Precipitation of Barium Sulphate Nanoparticles in Microemulsion: Experiments and Modelling

Fällung von Bariumsulfat Nanopartikeln in Mikroemulsionen: Experimente und Modellierung

Dissertation

zur Erlangung des akademischen Grades

Doktoringenieur
(Dr. - Ing)

von M.Sc. Dendy Adityawarman

geb. am 29 August 1975 in Semarang, Indonesien

genehmigt durch die Fakultät für Verfahrens- und Systemtechik
der Otto-von-Guericke-Universität Magdeburg

Gutachter: Prof. Dr.-Ing. habil. Kai Sundmacher
Prof. Dr.-Ing. habil. Jürgen Tomas

eingereicht am 04. 12. 2006

Promotionskolloquium am 10. 04. 2007

Danksagung

Mein besonderer Dank gilt meinem Betreuer Herrn Prof. Dr.-Ing Kai Sundmacher für die fachlichen Anregungen, die Diskussionsbereitschaft und seine jederzeit freundliche Unterstützung.

Ebenfalls bedanken möchte ich mich bei Herrn Prof. Dr.-Ing. Jürgen Tomas für die fachliche Unterstützung und die Bereitschaft zur Übernahme des Zweitgutachten.

Mein herzlicher Dank gilt allen Kollegen des Lehrstuhls Systemverfahrenstechnik für die Hilfsbereitschaft und die gute Stimmung, die einen wesentlichen Anteil am Gelingen dieser Arbeit hatte. Besonders möchte ich Dr. Andreas Voigt, Dr. Jürgen Koch, Björn Niemann, Michael Fricke, und Evelyn Felsch danken.

Besonders bedanken möchte ich mich auch bei meiner Frau Winda Azwani M.D. und meinen Eltern, die viel Geduld dafür aufgebracht haben, dass ich ihnen während der Erstellung dieser Arbeit wenig Zeit widmen konnte.

Schriftliche Erklärung

Ich erkläre hiermit, dass ich die vorliegende Arbeit ohne unzulässige Hilfe Dritter und ohne Benutzung anderer als der angegebenen Hilfsmittel angefertigt habe. Die aus fremden Quellen direkt oder indirekt übernommenen Gedanken sind als solche kenntlich gemacht.

Insbesondere habe ich nicht die Hilfe einer kommerziellen Promotionsberatung in Anspruch genommen. Dritte haben von mir weder unmittelbar noch mittelbar geldwerte Leistungen für Arbeiten erhalten, die im Zusammenhang mit dem Inhalt der vorgelegten Dissertation stehen.

Die Arbeit wurde bisher weder im Inland noch im Ausland in gleicher oder ähnlicher Form als Dissertation eingereicht und ist als Ganzes auch noch nicht veröffentlicht.

Magdeburg , Mai 2007

(M.Sc. Dendy Adityawarman)

Abstract

Today, the scenario of a well-controlled large-scale production of nanoparticles is a very important aspect in nanotechnology. The present work aims at the investigation of different engineering aspects on the production of nanoparticles using microemulsions, which lead to possible process control**.** Prior to the precipitation process, this study explains that the phase behaviour of the ternary as well as of the quaternary mixture (with reactants) has to be analysed to identify microemulsion regions being suitable for nanoparticle precipitation. Dynamic light scattering had been used for determining the droplet size and viscosity measurements had been undertaken to predict the internal structure of the fluid. Bulk phase precipitation of $BaSO_4$ was also conducted at different operating conditions in order to get basic understanding of the process itself. Generally a microemulsion made out of water, cyclohexane and surfactant is loaded with two reactants, $BaCl_2$ and K_2SO_4, to carry out $BaSO_4$ precipitation**.** A non-ionic technical surfactant, Marlipal O13/40 is employed, as this surfactant is cheap and available in big quantities and therefore preferred for a scale-up approach. The influence of suitable process control parameters like the feeding rate, the stirring rate, the feeding sequence, or the initial concentrations of the reactants on the particle size has been studied to gain a deeper understanding of the process formation of nanoparticles in a non-ionic water/oil microemulsion**.** The particle precipitation was carried out in a semi-batch reactor. Transmission electron microscopy was used to analyse the size, the size distribution, and shape of precipitated nanoparticles. A measurable influence on particle size was found for different initial concentration ratios of the two reactants. It was also found that with increasing particle size the shape changed from spherical to cubic. A corresponding simplified mathematical model based on mass balances qualitatively confirms the observed changes in particle size. Argumentations based on the droplet occupancy number, the critical nucleation number and the corresponding number of nucleated particles are given to explain the change in the mean particle size.

Keywords: Nanoparticles, $BaSO_4$, Microemulsions, Precipitation, Mathematical model

Kurzfassung

Die Gestaltung von technischen Prozessen zur kontrollierten Synthese von Nanopartikeln ist heutzutage ein sehr wichtiger Aspekt der Nanotechnologie. Diese Arbeit befasst sich dabei im Speziellen mit der ingenieurwissenschaftlichen Fragestellung, wie die Eigenschaften von Bariumsulfat-Nanopartikeln ($BaSO_4$) gezielt mit Hilfe der Mikroemulsionsfällung beeinflusst werden können. Aufgrund des komplexen Phasenverhaltens von Mikroemulsionen sind eingehende Voruntersuchungen zur Bestimmung des Mikroemulsionsbereiches notwendig, wobei sowohl die reine Mikroemulsion bestehend aus Wasser, Cyclohexan und dem nicht-ionischen technischen Tensid Marlipal O 13/40 als auch die Mikroemulsion zusammen mit den im Wasser gelösten Reaktanten ($BaCl_2$ und K_2SO_4) analysiert werden muss. Durch den Einsatz von dynamischer Lichtstreuung (DLS) zur Bestimmung der Tropfengröße und Viskositätsmessungen zur Analyse der inneren Fluidstruktur konnten eindeutige Existenzbereiche der Mikroemulsion für den gesamten benötigten Konzentrationsbereich der Reaktanten identifiziert werden.

Die eigentliche Fällungsreaktion ist in einem standardisierten Rührkesselreaktor in halbkontinuierlicher Betriebsweise durchgeführt worden. Die Mikroemulsionen im Reaktor und im Reaktorzulauf enthielten dabei jeweils einen gelösten Reaktanten, so dass erst durch den Tropfenaustausch im Reaktor die Fällungsreaktion eingeleitet wurde. Um zu einer gezielten Einstellung der Partikeleigenschaften zu gelangen, sind Einflussfaktoren wie die Zulaufgeschwindigkeit, die Rührergeschwindigkeit, die Zulaufsequenz und das Einsatzverhältnis der Reaktanten untersucht worden. Die resultierenden Partikelgrößenverteilungen und Partikelformen sind mittels Transelektronenmikroskopie (TEM) ausgewertet worden. Es zeigte sich, dass eine signifikante Steuerungsmöglichkeit für die Partikelgröße durch das Einsatzverhältnis der Reaktanten gegeben ist. Außerdem ließ sich feststellen, dass sich die Partikelform mit zunehmender Partikelgröße von sphärisch nach kubisch ändert. Weitere wichtige Aspekte dieser Arbeit waren vergleichende Fällungsexperimente in kontinuierlicher Phase sowie eine vereinfachte mathematische Modellierung und Simulation der Mikroemulsionsfällung.

Schlüsselwörter: Nanopartikel, $BaSO_4$, Mikroemulsion, Fällung, Modellierung

Table of Contents

Notation

Latin Symbols

Symbol	Explanation	Unit
A	surface area of nucleus	m^2
b	rate order of nucleation kinetics	(-)
bf	baffle diameter	cm
B_{nuc}	nucleation rate	(-)/(l s)
$B_{nuc,me}$	nucleation rate in microemulsion system	(-)/(l s)
B^0	homogeneous nucleation rate constant	(-)/(l s)
c	concentration of the sparingly soluble salt	mol/l
$c_{A^+}^{sat}$	concentration of A at saturation	mol/l
$c_{B^+}^{sat}$	concentration of B at saturation	mol/l
$c_{Ba^{2+}}^{sat}$	concentration of barium ions at saturation	mol/l
$c_{SO_4^{2-}}^{sat}$	concentration of sulphate ions at saturation	mol/l
c_A	concentration of A	mol/l
c_B	concentration of B	mol/l
$c_{Ba^{2+}}$	concentration of barium ions	mol/l
$c_{SO_4^{2-}}$	concentration of sulphate ions	mol/l
c_C	concentration of liquid molecules C	mol/l
$c_{C,crit}^{sat}$	critical supersaturation concentration of liquid molecules C	mol/l
c_m	treshold of metastable concentration limit	mol/l
c^{sat}	concentration at saturation	mol/l

Symbol	Explanation	Unit
c_{BaCl_2}	concentration of $BaCl_2$	mol/l
$c_{K_2SO_4}$	concentration of K_2SO_4	mol/l
$c_{BaCl_{2,0}}$	initial concentration of $BaCl_2$	mol/l
$c_{K_2SO_{4,0}}$	initial concentration of K_2SO_4	mol/l
c_{BaSO_4}	concentration of BaSO4	mol/l
$C_{i,0}$	initial concentration	mol/l
$c_{BaSO_4}^{sat}$	concentration of BaSO4 at saturation	mol/l
Δc	concentration gradient	mol/l
Δc_{me}	concentration gradient in microemulsion system	mol/l
CP	photon correlation function	(-)
d_{drop}	diameter of droplet	nm
d	diameter of stirrer	cm
d_p	particle diameter	nm
d_{pm}	mean particle diameter	nm
d_{pm_exp}	mean particle diameter from experiments	nm
d_{pm_sim}	mean particle diameter from simulation	nm
D_{ab}	diffusion coefficient	m^2/s
D	diameter of reactor	cm
f	number density function	(-)/nm
g	rate order of growth kinetics	(-)
G	growth rate	nm/s
G_{me}	growth rate in microemulsion system	nm/s
ΔG	Gibbs free energy	J

Symbol	Explanation	Unit
ΔG_v	volume excess free energy	J
$\Delta G_{v,vol}$	volume excess free energy per unit volume	J/m^3
ΔG_s	surface excess free energy	J
ΔG_{crit}	critical free-energy change to form nuclei	J
h	stirrer height level from the bottom	cm
H	liquid height level from the bottom	cm
i	number of molecules inside a water droplet	(-)
k_{chem}	chemical reaction rate constant	l/(mol s)
k_{ex}	droplet exchange rate constant	l/(mol s)
k_a	area shape factor	(-)
k_v	volume shape factor	(-)
k_{vp}	particle shape factor	(-)
k_{vd}	droplet shape factor	(-)
k_n	nucleation rate constant	$(-)/((l\ s)(mol/l)^b)$
$k_{n,me}$	nucleation rate constant in microemulsion	$(-)/((l\ s)(l/mol)^{N_{crit}})$
k_g	growth rate constant	$(nm/s)(l/mol)^g$
$k_{g,me}$	growth rate constant in microemulsion	$(nm/s)(l/mol)^2$
k	Boltzmann constant, = $1.38x10^{-23}$	J/K
K_v	scattering vector	(-)/m
K	film mass transfer coefficient	m/s
K_{sp}	solubility product	$mol^2\ l^2$
L	characteristic length of the crystal	m
m_{water}	mass of water	kg

Symbol	Explanation	Unit
$m_{surfactant}$	mass of surfactant	kg
m_{oil}	mass of oil	kg
Mw_{BaSO_4}	molar mass of $BaSO_4$ molecule, = 233.39	mol/g
M	mass solid deposited	g
M_C	molar mass of C	g/mol
n_A^F	feed rate of A	mol/s
n	refractive index	(-)
n_A	number of moles of A	mol
n_B	number of moles of B	mol
n_C	number of moles of C	mol
n_C^{solid}	number of moles of solid C	mol
n_C^{total}	total number of moles of C formed by chemical reaction	mol
n_{drop}	Number of moles of droplets	mol
n.a	not available	(-)
n_P	moles of particles	mol
N_A	Avogadro number, = 6.0221367×10^{23}	(-)/mol
N_{crit}	critical number of molecules for nucleation	(-)
N_{BaSO_4}	number of barium sulphate molecules	(-)
N_C^P	number of molecules in one particle	(-)
N_P	total number of particles	(-)
N_{Re}	Reynolds number	(-)
p_i	probability of droplets containing i molecules C	(-)
P_W	mean specific power input	W/l

Symbol	Explanation	Unit
P	C converted into particle	(-)
P’	growing particle	(-)
Q_f	feeding rate	ml/min
Q_w	water phase feeding rate	ml/min
r_{crit}	critical nucleus size	m
r	spherical radius of nucleus	m
r_{chem}	rate of chemical reaction	mol/(l s)
r_g	rate of C consumption due to growth	mol/s
$r_{nuc\text{-}cons}$	rate of C consumption due to nucleation	mol/s
R_c^0	initial concentration ratio	(-)
R_N^0	initial molar ratio	(-)
R	universal gas constant , = 8.314	J/(mol K)
R_v	volumetric ratio	(-)
S	supersaturation ratio	(-)
S_i	initial supersaturation ratio	(-)
t_{me}	time for microemulsion viscosity measurement between two points in capillary	s
t_{cy}	time for cyclohexane viscosity measurement between two points in capillary	s
T	absolute temperature	K
T_u	temperature of upper boundary	^oC
T_l	temperature of lower boundary	^oC
V_r	volume of reactant inside reactor	ml
V_f	volume of reactant to be fed	ml

Symbol	Explanation	Unit
V_w	volume of water phase	ml
V_{wt}	total volume of water in microemulsion (in the feed and in the reactor)	ml
V_{wr}	volume of water phase containing critical number of nuclei or more	ml
V_C	volume of one particle C	nm^3
x	film thickness	m

Greek Symbols

Symbol	Explanation	Unit
α	weight fraction of oil in the mixture of oil and water	kg/kg
β_o	geometrical factor equal to $16\pi/3$ for spherical nuclei	(-)
Γ	decay or inverse coherence time	1/s
γ	weight fraction of surfactant in the ternary mixture	(-)
γ_0	minimum weight fraction of surfactant in the ternary mixture to form a three phase microemulsion	kg/kg
$\bar{\gamma}$	surfactant efficiency to homogenize the same amount of water and oil	(-)
η_r	relative viscosity	(-)
η	liquid viscosity	kg/(m s)
λ	average droplet occupancy of liquid molecules C	(-)
μ_2	chemical potential of a component in phase 2	J
μ_1	chemical potential of a component in phase 1	J
ν	molecular volume	m^3

Symbol	Explanation	Unit
ρ_{BaSO_4}	density of bulk crystalline barium sulphate ,= 4.5	g/cm^3
ρ_{me}	density of microemulsion	g/cm^3
ρ_{cy}	density of cyclohexane	g/cm^3
ρ	mass density	kg/m^3
ρ_C	density of C	g/nm^3
σ	surface free energy per unit of area	J/m^2
τ_{chem}	chemical reaction time constant	s
τ_{ex}	droplet exchange time constant	s
τ_{nuc}	nucleation time constant	s
τ_g	particle growth time constant	s
υ	kinematic viscosity	m^2/s
ω	stirring rate	min^{-1}
$\omega\theta$	dimensionless mixing time	(-)
φ	number of phases in microemulsions	(-)

Chapter 1

Introduction

1.1 Overview

During the last decades, interests in the study of nano-scale materials (nanoparticles) have been increasing at an accelerating rate, stimulated by innovative solutions for tomorrow's products. Advances in characterization techniques and material synthesis of nano-scale materials reveal that these materials exhibit many unique and interesting physical and chemical properties with a number of potential technological applications such as catalysts, pharmaceuticals, semiconductors, and fine chemicals. On the laboratory scale, various nano-scale materials have been produced but not on a large scale [Arriagada and Osseo-Assare, 1999]. Another recent issue in the synthesis of nano-scale materials is subjected in a defined size distribution and morphology [Chen et al., 2005]. Many different approaches, like wet chemical processes e.g. for precipitation and crystallization (in bulk and dispersed systems) and gas-phase synthesis e.g for chemical-physical vapour deposition, show several disadvantages as there are spatial inhomogeneities of concentration in reaction and dispersion processes taking place in these methods. For these reasons, methods and process as for a controlled production of particles with a specific size and morphology are becoming important topics for many areas of technical application.

Certain ternary dispersed systems, called microemulsions, have demonstrated their ability as a promising alternative medium for the synthesis of defined nanoparticles for almost 20 years [Nagy, 1999]. Under appropriate conditions, a water-in-oil (w/o) system will self-assemble into nanodroplets (5-100 nm) if the surfactant molecules surround a fluid core. These water nanodroplets can be filled with different reactants for precipitation and crystallization for nanoparticle synthesis. There are different kinds of nanoparticles, for different applications, which can be produced inside such a microemulsion system which is usually prepared by two important methods. The first is the one-microemulsion method (diffusion based process) and the second is the two-microemulsion method (droplet fusion-fission based process).

In this present work, the synthesis of barium sulphate ($BaSO_4$) nanoparticles is chosen as a model reaction system for the investigations. The main reason of this selection is based on the availability of important information such as kinetic data (nucleation and growth rate) for the bulk precipitation of $BaSO_4$, which are useful for further model based process analysis.

$BaSO_4$ nanoparticles will be produced by the two-microemulsion method by mixing of two identical water-in-oil (w/o) microemulsions, the first containing the reactant barium chloride ($BaCl_2$) (A) and as second reactant (B) inside the reactor, containing aqueous reactant potassium sulphate (K_2SO_4). After the mixing of these two reactants, droplet fusion and fission will lead to an instantaneous chemical reaction between both reactants, and as an immediate consequence $BaSO_4$ liquid molecules (C) will be produced. As soon as the liquid molecules C have reached a critical number N_{crit}, nuclei are formed which grow to larger particles inside the nanodroplets.

The schematic process of nanoparticle synthesis in microemulsion systems used in this study is shown in Fig. 1.1.

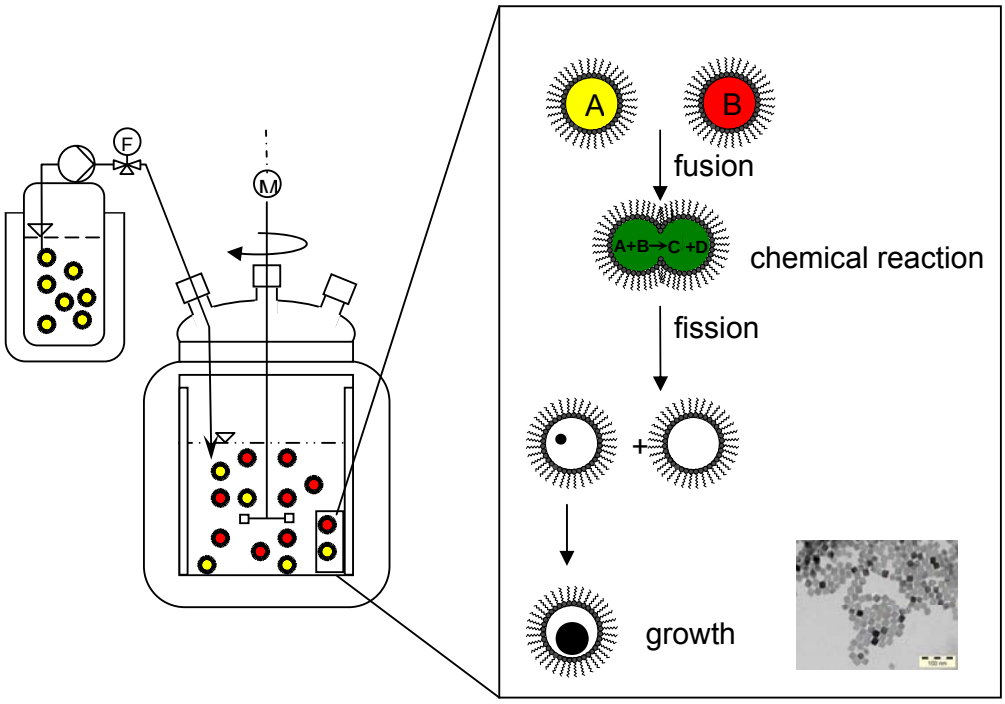

Fig. 1.1: Scheme of nanoparticle synthesis based on the two-microemulsion method.

1.2 Research objectives of this thesis

In order to use microemulsion systems as reaction media for the large-scale controllable production of nanoparticles, one should investigate several important process parameters to find out suitable tools for controlling the particle properties. The objective of this work is therefore to identify possible operating parameter to control the particle size and distribution. A further objective is to develop a mathematical to analyse the dynamic process behaviour based on the precipitation theory which typically used for bulk processes. With this model specific kinetic data for microemulsion precipitation could be derivable.

In chapter 2, the fundamental aspects of this work will be addressed. Basic information about nano-scale materials, precipitation processes, microemulsions, and the synthesis of nanoparticles inside microemulsion droplets will be discussed.

Chapter 3 provides information about the materials, the experimental set-up, and the measuring techniques which are used in this work.

Chapter 4 conveys the experimental results as the major part of this work. Prior to the microemulsions precipitation study, detailed investigations on the phase behaviour of the ternary microemulsion mixtures and $BaSO_4$ precipitation in the bulk phase are performed. The investigation on the ternary mixture water/oil/surfactant behaviour yields important information on operating regions of microemulsions precipitation and the droplet size. Microemulsions systems that were used here a ternary mixture of non-ionic Marlipal surfactant-cyclohexane-water. $BaSO_4$ precipitation in the bulk phase were carried out to investigate important operating parameters, such as the stirring rate, the feeding rate, and the initial molar reactant ratio. Also the precipitation of $BaSO_4$ nanoparticles inside the microemulsion system will be reported in this chapter. Possible control parameters for the mean particle diameter in microemulsion precipitation were also identified in executed experiments.

In chapter 5, a mathematical model for microemulsion precipitation is developed to analyse the complex interactions of population mechanisms like fusion and fission of droplets, chemical reaction, and nucleation and growth of particles within the droplets. The developed model comprises of the estimated microemulsion specific nucleation kinetics, which take the discrete character of the system on molecular scale into account, and also involves the estimated growth kinetics, which have been adopted from the bulk phase approach.

The major outcome of this process model is the fast (below one second calculation time) and reliable determination of the evolution of the mean particle diameter as a function of time. The model is therefore an efficient tool which can be coupled to Computational Fluid Dynamics (CFD) as well as to process control schemes and which is also suited for scale-up studies. The comparison with experimentally obtained data from barium sulphate precipitation shows a qualitatively good agreement. Sensitivity studies have also been carried out to investigate the reliability of the estimated parameters (critical number for nucleation N_{crit}, nucleation rate constant $k_{n,me}$, growth rate constant $k_{g,me}$) as well as the influence of the droplet diameter d_{drop} on the resulting mean particle diameter.

At the end of this work, concluding remarks are given in chapter 6.

Chapter 2

Fundamental Aspects

2.1 Nano-scale materials

2.1.1 Nano-scale material properties and potential applications

Nanotechnology is one of the most important future key technologies for science and industry. In the field of material science and engineering, nanotechnology products can be synthesized from unit materials such as atoms and molecules to build ceramics, catalysts, and semiconductors. Therefore nanotechnology is one of the most attractive research areas. Nano-scale materials are commonly characterized by at least one dimension in the nanometer range (1 nm = 10^{-9} m) [Rao et al., 2004]. Fig. 2.1 below gives an impression of the position of nano-scale dimensions among different objects that are already known. By simple calculations, it can be estimated that the volume of one Bacillus cereus bacterium which is in the micrometer range could hold one million of 5 nm nanoparticles [Klabunde, 2001].

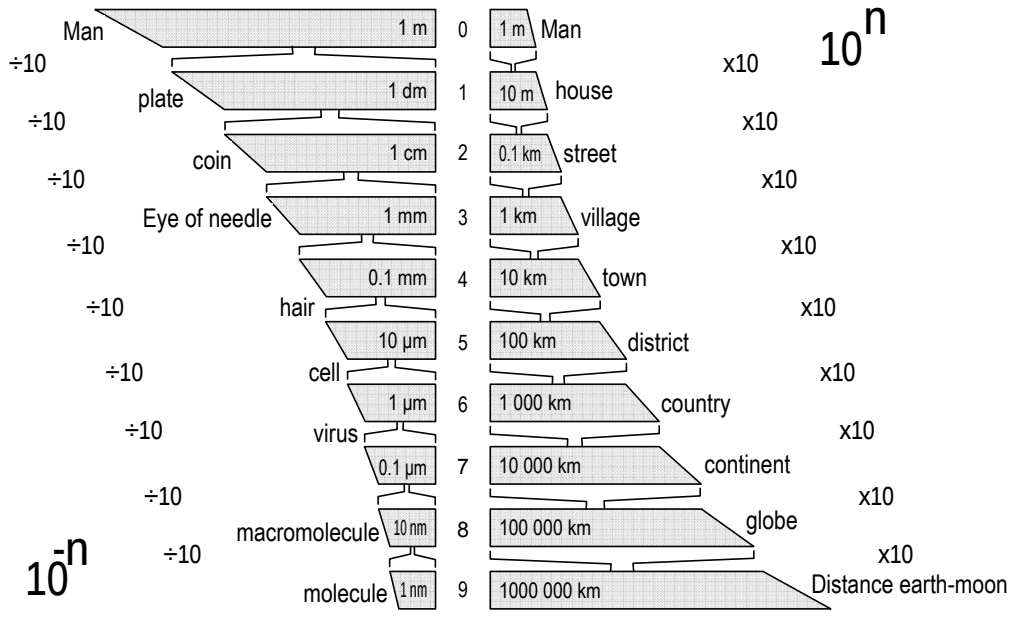

Fig. 2.1: Integration of natural and technical nanosystems in a functional microstructured environment [redrawn from Köhler and Fritzsche, 2004].

In the nano-scale range, the materials structures and properties differ significantly from those of single atoms or molecules but also from bulk materials. These unique properties bring nano-scale materials into an emerging wide area of applications.

One of the interesting properties of nano-scale materials is the decreasing melting temperatures with decreasing size as an effect of the increasing number of surface atoms. Since the number of surface atoms increases with smaller particles, these atoms can be more easily rearranged than those in the centre of the particles, and thus the melting process can start earlier [Klabunde, 2001]. As can be seen in Fig. 2.2 below, there is a dramatic decrease of the melting points for particles smaller than 3-4 nm [Castro et al., 1990].

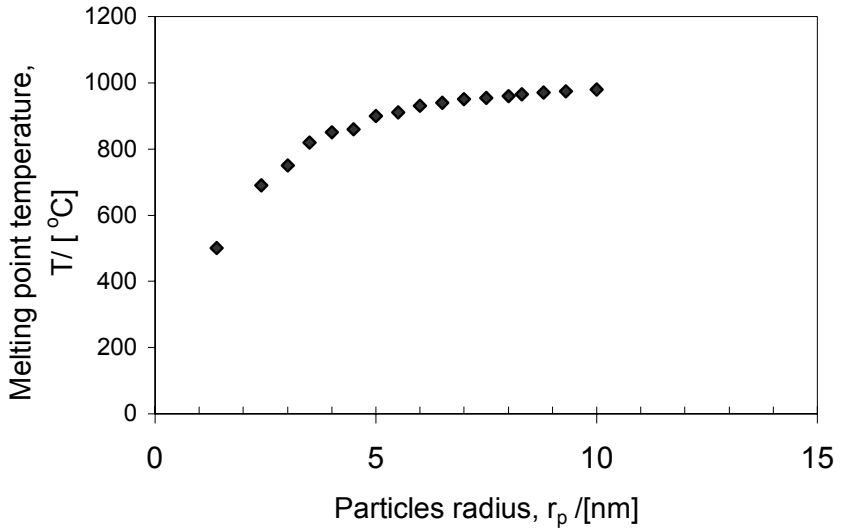

Fig. 2.2: Relation between the size of gold particles and their melting points [redrawn from Castro et al., 1990].

The effect of the increasing number of surface atoms with decreasing particle size also makes small metal nanoparticles becoming a highly reactive catalyst as the area of surface active centres for catalytic processes will also increase [Klabunde, 2001].

Another interesting point of nanoparticles is their magnetic property. Whilst magnetic bulk materials are usually formed from multiple magnetic domains, small magnetic nanoparticles often consist only of one domain and exhibit a phenomenon known as superparamagnetism. In this case the overall magnetic coercivity is lowered as a result of random processes of the particle magnetization due to thermal fluctuations [Kelsall et al., 2005]. Concerning optical properties, the effect of the reduced dimensionality on the electron structure has a strong impact on the valence band and the conduction band [Kelsall et al.,

2005]. Optical emission and absorption depend on the transition between these bands. For this reason, semiconductors and metals, in particular, show large changes in their optical properties, such as the colour being a function of the particle size. For example, colloidal solutions of gold nanoparticles have a deep red colour which becomes progressively more yellow with increasing particle size.

The classification of nano-scale materials depends generally on the number of dimensions which exist in the nanometer range. By reason of this dependence on the dimensions, nano-scale materials can be classified as: zero-dimensional (e.g. nanopores), one-dimensional (e.g. laminate structure), two-dimensional (nanowires/nanotubes), and three-dimensional structure (e.g. super lattices). This classification system is useful in describing the type of the structure of the nano-scale materials one would like to produce. In Table 2.1, a list of the typical size and dimensions of nano-scale materials is shown.

Table 2.1 Typical size of some nano-scale materials [Rao et al., 2004].

Form	**Size**	**Material**
Nanocrystals	Diameter of 1…10 nm	Metals, semiconductors, magnetic materials.
Nanowires	Diameter of 1…10 nm	Metals, semiconductor, oxides sulfides, nitrides.
Nanotubes	Diameter of 1…10 nm	Carbon, layered metal.
Nanoporous solids	Pore diameter of 0.5…10 μm	Zeolites, phosphates, etc.
2-dimensional array	Several nm^2…μm^2	Metals, semiconductors, magnetic materials.
Surface and thin film	Thickness 1…1000 nm	Variety of materials.
3-dimensional structures (super lattices)	Several nm^3…μm^3	Metals, semiconductors, magnetic materials.

Some important applications and technology fields based on nano-scale materials are listed in the following Table 2.2.

Table 2.2 Several fields of application for nano-scale materials.

Field	**Applications**
Pharmacy/Health	• Smart and controlled released drugs [Herrero-Vanrell et al., 2005] • Cancer therapy [Zhou et al., 2005] • DNA tagging for biochemical assays [Charles Cao et al., 2005]
Enviromental/Green Chemistry	• Solar cells [Kruis et al., 1996] • Water purification [Peng et al., 2005] • Nano-adsorbents [Abu-Daabes and Pinto, 2005]
Electronics	• Nanostructured electrodes [Zheng et al., 2005] • Nano-sensors [Zhao et al., 2005] • Batteries [Son, 2004]

2.1.2 Synthesis of nano-scale materials

Nano-scale materials can be made in numerous ways. A broad classification divides the synthesis methods into either that which build materials from bottom up, i.e. atom by atom, or those constructed from the top down using processes that involve the restructuring or reformation of atoms to produce the desired structure [Kelsall et al., 2005]. The two approaches are schematically represented in Fig. 2.3.

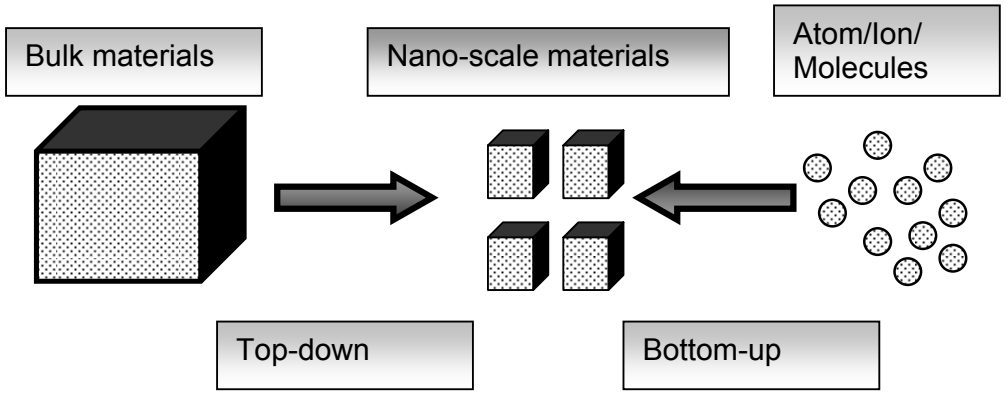

Fig. 2.3: Schematic of nano-scale materials synthesis.

Top-down routes are included in the typical solid-state processing of the materials. These routes are based on the reduction of bulk (micro) sized materials into the nano-scale. High energy ball milling or microfluidizers are used to break down dispersed solids down to 100 nm. Coarse-grained materials (metals, ceramic, and polymers) in the form of powders are crushed mechanically in ball milling by hard materials such as steel or tungsten carbide. This repeated deformation due to applied forces can cause large reduction in grain size since energy is being continuously pumped into crystalline structures to create lattice defects. Usually this route is not suitable for preparing uniformly shaped materials, and it is very difficult to realize very small particles even with high energy consumption. Bottom-up routes are more often used for preparing most of the nano-scale materials with the ability to generate a uniform size, shape, and distribution. Bottom-up routes effectively cover chemical synthesis and the precisely controlled deposition and growth of materials. Within that bottom-up route, physical/aerosol and wet/chemical synthesis are widely used for particle generation and listed in the following Table 2.3.

Table 2.3 Various synthesis methods for nano-scale materials

Methods	**Type of process**
Physical/aerosol methods	• Vapour condensation [Lee et al., 2005] • Spray pyrolysis [Yu et al., 2005] • Thermochemical/flame decomposition of metal organic precursor [Skandan et al., 1999]
Chemical/wet methods	• Sol-gel technique [Hintz et al., 2003] • Low-temperature wet chemical synthesis; precipitation/crystallization from bulk solution [Chen and Chang, 2005] • Microemulsion methods [Adityawarman et al., 2005]

Physical vapour synthesis is most often used for the preparation of carbon black, colour pigments and fumed silica, using thermal plasma and lasers as heat sources [Wagner and Pratsinis, 2005]. This method involves the conversion of solid materials into gaseous components by physical processes. The gaseous material is then cooled and re-deposited on a substrate with possible modifications, such as reaction with another gas.

Chemical/wet syntheses include classical crystallization, bulk or emulsion precipitation. Sol-gel methods are widely used for fine chemical preparation [Yang et al., 2005]. These routes involve the reaction of chemical reactants with other reactants in either an aqueous or non-aqueous solution. These chemical reactants react and self-assemble to produce a supersaturated solution with the product. This supersaturated solution at certain conditions results in particle nucleation. These initial nuclei then grow into nanometer size particles.

Barium sulphate ($BaSO_4$) particles can lead to a significant improvement of optical characteristics and flow behaviour, and have been used widely in pigments, printing inks, and medicine [Chen et al., 2005]. $BaSO_4$ has an orthorhombic crystal structure, the unit cell are a = 8.88 Å, b = 5.46 Å, and c = 7.16 Å. Fig. 2.4 below shows the $BaSO_4$ morphology as predicted using Cerius2® software [Van-Leuween, 1998].

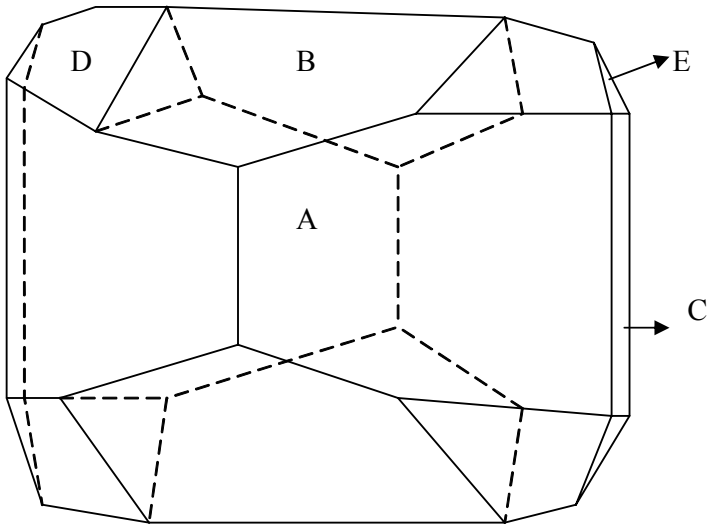

Fig. 2.4: The predicted morphology of orthorhombic crystal structure of barium sulphate from the unit cell dimensions a = 8.88 Å, b = 5.46 Å, and c = 7.16 Å. The indicated faces are A = {101}, B = {011}, C = {200}, D = {111}, and E = {210} [redrawn from Van-Leeuwen, 1998].

Microemulsions techniques for $BaSO_4$ nanoparticle synthesis are becoming a new focus in this study of nano-scale materials. The use of microemulsions systems is introduced to precipitate $BaSO_4$ nanoparticles, which shows the ability for efficient control of particle properties. As a comparison to this study, there have been several reports of barium sulphate nanoparticles and nanofilament synthesis using microemulsion technology [Qi et al., 1996,

Hopwood and Mann, 1997, Li and Mann, 2000, Ivanova et al., 2001, and Summers et al., 2002].

2.2 Precipitation in bulk phase

Solid particles can be generated from precipitation and crystallization processes based on the wet/chemical route. For that reason, in this chapter, the theoretical basics of precipitation processes is discussed.

The phase transformation of dissolved liquid molecules into a solid phase proceeds by a crystallization process and is relatively slow as the necessary supersaturation is created by a reduction of temperature or by evaporation of solvent. On the other hand in case of classical precipitation, two chemical reactants are mixed. Then, a fast chemical reaction initiates the formation of a supersaturated solution which leads to the formation of solid particles as the result of the low solubility of the formed product.

Precipitation is one of the oldest unit operations widely used in the chemical industry to produce defined solid particles. The Solvay process, which precipitates sodium bicarbonate, is an interesting old example for precipitation, which is still widely used in large-scale production. In Table 2.4, several applications of precipitation processes and its important aspects are listed.

Table 2.4 Important industrial precipitation processes [Van Leeuwen, 1998]

Application	**Important aspect**	**Examples**
• production of pigments	• smaller particle	• $CaZn_2(PO_4)$ [Ding and Wang, 2006]
• production of pharmaceuticals	• smaller particle, purity	• salbutamol sulphate [Chiou et al., 2006]
• waste water treatment	• smaller particle	• $Na_2Al_2O_4$ [Kemmer, 1998]

2.2.1 Mechanisms of precipitation processes

Precipitation is a process in which a solid product is formed as a result of a chemical reaction of two or more components contained in the mother phase [Nyvlt et al., 1985]. The process of phase transformation requires a perturbation of the equilibrium as a driving force,

which can be explained by thermodynamic principles. When a substance is transformed from one phase into another, the change in the molar Gibbs free energy ΔG during the transformation, at constant pressure and temperature, is given by [Dirksen and Ring, 1991]:

$$\Delta G = (\mu_2 - \mu_1), \tag{2.1}$$

where ΔG is the molar Gibbs free energy, μ_2 is the chemical potential of a component in phase 2 and μ_1 is the chemical potential of a component in phase 1. When $\Delta\mu<0$, the transition from phase 1 to 2 is spontaneous. Alternatively, when $\Delta\mu>0$, this phase transformation is thermodynamically not possible (on a macroscopic scale), whereas, $\Delta\mu = 0$ defines the condition for thermodynamic equilibrium. The molar Gibbs free energy can be expressed in terms of the supersaturation ratio S as follows (assumed activity coefficient = 1):

$$\Delta G = -R \cdot T \cdot \ln(S), \tag{2.2}$$

where R is the universal gas constant and T is the absolute temperature. For ionic precipitation systems, the solubility can be explained in terms of the solubility product K_{sp} as given in the following equations:

$$A^+ + B^- \leftrightarrow AB \tag{2.3}$$

$$K_{sp} = c_{A^+}^{sat} \cdot c_{B^+}^{sat}, \tag{2.4}$$

where $c_{A^+}^{sat}$ is the concentration of A^+ at saturation, and $c_{B^+}^{sat}$ is the concentration of B^- at saturation.

The supersaturation ratio S for this system is defined as:

$$S = \frac{c_{A^+} \cdot c_{B^-}}{K_{sp}} \tag{2.5}$$

where c_A is the concentration of A^+ and c_B is the concentration of B^-.

From eq. 2.2, one can expect that S as a dimensionless concentration ratio could be identified as the key variable in any precipitation process. Compared to the crystallization process, the solubility of the products emerging from precipitation processes is very low. The supersaturation ratio S of a precipitation process is typically between 10^2-10^4 while S for the crystallization process (as the formation of the solid proceeds in the region close to the solubility limit) is relatively low (S ~ 1-2) [Schmidt, 2000].

In general, a precipitation process is described by basic primary and secondary processes. The basic primary processes include the creation of a certain supersaturation level followed by the generation of nuclei (nucleation) and the subsequent growth, which is always present during a precipitation process. Then, a number of secondary processes like aging,

ripening, agglomeration, and breakage might occur depending on the nature of the process itself and the chemical compound as illustrated in the following scheme (Fig. 2.5).

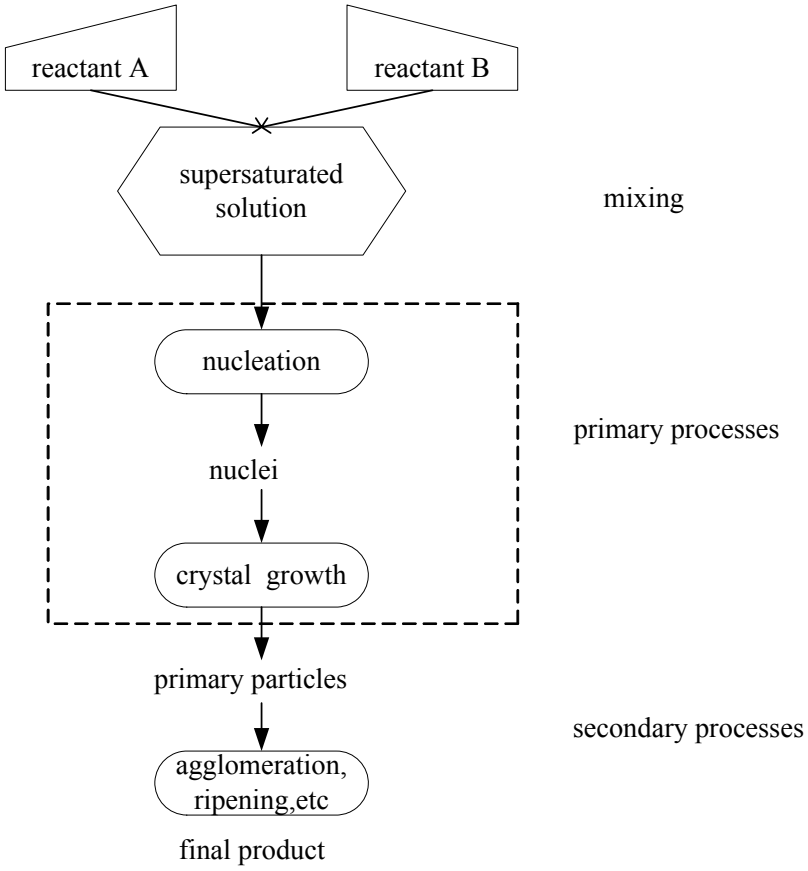

Fig. 2.5: Scheme of precipitation process.

In this work, since we want to focus on microemulsion precipitation, the surfactant layer at the nanodroplets builds a protective layer to suppress the secondary processes. For this reason, only the primary processes will be studied in detail in this work.

2.2.2 Nucleation

In a highly supersaturated solution the instability of the system will result in a fast local concentration fluctuation. This leads in a homogeneous phase to small solid clusters of molecules. These clusters are assumed to be formed by the mechanism of addition of dissolved molecules to the cluster until a critical cluster size is reached. Thereby, a stable nucleus is formed [Myerson, 1993]. If the cluster can not reach the critical size, it will re-dissolve. In the absence of foreign particles this mechanism is considered as primary

homogeneous nucleation. For primary heterogeneous nucleation, nuclei are formed on the surface of foreign solid particles. These foreign particles are generally known to reduce the surface energy being required for nucleation as there are interactions between the foreign particles, molecules, and the solvent [Van-Leuween, 1998]. The surface energy σ can drop from around 0.08 - 0.1 J/m^2 (for homogeneous nucleation) to much lower values of about 0.002 - 0.003 J/m^2 (for heterogeneous nucleation). Fig. 2.6 illustrate that homogeneous nucleation occurs at very high supersaturation and heterogeneous nucleation occurs at much lower supersaturation.

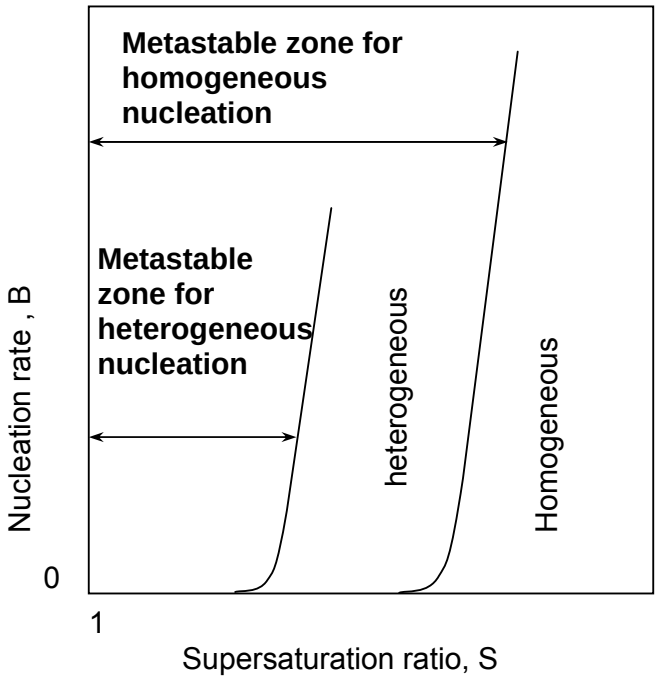

Fig. 2.6: Scheme of the dependencies of the primary nucleation rate B on the supersaturation ratio S [redrawn from Tavare, 1995].

Secondary nucleation is induced by breakage or attrition events of crystals. Since these events are secondary processes which do not occur in the here considered system, we will only discuss primary nucleation in the following.

Primary Nucleation

In the process of homogenous nucleation, ΔG as molar Gibbs energy is the sum of the surface excess free energy ΔG_s and the volume excess free energy ΔG_v [Tavare, 1995] and is described in the following manner:

$$\Delta G = \Delta G_s + \Delta G_v. \tag{2.6}$$

In other words ΔG is the overall excess free energy, ΔG_s is the free energy change required to form the surface of the nucleus and ΔG_v is the free energy change that results from the situation that a solute changes from the liquid to the solid state.

ΔG_s depends on the surface area and is therefore proportional to the square of the nucleus radius whereas G_v depends on the nucleus volume and is proportional to the cube of the nucleus radius [Randolph and Larson, 1988]. Assuming a spherical nucleus eq. 2.6 can be written as:

$$\Delta G = 4\cdot\pi\cdot r^2\cdot\sigma + (4\pi/3)\cdot r^3\cdot\Delta G_{v,vol} \tag{2.7}$$

where σ denotes the surface energy between the nuclei and its surrounding supersaturated fluid, $\Delta G_{v,vol}$ is volume excess free energy per unit volume and r the radius of a spherical nucleus.

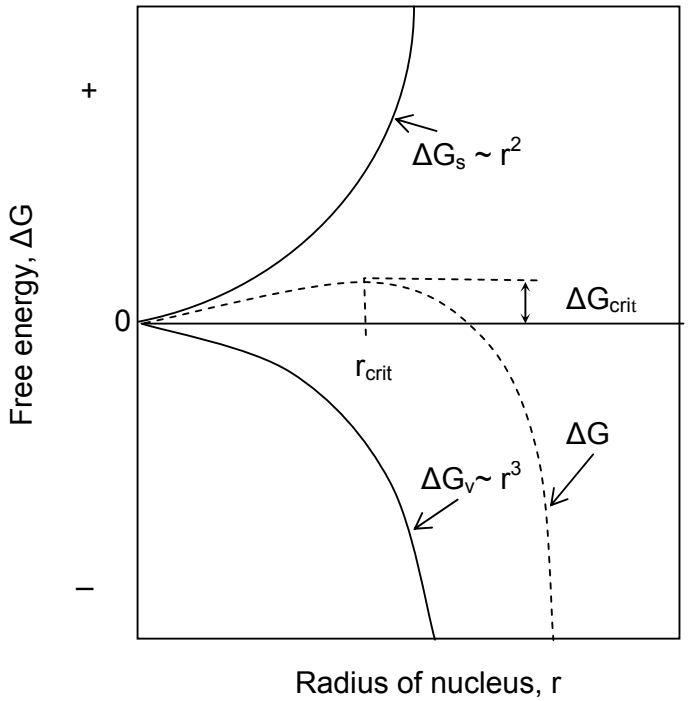

Fig. 2.7: Schematic free energy diagram for homogeneous nucleation [redrawn from Mullin, 2004].

The relation between the overall excess free energy and the spherical nucleus radius is shown in Fig. 2.7. It shows that any nucleus with a radius smaller than the critical radius r_{crit} is unstable and tends to be re-dissolved, because the growth of such a nucleus would increase the overall free energy of the system. If however the radius of a nucleus is greater or equal than r_{crit}, this nucleus will be stable and its growth will lead to a lowering of the system energy.

The relationship between the particle size and the solubility is expressed by the Gibbs-Thomson equation:

$$\ln\left(\frac{c}{c^{sat}}\right) = \frac{2 \cdot \sigma \cdot v}{k \cdot T \cdot r_{crit}}, \tag{2.8}$$

where r_{crit} is the critical nucleus radius, *v* is the molecular volume, and k is the Boltzmann constant. According to the equation above, the critical size of a nucleus is decreasing with increasing saturation.

Due to the energy barrier for the formation of nuclei, an Arrhenius type kinetic equation for the rate of nucleation can be employed [Tavare, 1995]. The nucleation rate B, defined as the number of nuclei produced per unit volume and per unit time, can be expressed as:

$$B_{nuc} = B^0 \cdot \exp(-\Delta G_{crit}/k \cdot T). \tag{2.9}$$

Here the energy required to form critical nuclei is given by:

$$\Delta G_{crit} = \beta_o \cdot \sigma^3 \cdot v^2/(k \cdot T \cdot \ln S)^2, \tag{2.10}$$

where ΔG_{crit} is the critical free-energy change to form nuclei, B^0 is a rate constant whose value is usually 10^{23}-10^{33}nuclei/(l s), β_o is a geometrical factor ($\beta_o = 16\pi/3$ for spherical nuclei), and *v* is the molecular volume [Randolph and Larson, 1988].

Equation 2.10 indicates that at least three variables govern the rate of nucleation: the temperature T, the degree of supersaturation S and the surface energy σ. The insertion of eq. 2.10 into eq. 2.9 shows that the rate of nucleation can be rewritten in the following way:

$$B_{nuc} = B^0 \cdot \exp\left[-\frac{16 \cdot \pi \cdot \sigma^3 \cdot v^2}{3k^3 \cdot T^3 \cdot (\ln S)^2}\right], \tag{2.11}$$

Eq. 2.11 is valid for spherical nuclei and homogeneous nucleation.

Equation 2.11 shows that if the supersaturation ratio is increased and the surface energy is decreased the result is a higher nucleation rate, which finally leads to the formation of particles of smaller size.

The strong non-linear behaviour of the exponential relation of the nucleation rate sometimes causes problems in computation; due to this reason eq. 2.11 can be approximated by a power law function of supersaturation at a given temperature [Tavare, 1995]:

$$B_{nuc} = k_n \cdot (c - c_m)^b \quad , \tag{2.12}$$

where k_n is a nucleation rate constant, c_m is the threshold concentration defined by Miers metastable limit ($c_m > c^{sat}$), c is concentration of the solute in liquid phase, and b is the nucleation kinetic rate order which is typically in the range of ~ 5 - 15 [Lindberg and Rasmusson, 2000].

Since $c_m \approx c^{sat}$ for most inorganic systems, the nucleation rate can be expressed by:

$$B_{nuc} = k_n \cdot (c - c^{sat})^b \tag{2.13}$$

From equation 2.13, it can be seen that the driving force of the nucleation in our case is the concentration difference.

Since $BaSO_4$ is chosen as model reaction system in microemulsion precipitation, the nucleation rate constant for this specific compound will be investigated here. In literature, a large number of studies have been reported on $BaSO_4$ precipitation. Though there exist a large amount of data, there can be still a lot of differences found in the kinetic rate constant parameter values reported in the literature. This indicates that these constants depend very much on the experimental conditions. Therefore, the approach taken in this research area is to use the kinetic studies from the literature (Baldyga et al., 1995) as a basic reference and then to estimate the specific value for the nucleation rate constant $k_{n,me}$ in microemulsion and the nucleation kinetic rate order b by fitting the simulated data to the experimental data being obtained on $BaSO_4$ microemulsion precipitation in this work (see chapter 5).

2.2.3 Growth rate of particles

Once a stable nucleus has been created in a supersaturated solution, within certain conditions this nucleus will grow and lead to a bigger particle. The growth of particles in crystallization and precipitation processes can be described by several mechanisms. Two basic processes occur during growth. These are: (1) mass transport by diffusion or convection from the bulk solution to the crystal/particle face and (2) surface reaction. The overall rate is determined by the relative magnitude of these two resistances in series.

In case that growth is dominated by mass transport which is typical for precipitation processes, the growth rate can be represented by a simple mass transfer equation as follows:

$$\frac{dM}{dt} = \frac{D_{ab}}{x} \cdot A \cdot (c - c^{sat}) \tag{2.14}$$

where M is solid mass being deposited, D_{ab} is the diffusion coefficient, x is the film thickness and A is the total surface area of the nuclei [Randolph and Larson, 1988]. In most cases of mass transfer, the film thickness x is not known, but the film mass transfer coefficient $k_m = D_{ab}/x$:

$$\frac{dM}{dt} = k_m \cdot A \cdot (c - c^{sat}) . \tag{2.15}$$

Since particles are usually described of the basis of their diameter rather than of their mass, it is more useful to express equation 2.15 with the help of the growth rate of the length dimension [Randolph and Larson, 1988]. If L is a characteristic diameter and k_v is a volume shape factor, then $M = \rho k_v L^3$, and the particle surface area is equal to $k_a L^2$ where k_a is an area shape factor. Using these relations equation 2.15 can be represented as:

$$k_v \cdot \rho \frac{d(L)^3}{dt} = k_m \cdot k_a \cdot L^2 \cdot (c - c^{sat}) \tag{2.16}$$

$$3k_v \cdot \rho \cdot L^2 \cdot \frac{dL}{dt} = k_m \cdot k_a \cdot L^2 \cdot (c - c^{sat}) \tag{2.17}$$

$$\frac{dL}{dt} = \frac{k_m \cdot k_a}{3 \cdot k_v \cdot \rho}(c - c^{sat}) \tag{2.18}$$

$$G = k_g \cdot (c - c^{sat}) \text{ with } k_g = \frac{k_m \cdot k_a}{3 \cdot k_v \cdot \rho} \tag{2.19}$$

where ρ is the mass density, $G = \frac{dL}{dt}$ is the growth rate and k_g is the growth rate constant.

As in the nucleation kinetic rate formula, Tavare (1995) expressed the overall growth rate with a simple empirical power-law relationship expressing the specific rate of the mass deposition as:

$$G = k_g \cdot (c - c^{sat})^g \tag{2.20}$$

where the growth kinetic rate order g is generally given between 0 and 3 [Tavare, 1995]. In this work, for modelling of $BaSO_4$ nanoparticle precipitation microemulsion system, the diffusional growth inside the water droplet can assumed to be negligible due to the very small droplet size and very rapid droplet fusion-fission events. Therefore, the growth kinetic order for surface integration–controlled growth g = 2 is used in accordance with Balydyga et al. (1995). The specific growth rate constant in microemulsion $k_{g,me}$ will be identified from the fitting of the simulated data to the experimental results (see chapter 5).

In the precipitation process, after the establishment of a certain level of supersaturation, nucleation and growth processes are occuring simultaneously. For that reason, the particle size depends on the ratio between nucleation and growth rate.

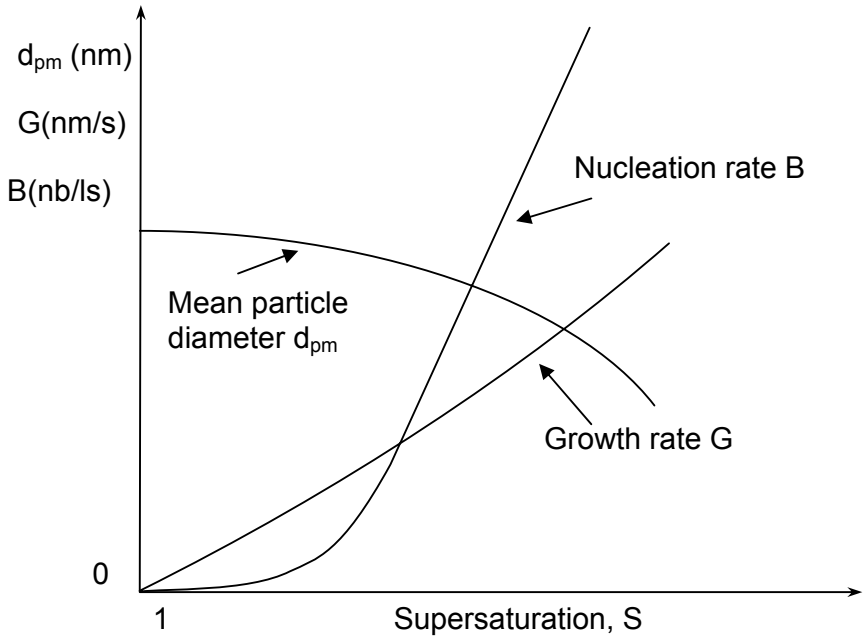

Fig. 2.8: Scheme of the dependencies of the nucleation rate B, growth rate G and the mean particle diameter d_{pm} on the supersaturation [redrawn from Nyvilt et al., 1985].

In Fig. 2.8, the nucleation rate, growth rate and particle size are shown as functions of the supersaturation. It can be seen that by decreasing the supersaturation ratio, the growth process will be dominating which will lead to bigger particle sizes. On the other hand when the supersaturation ratio is increasing, the nucleation rate will be dominating which results in a larger number of smaller particles.

2.3 Precipitation in Microemulsions

2.3.1 Properties of Microemulsions

A mixture of the three components, water, non-polar oil, and surfactant exhibits a complex phase behaviour and a variety of interesting microstructures. The systematic investigation of such ternary systems was done for over 45 years, the first time defined by Schulman et al, (1959) with special emphasis on the phase behaviour, the interfacial tension,

the microstructure, and the droplet dynamics. Fig. 2.9 illustrates possible qualitative structures being formed in the composition triangle of the ternary mixture water/oil/surfactant.

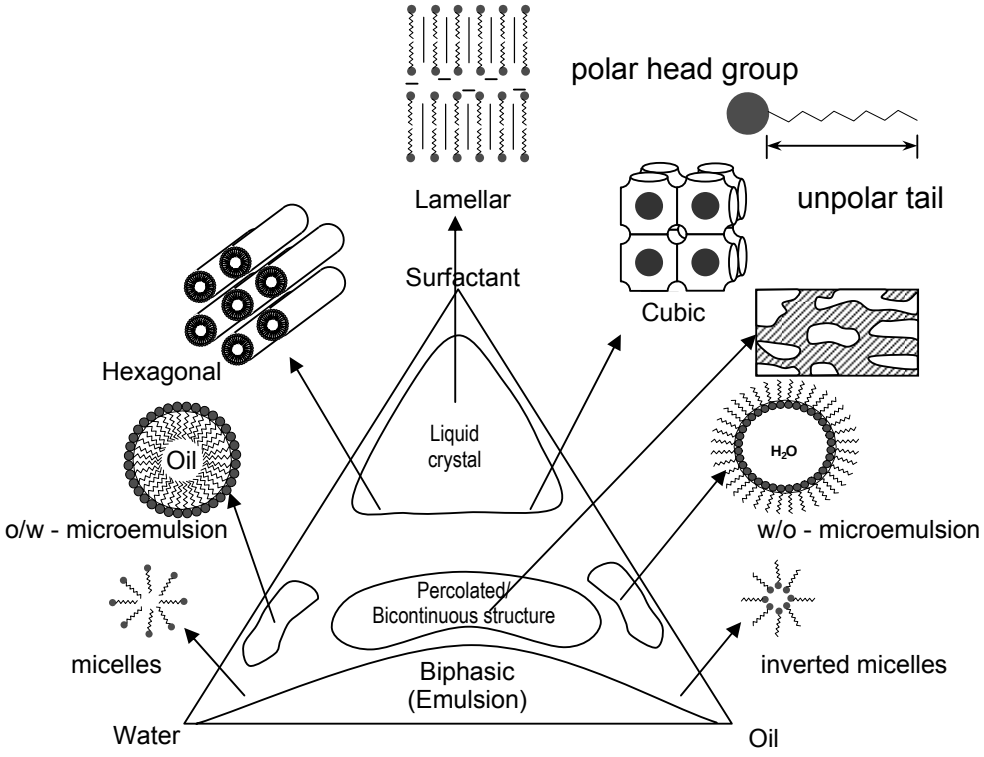

Fig. 2.9: Schematic diagram illustrating the phase behaviour of an oil/water/surfactant system [modified from Moulik and Paul, 1998].

From Fig. 2.9, it can be seen that micelles and bilayers are the building blocks of the self-assembly structure within the ternary mixture of surfactant, oil, and water. One can divide the microstructures into two main groups [Holmberg et al., 2003]: (1) those that are built of limited or discrete self-assemblies, which may be characterized roughly as spherical objects (micelles/nanodroplets belong to this structure type). (2) Infinite or unlimited self-assemblies where the aggregates are connected over macroscopic distances in one, two, or three dimensions [Tadros, 2005]. The hexagonal phase is an example of one-dimensional continuity, the lamellar phase of two-dimensional continuity, whereas cubic and bicontinuous structure are examples of three-dimensional continuity. The above mentioned three-dimensional self-assemblies are referred to as liquid crystalline structures since they behave as a highly viscous fluid with a microscopic crystal structure. Those structures, however do

not concern us much, because the experiments done in this work were carried out in spherical micelles and nanodroplets of microemulsions.

Within specific composition domain and at certain conditions (e.g. temperature), discrete-self assemblies which are thermodynamically stable and optically transparent ternary mixtures, known as micelles and microemulsions, are spontaneously formed. On a microscopic scale, in these macroscopically transparent mixtures the surfactant molecules separate into two immiscible liquids (oil and water). A microemulsion is defined as a liquid solution of swollen micelles that is optically isotropic and thermodynamically stable. It can be formed from two types of micelles [Tadros, 2005]. In normal micelles with an oil core and the surfactant polar head groups directed towards aqueous medium which can be seen in the water-rich triangle corner. The second type of micelles is an inverted micelle (formed in non-polar media) with a water core containing the polar head groups and the hydrocarbon tails have contact with a continuous oil phase which can be seen in the oil-rich corner of the triangle in Fig. 2.9 above. Normal micelles can solubilize more oil in the hydrocarbon core, forming swollen micelles which are oil-in-water (o/w) microemulsions. Inverted micelles can solubilize more water in the water core, forming water-in-oil (w/o) microemulsions. Roughly, the dimensions and physical characteristic of micelles, microemulsions, and macroemulsions are given in Table 2.5.

Table 2.5 Dimensions and characteristics of different emulsion systems.

Systems	**Droplet Size**	**Characteristics**
Micelles	r < 5 nm	-transparent
Microemulsions	r ~ 5-10 nm r ~ 10-50 nm	-transparent -translucent -the interfacial surface area $\approx 10^5$ m^2 per liter
Macroemulsions	r > 50 nm	-opaque and milky

Microemulsion systems have several interesting properties such as ultra-low interfacial tension, excellent solubility and an extremely large surface area which might be very interesting for certain industrial applications [Chhabra et al., 1997]. Several examples for the application of microemulsion systems include cosmetics [Aikens and Friberg, 1999], foods [Engström and Larsson, 1999], pharmaceuticals [Mamlstein, 1999], and tertiary oil recovery [Pillai et al., 1999]. In reaction engineering, microemulsions were also used as reaction media

for organic and enzymatic synthesis [Orlich and Schomäcker, 2001], polymerization [Candau, 1999], and the production of nano-scale materials [Rauscher et al., 2005].

Kahlweit et al., (1990) have investigated the phase behaviour of ternary oil/water/non-ionic surfactant (water/n-Alkane/C_iE_j) mixtures in detail. Such a ternary system is usually represented in a Gibbs phase triangle for water, oil, and surfactant at constant pressure and specific temperature. The composition of the microemulsion system is usually specified by the parameters α and γ [Kahlweit et al., 1990]. α is the weight fraction of oil in the binary mixture of oil and water:

$$\alpha = \frac{m_{oil}}{m_{oil} + m_{water}}. \tag{2.21}$$

γ stands for the weight fraction of surfactant in the ternary mixture:

$$\gamma = \frac{m_{surfactant}}{m_{oil} + m_{water} + m_{surfactant}}. \tag{2.22}$$

Taking into account the temperature as well, the triangle expands to an upright phase prism (see Fig. 2.10)

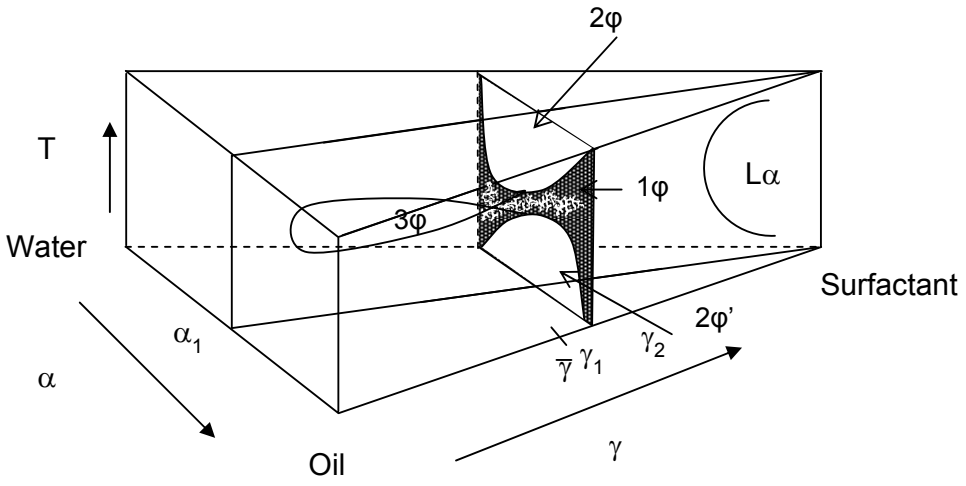

Fig. 2.10: Schematic phase prism in terms of temperature and composition [redrawn from Schubert and Kaler, 1996].

In Fig. 2.10, a vertical section plane is shown schematically at $\alpha = \alpha_1$. Fig. 2.11 below shows this section in detail at varying surfactant mass fraction γ.

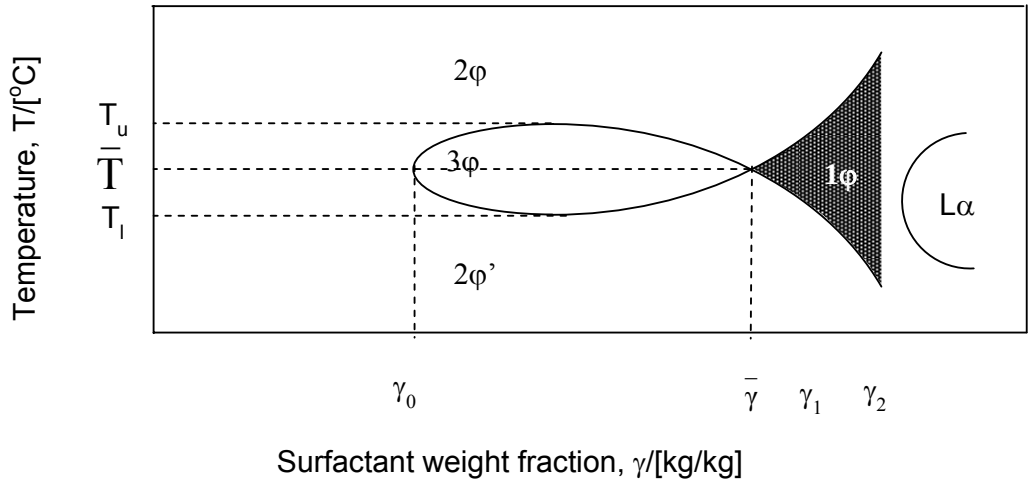

Fig. 2.11: Schematic pseudo-binary phase diagram at $\alpha = \alpha_1$ as a function of temperature and surfactant weight fraction γ [redrawn from Schubert and Kaler, 1996].

Considering the mixture as a function of temperature at intermediate surfactant weight fraction, for low temperatures the mixture forms two phases where the oil-in-water microemulsion is in equilibrium with an excess of oil (2φ'). At the same weight fraction but for a medium temperature, a single-phase microemulsion is formed (1φ). Finally, for higher temperatures two phases are formed again but now there is a water-in-oil microemulsion in equilibrium with an excess water phase (2φ). It is also possible to observe the formation of liquid crystalline phases (e.g. lamellar phase Lα) at a high non-ionic surfactant weight fraction γ.

The phase boundaries between the upper and the lower two-phase region and the one-phase region form the so-called "fish-tail". At even lower weight fractions of surfactants γ_0, three phases are observed inside the body of the fish form and the phases are in the sequence 2φ'→3φ →2φ (with temperature elevations). These three phases (3φ) consist of both oil-rich and water-rich phase microemulsion in equilibrium with a single-phase microemulsion. The temperature range where the mixture separates itself into three phases is defined as: $\Delta T = T_u - T_l$ where T_u denotes the temperature of upper boundary and T_l the temperature of the lower boundary. The surfactant weight fraction at the head of the fish is called γ_0. At the weight fractions lower than γ_0 ($\gamma < \gamma_0$) two phases are always achieved.

The surfactant concentration γ at the intersection between the fish body and the fish tail represents the efficiency of the surfactant to homogenize the same amount of water and oil

and is denoted by $\bar{\gamma}$. The temperature value at $\bar{\gamma}$ is represented by $\bar{T}$. The temperature $\bar{T}$ is often called phase inversion temperature. At this temperature the system is in a "balanced state" (the surfactant film has a zero mean curvature resulting in a bicontinuous structure). Our main purpose for nanoparticles synthesis is to use a single-phase microemulsion. An additional insight can be obtained from perpendicular to the plane on which the fish-like form can be seen in the range $\gamma_1<\gamma<\gamma_2$. In that plane there is a narrow channel of the single-phase microemulsion that evolves from the water-rich to the oil-rich side of the phase diagram as can be seen in Fig. 2.12.

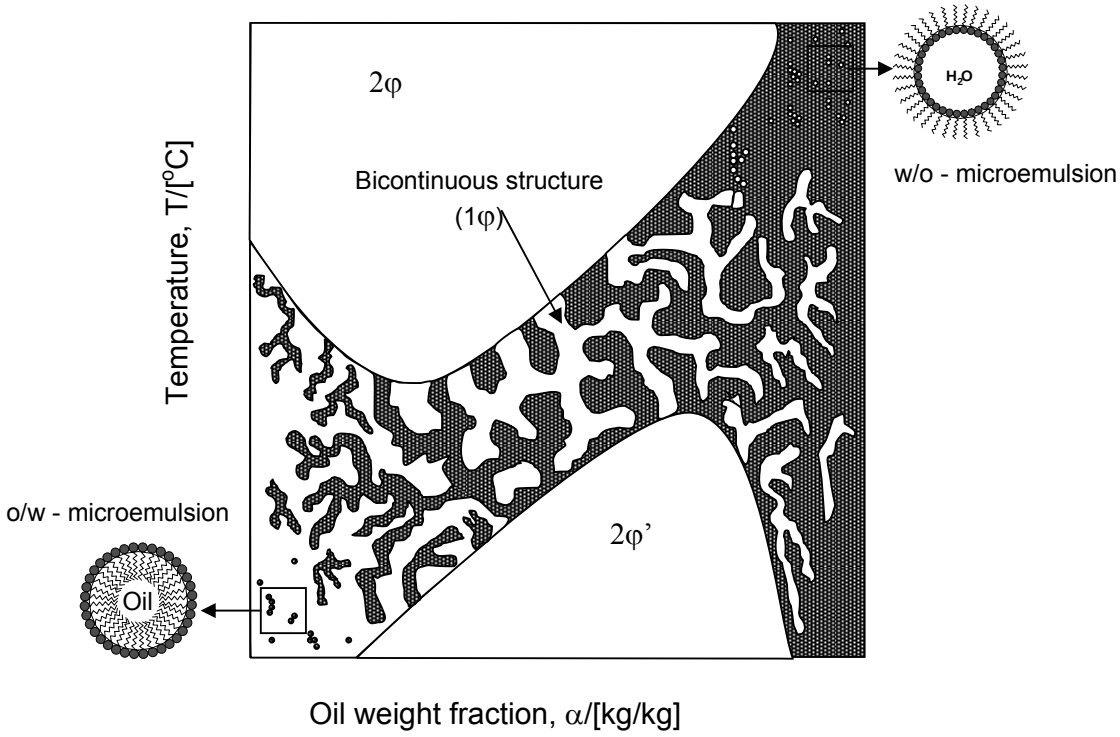

Fig. 2.12: Schematic section of phase prism of a ternary mixture surfactant/oil/water at constant surfactant weight fraction γ ($\gamma_1<\gamma<\gamma_2$). [Redrawn from Schwuger et al., 1995].

As can be seen more clearly in Fig. 2.12, on the water-rich side, the mixtures consist of a stable dispersion of oil droplets in water (o/w microemulsion), which will coagulate above a certain upper temperature. A sponge-like structure is formed if the mixture contains approximately equal amounts of water and oil, i.e. α = 30 to 70 % [Schwuger et al., 1995]. On the oil-rich side, dispersed water droplets are formed (w/o microemulsion), which also will coagulate above a certain upper temperature. A narrow composition channel for the single-

phase microemulsion as homogenous isotropic solution can be found in which the weight fraction of oil α can be varied from 0 to 100 %. Different two phase regions are bordering this single-phase region in which the surfactant is dissolved either in the aqueous bottom phase (2φ') or in the organic top phase (2φ). This narrow channel is considered as the main focus for investigation, since the operating region for nanoparticles synthesis is determined using this information.

For the case of the ternary system, microemulsions need surfactants as a dispersant for oil-in-water or water-in-oil droplets. Several types of surfactants are often used for preparing microemulsion systems (Table 2.6)

In this study the type of non-ionic surfactant being used is a alkylpolyglycolether (ethoxylated alcohol). Ethoxylation of alcohols, which usually consist of 6 to 16 carbon atoms, react in a pressurised vessel by introducing ethylene oxide into the stirred alcohol. This reaction is exothermic and catalyzed by acids or more often by bases, e.g. potassium hydroxide. The result from this ethoxylation process is a mixture of reaction products with different degrees of ethoxylation and a residual amount of un-reacted alcohol. The non-ionic technical surfactant Marlipal O 13/40 (Sasol, Marl-Germany) is formed by a reaction of ethylene oxide with iso-tridecanol, as shown in Fig. 2.13. Marlipal O 13/40 contains an average of 4 moles (n = 4) of ethylene oxide per mole alcohol.

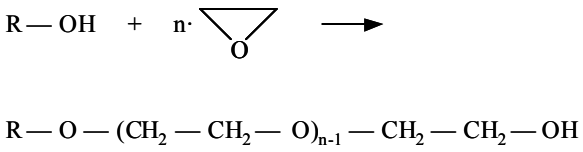

Fig. 2.13: Formation reaction of Marlipal O 13/40 non-ionic surfactant

Table 2.6 Surfactants which are often used in microemulsion-mediated nanoparticle synthesis [Osseo-Asare, 1999]

Type of surfactant	Name of surfactant	Chemical formula
Anionic	Aerosol OT (AOT); Sodium bis (2-ethylhexil sulfosuccinate)	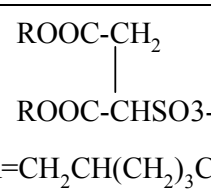
	Potassium oleate	$CH_3\ (CH_2)_7CH = CH(CH_2)_7COO^-K^+$
	Sodium dodecyl sulphate (SDS)	$C_{12}H_{25}OSO_3^-Na^+$
Cationic	Dioleyl phosphoric acid (DOLPA)	$R_1 = C_{12}H_{25}$; $R_2 = CH_3$ 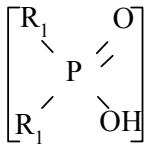
	Didodecyldimethylammonium-bromide (DDAB)	$R_1 = C_{12}H_{25}$; $R_2 = CH_3$ 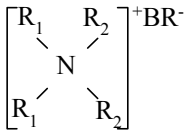
	Cethyltrimethyl ammonium-bromide (CTAB)	$R_1 = C_{16}H_{25}$; $R_2 = CH_3$ 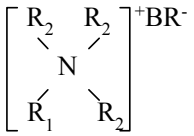
	Cethyldimethylbenzylammonium-bromide (CDBA)	$R_1 = C_{16}H_{25}$; $R_2 = CH_3$ 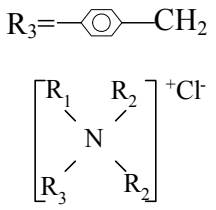

(to be continued)

(continued)

Type of surfactant	Name of surfactant	Chemical formula
Non-ionic	Polyoxethylene-(n)-nonylphenyl-ether, (Triton). [n = 4 (Triton N-42); n = 5 (Triton N-57); n = 6 (Triton N-60); n = 9-10 (Triton N 101)]	C_9H_{19}–⬡–$(OCH_2\text{-}CH_2)_nOH$
	Polyoxethylene-(n)-octylphenyl-ether, (Triton). [n = 1 (Triton X-15); n = 3 (Triton X-35); n = 5 (Triton X-45); n = 9-10 (Triton X 100)]	C_8H_{17}–⬡–$(OCH_2\text{-}CH_2)_nOH$
	Polyoxethylene-(n)-dodecylphenyl ether	$C_{12}H_{25}$–⬡–$(OCH_2\text{-}CH_2)_nOH$
	Sorbitan monooleate (SPAN 80)	$R_1 = (CH_2)_7CH = CH(CH_2)_7CH_3$ 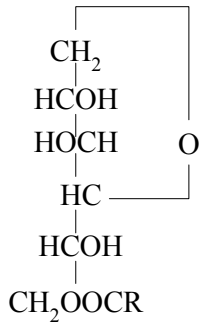
	Alkylpolyglycolether (Marlipal) (n = 4, Marlipal O 13/40; n = 5, Marlipal O 13/50; n = 6, Marlipal O 13/60)	$RO(CH_2\text{-}CH_2\text{-}O)_{n-1}\text{-}CH_2\text{-}CH_2\text{-}OH$

2.3.2 Synthesis of nanoparticles in microemulsions

Syntheses of nanoparticles in microemulsion systems can be carried out inside the emulsion droplets which act as nanoreactors. The major advantages by using microemulsions as reaction media are:

- The ability of controlling the size and particle distribution due to uniform micro-mixing resulting in rapid fusion and fission phenomena of the nanodroplets.

- The creation of a high interfacial surface area (the interfacial surface area is around 10^5 m^2 per litre of microemulsion)
- The low sensitivity with respect to hydrodynamics in the reactor during the reaction.

In general there are two methods for nanoparticle synthesis using microemulsion techniques [Osseo-Asare and Arriagada, 1990]. The first method is called the one-microemulsion method. This method includes "energy triggering" and the "one-microemulsion plus reactant" method. In the energy triggering method, the reaction is initiated by implementing a triggering agent into the single microemulsion which contains a reactant precursor (Fig. 2.14-1a). This fluid system is activated in order to initiate the reactions that eventually lead to particle formation. For example, pulse radiolysis and laser photolysis were used to trigger the preparation of nano-size gold particles [Kurihara et al., 1983]. Besides this energy triggering method, the other method is the one microemulsion – plus reactant method. In this method, the reaction is initiated by directly adding the pure reactant (liquid or gaseous phase) into the microemulsion containing another reactant (Fig. 2.14-1b). The ions e.g. metals are first dissolved in the aqueous phase of a w/o microemulsion. Then the precipitating agent, in the form of an aqueous solution (e.g salt NaOH) or a gas phase [e.g NH_3(g), $CaCO_3$ (g)], is fed into the microemulsion solution. Another scenario within the one microemulsion – plus reactant method is that the precipitating agent is first dissolved in the polar core and a metal-containing solution (e.g organic precursor) is subsequently added into the microemulsions. The one-microemulsion method generally is driven by the diffusion-based process, since the second trigger/reactant is diffusing into the droplets containing the reactant in the used microemulsion.

The second method which is also often used for preparing nanoparticles is the two-microemulsion method. Two reactants, A and B which are dissolved in the aqueous nanodroplets of two separate microemulsions are mixed as shown in Fig. 2.14-2. This method relies on fusion-fission events between the nanodroplets. A list of the microemulsion nanoparticle preparation methods is given in Table 2.7. Schematic illustrations are presented in Fig. 2.15.

Table 2.7 Methods of nanoparticles synthesis in microemulsion systems

Methods		**Materials**	**Literature source**
One-microemulsion method	Energy triggering	$Al(OH)_3$	Dutta and Robbins, 1989
		Gold	Kurihara et al., 1983
		FeOOH	O'Sullivan et al., 1994
	One microemulsion plus reactant	$CaCO_3$	Kandori et al., 1987
		FeOOH	Inouye et al., 1982
		Fe_2O_3	Ayyup et al., 1988
		Vinyl polimer	Burban et al., 1995
		Silica	Watzke and Dieschbourgh, 1994
		Silica	Espiard et al., 1995
		Silica	Chang and Fogler, 1996
Two -microemulsions method		$BaSO_4$	Adityawarman et al., 2005
		$CaCO_3$	Rauscher et al., 2005
		Ni_2B,Co_2B,	Nagy, 1999
		Fe_3O_4	Liz et al., 1994

In this work, the two-microemulsion method will be used for the synthesis of $BaSO_4$ nanoparticles in a microemulsion. In order to produce the nanoparticles, two microemulsions carrying the appropriate reactants are mixed. The chemical reaction starts when there are fusion-fission event between the droplets as a prequisite for the mixing of the reactants. After the chemical reaction has taken place at the nanodroplets and produced critical number pf molecules C for nucleation (N_{crit}), this results in nuclei formation and furthermore leads to the growth of nanoparticles. The mechanism of the synthesis of nanoparticles in nanodroplets by the two-microemulsion method is shown in Fig. 2.14.

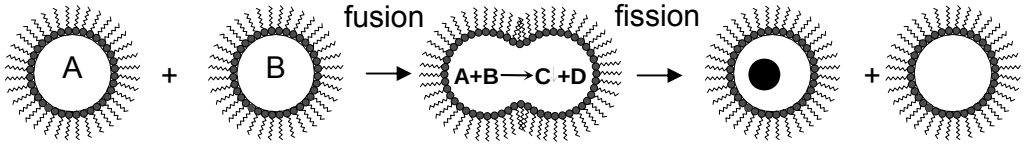

Fig. 2.14: Nanoparticle formation mechanism in microemulsion droplets.

The very small size and rapid fusion-fission of the water droplets lead to a very homogenous mixing of the two reactants. This particular mixing behaviour distinguishes the

microemulsion clearly from the bulk phase precipitation, where inhomogeneous mixing leads to different concentrations resulting in a broad particle size distribution and larger particles.

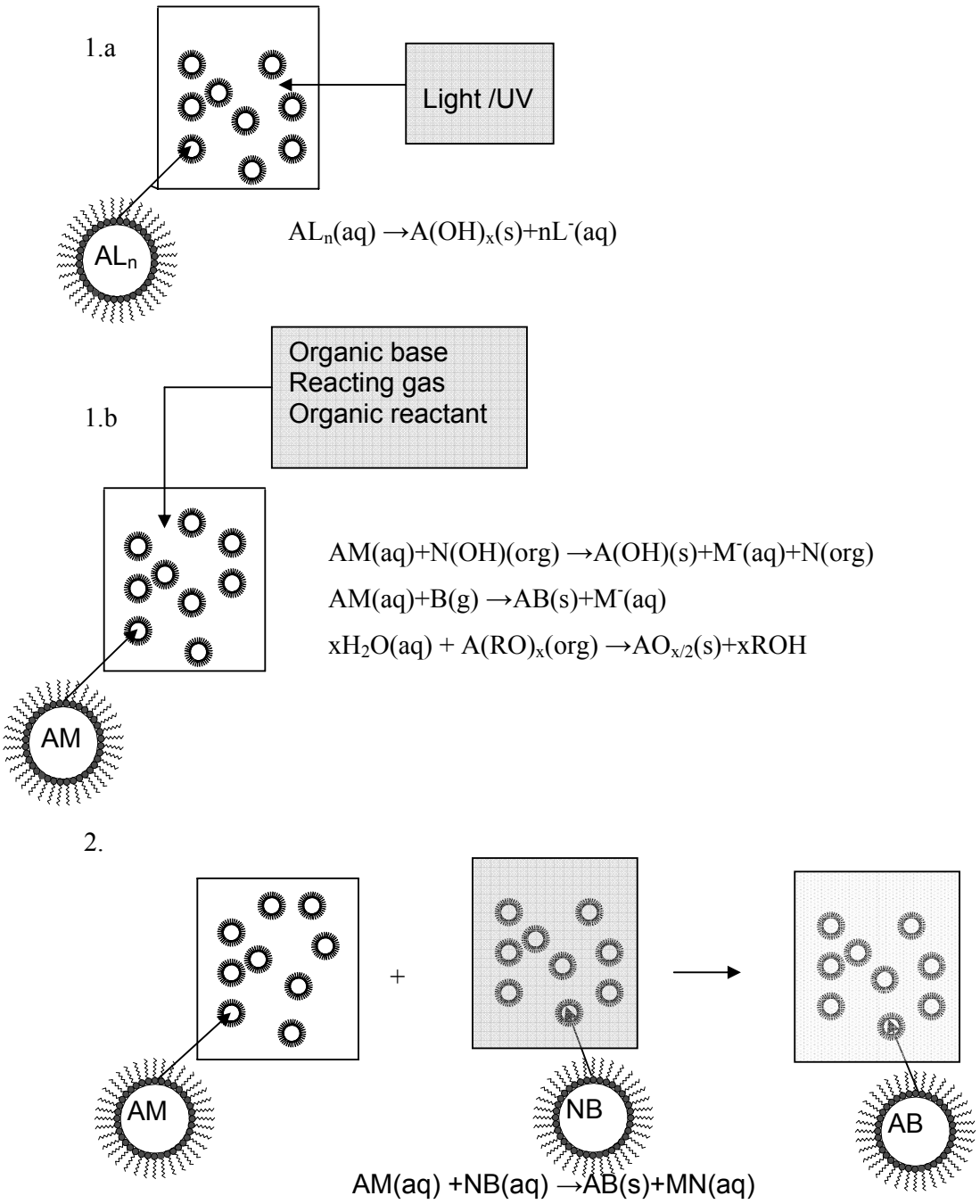

Fig. 2.15: Different methods of nanoparticle synthesis in microemulsions: 1.a One-microemulsion method: Energy triggering method. 1.b One-microemulsion method plus reactant method. 2. Two-microemulsions method. Cations: A,N, Anions: B,M [redrawn from Osseo-Asare and Arriagada, 1990].

A fundamental model that explains the formation of monodisperse particles in a homogeneous reaction system has been proposed by Lamer and Dinegar (1950). According to this model all the particles nucleate in a very short time interval. After this nucleation step particle growth occurs. The particle growth is kinetically controlled by the diffusion of the liquid molecules from the solution towards the particle surface. The course of this precipitation reaction is illustrated in Fig. 2.16 which shows a schematic plot of the concentration of the product molecules C versus time. The comparison of the course of dissolved molecules C concentration c_c in the two processes (microemulsion precipitation and bulk phase precipitation) also can be seen in Fig. 2.16.

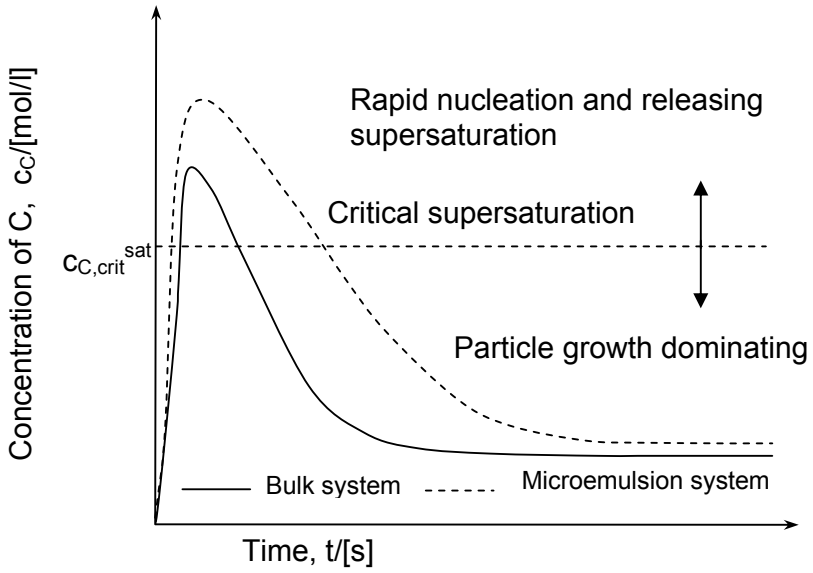

Fig. 2.16: Schematic representation of the course of concentration C during microemulsion and bulk phase precipitation in case of batch operation [redrawn from Schmidt, 2000].

As shown in Fig. 2.16 above, as soon as the liquid molecules C are formed by the chemical reaction, the concentration c_C increases rapidly and exceeds a critical value $c_{C,crit}^{sat}$ leading to spontaneous nucleation. Due to the parallel and competitive occurrence of nucleation and subsequent growth, c_C reaches a maximum. After this maximum c_c begins to decrease with the time and drops below $c_{C,crit}^{sat}$. Nucleation occurs only in the period where c_C is higher than $c_{C,crit}^{sat}$. The decrease of c_C after nucleation is mainly governed by the diffusion-controlled growth of the formed nuclei. In the microemulsion system due to the droplet fusion-fission process and the very small size of the nanoreactors, the nucleation process will take longer and c_C will exceed $c_{C,crit}^{sat}$ more than in a bulk system, which will lead to a higher number of particles with an accordingly smaller particle diameter compared to the bulk

system. The high concentration of liquid molecules C inside the nanodroplets corresponds to a higher value of the supersaturation S. In Fig. 2.17, a typical supersaturation ratio of $BaSO_4$ molecules inside 5 nm water droplets can be seen.

The supersaturation ratio of $BaSO_4$ molecules S inside the water droplets is calculated by

$$S = \frac{c_{BaSO_4}}{c_{BaSO_4}^{sat}} = \frac{N_{BaSO_4}}{k_{vd} \cdot N_A \cdot d_{drop}^{3} \cdot c_{BaSO_4}^{sat}}, \tag{2.23}$$

where c_{BaSO_4} is the concentration of barium sulphate molecules, $c_{BaSO_4}^{sat}$ is the concentration of barium sulphate molecules at saturation, k_{vd} is the droplet shape factor, and N_{BaSO_4} is the number of $BaSO_4$ molecules inside one droplet. It shows that the expected behaviour that an increase of $BaSO_4$ molecule inside droplet leads to a higher supersaturation ratio.

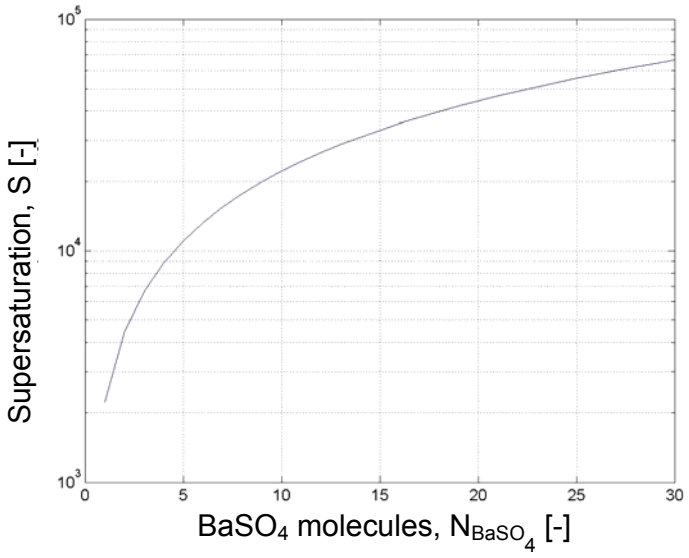

Fig. 2.17: Supersaturation ratio S inside the 5 nm water droplets.

Table 2.8 below presents several examples of nanoparticles where the microemulsion technique was already applied successfully.

Table.2.8 Nanoparticles synthesis in microemulsion systems [Niemann et al, 2006].

Material class	**Materials**	**Particle size [nm]**	**Literature source**
Bimetals	Pd-Au	n.a	Sato et al., 2002
	Pd-Pt	6…14	Wu et al., 2001
Borides	Ni_2B,Co_2B, NiCo	2…7	Nagy, 1999
Carbonates	$CaCO_3$	48…120	Kandori et al., 1987
	$BaCO_3$	54…165	Kandori et al., 1988
Halides	AgCl,AgBr,AgI	2…6	Sato et al., 1996
	AgBr	5…20	Monnoyer et al., 1995
Metals	Ag	0.8…14	Petit et al., 1993
	Pd	4…7	Lade et al., 2000
	Pt,Pd,Rh,Ir	3…5	Boutonnet et al., 1982
Metal oxides	TiO_2	≈ 2	Li and Wang, 1999
	TiO_2	≈ 3	Hirai et al., 1993
	ZnO	5…40	Hingorani et al., 1993
Pharmaceuticals	Limesuflide	4…6	Debuigne et al., 2001
Polymers	Styrene	30…45	Chern and Tang, 2003
Semiconductors	Ag_2S	1.5…10	Pileni et al.,1996
	Ag_2S	1.5…14	Motte et al.,1996
	CdS, ZnS	2.2…3.8	Hirai et al.,1994
	ZnSe	≈ 8	Karanikolos et al.,2003
	MoS_3	10…80	Boakye et al.,1994
	CdS	< 1.4	Lianos et al.,1987
Silica	Silica	2…44	Chang and Fogler, 1996
	Silica	90…260	Esquena et al., 1997
	Silica	32…75	Arriagada and Osseo-Asare, 1999
Sulphates	$BaSO_4$	5…20	Qi et al.,1996
	$BaSO_4$	10…20	Ivanova et al., 2001

Osseo-Asare and Arriagada, (1990) explained the important factors which influence the synthesis of nanoparticles using water-in-oil microemulsion techniques :

- **Phase behaviour:** This parameter is influenced by the presence of dissolved reactants in the aqueous phase which is important for the determination of the operating region for precipitation [Qi et al., 1996, Ivanova et al., 2001, Rauscher et al., 2005, Adityawarman et al., 2005].
- **Droplet exchange rate:** Microemulsions can exchange their water cores via fusion and fission events. The droplet exchange rate constant k_{ex} is reported to be 10^6-10^8 l mol^{-1} s^{-1} for the AOT/Iso-octane system [Fletcher et al., 1987]. The importance of this parameter in particle synthesis is due to the possible increase or decrease in the chemical reactivity of ionic species, which is usually observed in particles synthesis [Bagwe and Khilar, 2000, Natarajan et al., 1996 and Ingelsten et al., 2001]. It has also been recognised that such effects are highly specific with regard to the chemical species, the type of surfactants, and the reactions. For example, Bagwe and Khilar, (2000) demonstrated through the formation of AgCl nanoparticles in AOT-microemulsions that a higher exchange rate led to a smaller size of the particles. By using time-resolved luminescence quenching (TRLQ) Lade et al. (2000) reported that a Marlipal-cyclohexane-water microemulsion at $\alpha = 0.95$ and $\gamma = 0.15$ has a droplet exchange rate constant of $3x10^9$ l mol^{-1} s^{-1} and will increase with increasing temperature.
- **Dynamic behaviour of surfactant aggregate** which is usually observed for the size and the mass of a single product particle is much larger than attributable to the droplet size. [Kandori, 1987, Hopwood and Mann, 1997, Rausher et al., 2005, and Adityawarman et al., 2005]. This observation strongly suggests that the interface lability and droplet exchange rate are of major importance [Tojo et al., 1998].
- **Droplet occupancy numbers:** The amount of the droplets inside the microemulsion in a given system allows the determination of an average number of molecules per droplet. Atik and Thomas (1981), Hirai et al. (1993), Bandyopadhyaya et al. (1997), Nagy (1999), present that the distribution of the molecules over the nanodroplets follows a Poissonian distribution. Smaller nanoparticles are performed at high occupancy numbers as a result of a faster nucleation rate given by a high probability of the interaction between two reactive ions [Qi et al., 1996]. On the contrary, fewer and larger nanoparticles are formed at a lower occupancy number as a smaller number of nuclei are formed.

Chapter 3
Materials, set-up, characterization and measuring techniques

3.1 Chemicals

All chemical substances being used for the experimental investigations in this work are listed in Table 3.1 below:

Table 3.1 Chemicals.

Chemical	Source	Purity
$BaCl_2$	Merck	99.99%
K_2SO_4	Applichem	99.5%
Cyclohexan	Merck	99.9%
Marlipal O 13/40 Marlipal O 13/60 Marlipal O 13/80	Sasol	11.5% fatty-alcohol fraction 5.8% fatty-alcohol fraction 5.8% fatty-alcohol fraction
KI	Merck	99%
I_2	Schering-Kahlbaum	99%
$Na_2S_2O_3$	VEB pharma	99%

All of these substances were used without any further purification processes. Cylohexane is chosen as continuous phase. Due to its low boiling point of 81.2 ^oC cyclohexane can be easily removed from the solution by evaporation and possibly recycled in a larger-cale technical plant. The used surfactant Marlipal O13 is a commercial surfactant of alkylpolyglycolether-type and is available in large quantities on the market. The synthesis of Marlipal surfactants takes place by the reaction of iso-tridecanol and ethylene oxide. Depending on the process conditions of the synthesis, various ethoxylation grades of the surfactant can be produced. For example, Marlipal O13/60 has an average ethoxylation grade of 6, which means it contains 6 moles of ethylene oxide per mole alcohol (see Fig. 3.1).

After the synthesis, unreacted alcohol remains in the reaction mixture. The quantity of this unreacted alcohol decreases with ethoxylation grade. For oil components we use n-alkanes (cyclohexane).

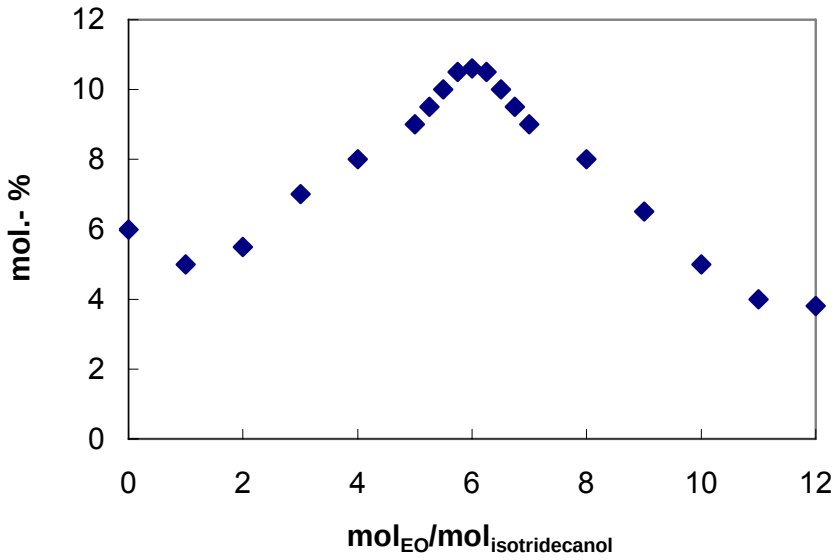

Fig. 3.1: Distribution of ethoxylation grade (ethoxy groups pro alcohol) for the surfactant Marlipal O13/60 [redrawn schematically from Schmidt, 2000].

3.2 Reactor set-up

In order to ensure reproducible synthesis conditions and to study the influence of different operating parameters on the bulk-phase/microemulsion precipitation, a standardized reactor design was used. A semi-batch process scheme was utilized for the synthesis of $BaSO_4$ particles from bulk phase as well as microemulsions precipitation (see Fig. 3.2).

The reactor consisted of a 1000 ml glass tank supplied with a water jacket for temperature control by means of Lauda thermostat. The tank was equipped with eighteen baffles and a six-blade Rushton turbine impeller placed at one-third of the initial liquid height H_0 from the bottom. The feed input was located 2 cm below the initial liquid height H_0. One reactant was dosed by a peristaltic pump into the reactor. All information of the experimental set-up is listed in Table 3.2 and illustrated by Fig. 3.2 and Fig. 3.3.

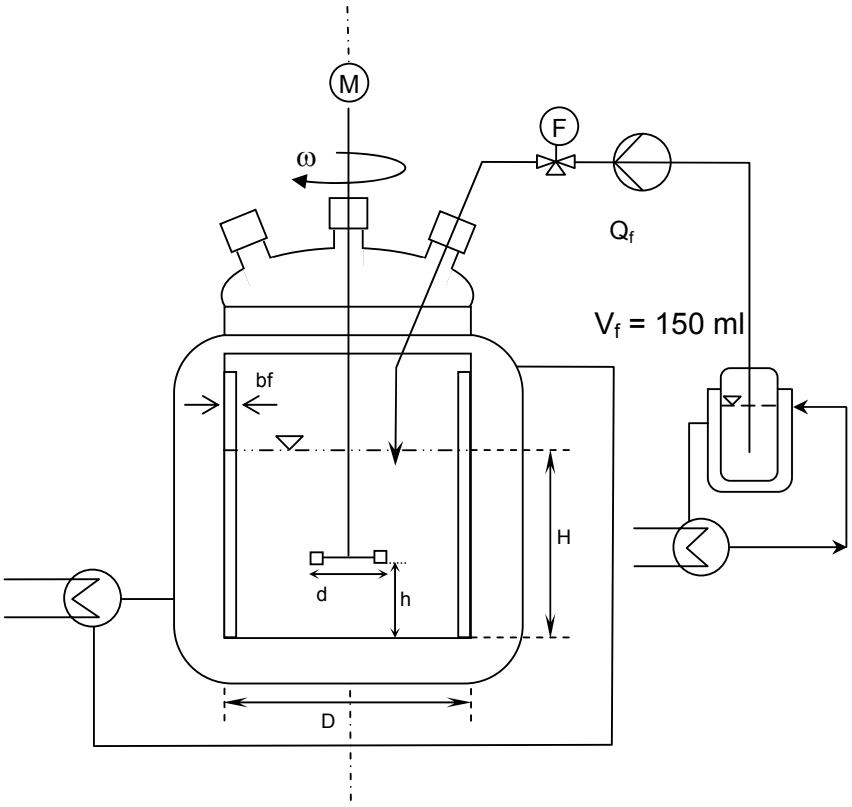

Fig. 3.2: Schematic of the semibatch stirred tank reactor used for the experiments

Table 3.2 Experimental set-up.

Reactor	**Configuration**
Stirrer position	h = H/3 from the bottom
Liquid height	H ≈ 2.5 cm for microemulsion precpitation H ≈ 11.8 cm for bulk precipitation
Inner diameter	D = 10 cm
Number/diameter of baffles	18 /0.5 cm
Reactant volume	V_r = 150 ml for microemulsion precipitation V_r = 700 ml for bulk precipitation
Feeding volume	V_f = 150 ml for microemulsion precipitation V_f = 150 ml for bulk precipitation
Stirring rate	ω = 50…800 min^{-1}
Feeding rate	Q_f = 17.5…140 ml/min for microemulsion precipitation Q_f = 17.5…130 ml/min for bulk precipitation
Stirrer	
Number of blades	6 pitched blade Rusthon turbine
Diameter	d = 3 cm

a)

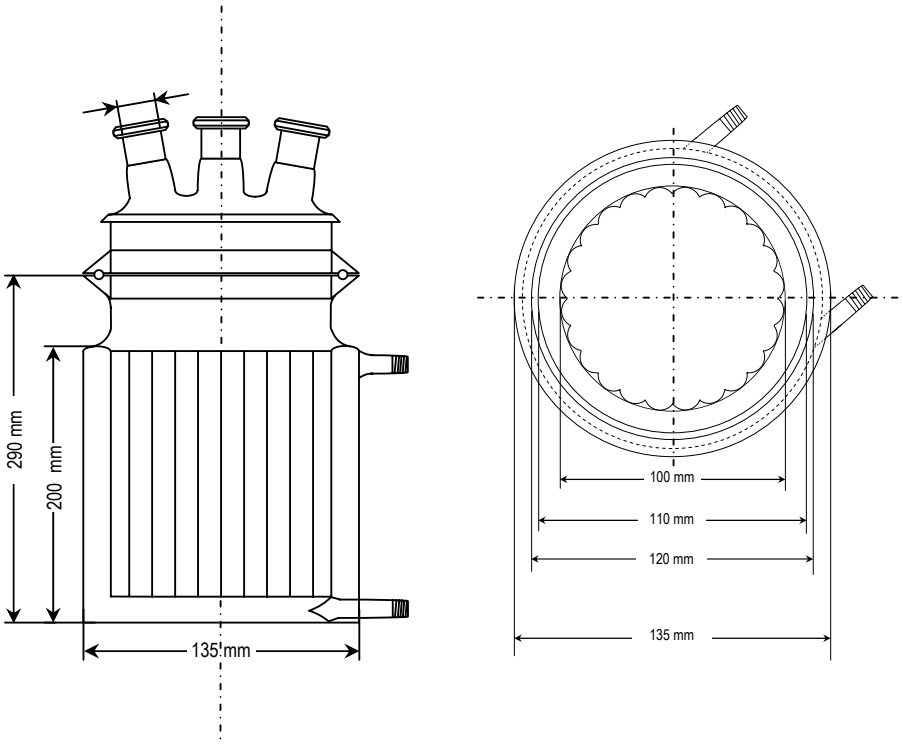

b)

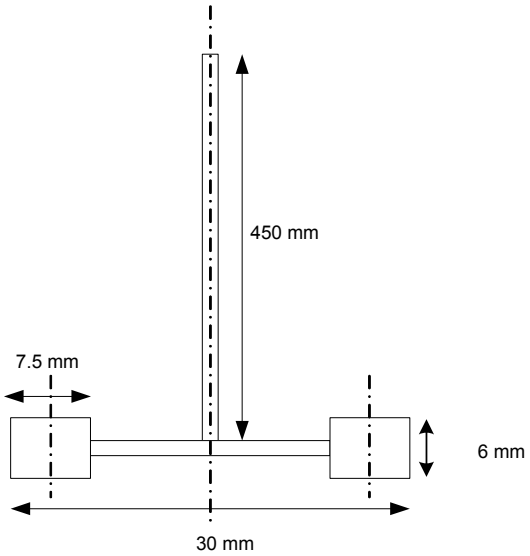

Fig. 3.3: Reactor (a) and stirrer (b) configuration.

In order to characterize the macromixing conditions in this reactor, mixing times at different liquid levels (H/D) and different stirring rates ω were measured applying the method of decolouration of iodine by reduction with sodium thiosulphate solution (see e.g. Kraume, 2003). The mixing time θ was determined when last streaks of iodine disappeared by using

the online-sensor of UV-spectrophotometer (Specord 50 from Jena-Analytik). Then, the dimensionless mixing time $\omega\theta$ can be plotted versus the modified Reynolds number N_{Re}.

$$N_{Re} = \frac{\omega \cdot d^2}{\upsilon} \tag{3.1}$$

where ω is the stirring rate, d is the stirrer diameter, ρ is the densitiy of the liquid, and υ is the kinematic viscosity. As can be seen from Fig. 3.4, for the chosen operating range for bulk and microemulsion precipitation, the Reynolds numbers are between 750 for ω = 50 min^{-1} and 12000 for ω = 800 min^{-1}.

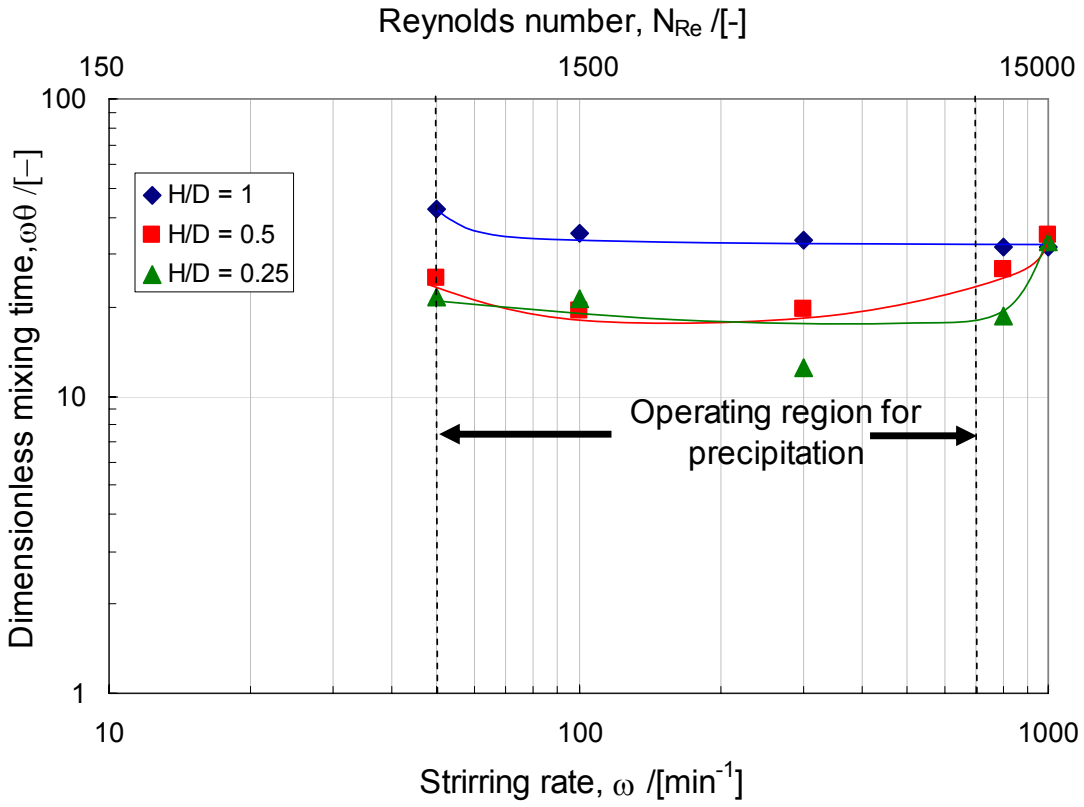

Fig. 3.4: Mixing time characteristics of the semi-batch reactor at different liquid levels (H/D).

At a stirring rate of ω =300 min^{-1}, the mean specific power input Pw can be estimated as follows [Zlokarnik, 1972]:

$$Pw = \frac{0.5 \cdot \omega^3 \cdot d^5 \cdot \rho}{V_r}, \tag{3.2}$$

where V_r is the volume of the reactant in the reactor which in all cases was 150 ml for microemulsion precipitation. From eq. 3.2, it can be calculated that the mean specific power input is P = 0.01 W/l.

3.3 Microemulsions characterization techniques

3.3.1 Optical observation

The microemulsion phase behaviour was investigated using a 20 – 25 ml glass cylinder equipped with a glass lid. The total mixture of one probe was around 10 gram. The mixture was weighted upon the composition of the oil weight fraction α and the surfactant weight fraction γ. The glass cylinder was placed in a thermostated chamber, which was equipped with a Lauda thermostat. When the probe was reaching the set temperature, visual observations to see the phase conditions were done. A single-phase microemulsion state was achieved when the mixture shows a clear, transparent, and isotropic solution. With temperature variation (decreased or increased), two or more phases were achieved and to be noted.

3.3.2 Viscosity

The viscosity of the (w/o) microemulsion with cyclohexane as continuous phase was measured by using a capillary viscosimeter (Viscoclock) from Schott. For temperature control and variation, the water bad was equipped with a Lauda thermostat. The viscosimeter was calibrated with cyclohexane for every temperature studied. The total mixture of one probe was around 25 gram. The mixture was weighted upon the composition of the oil weight fraction α and the surfactant weight fraction γ. The relative viscosity η_r was obtained by measurement of the flow time of the solution between two markers in the capillary for microemulsion and for cyclohexane. The relative viscosity is calculated by

$$\eta_r = \frac{\eta}{\eta_{cy}} = \frac{\rho_{me} \cdot t_{me}}{\rho_{cy} \cdot t_{cy}} \tag{3.3}$$

where ρ is the density and t is the flow time through the capillary. The indices indicate the microemulsion (me) and the continuous phase cyclohexane (cy). Since the density difference of the microemulsion and cyclohexane is relative small, the density in equation 3.3 is neglected and the relative viscosities are directly calculated from the flow time ratio.

3.3.3 Droplet size

For the determination of the droplet size distribution, dynamic light scattering measurements (Particle Size Analyzer LB-500, Horiba) were made at various compositions, which were weighted upon the composition of oil weight fraction α and surfactant weight fraction γ. The total mixture of one probe was around 5 gram. This measurement technique is

based on the detection of the intensity fluctuation of scattered light by the water droplets inside the microemulsion if they undergo Brownian motion [Tardos, 2005].

The Horiba LB 500 device is using a back scattering method to reduce the effect of multiple scattering in highly concentrated samples and is increasing the sensitivity at low concentrations. The particle size is from 3 nm to 6 μm. Small volume (2-5 ml) quartz cells with glass lid were used to allow to retain the sample for further testing or to minimize the amount of the microemulsion samples. The instrument was equipped with a temperature sensor to control the operating temperature in the range 25 to 70 ^{o}C.

3.4 Particle synthesis and characterization

3.4.1 Bulk phase precipitation

Precipitation of barium sulphate in the bulk phase was carried out in the semi-batch reactor. Barium chloride ($BaCl_2$) with a purity of 99.9% (from Merck) and potassium sulphate (K_2SO_4, from Applichem) with 99.5% chemical purity were used to prepare aqueous solutions. All chemicals were used without any further purification or conditioning. Water was purified and deionized using a Millipore treatment system. Precipitation experiments were carried out at 25 ^{o}C. Two series of set experiments were performed: (1) Effect of the stirring rate and the initial molar ratio on the particle size, (2) Effect of the feeding rate on the particle size. Two feeding modes were also investigated: either $BaCl_2$ as feed or K_2SO_4 as feed. In each run, a spontaneous precipitation was initiated by adding 150 ml V_f of 0.1 mol/l feed solution as a limiting reactant over a period of approximately 5 min to 700 ml V_r of the second reactant being already present in the tank. While the feed concentration was always kept constant at 0.1 mol/l, the solution concentration in the tank was varried from 0.021 to 0.107 mol/l to adjust the initial molar ratio of the two reactants. Hence both stoichiometric and non-stoichiometeric precipitation conditions tanks were investigated and the initial molar ratios of barium to sulphate ions R_N^0 were varied from 1 to 5 (K_2SO_4 as feed) and 1/5 to 1 ($BaCl_2$ as feed). In each case, the feeding reactant added to the tank solution 2 cm below the free liquid surface. The volumetric ratio R_v of the initial tank volume and the total feeding volume of reactants is defined by:

$$R_v = \frac{V_r}{V_f}. \tag{3.4}$$

The initial molar ratio R_N^0 is defined by:

$$R_N^0 = \frac{c_{BaCl_2,0}}{c_{K_2SO_4,0}} \cdot R_v \quad (\text{for } K_2SO_4 \text{ as feed}) \tag{3.5}$$

and

$$R_N^0 = \frac{c_{BaCl_2,0}}{c_{K_2SO_4,0}} \cdot \frac{1}{R_v} \quad (\text{for } BaCl_2 \text{ as feed}) \tag{3.6}$$

where the initial supersaturation values S_i for this study, as suggested by Wong et al. (2001), are estimated by assuming equal volumes of the feeding solution and the initial solution being present. Such values are given in Table 3.3. The initial supersaturation ratio S_i is calculated from

$$S_i = \sqrt{\frac{c_{BaCl_2,0} \cdot c_{K_2SO_4,0}}{K_{sp}}} . \tag{3.7}$$

Where K_{sp} stands for the solubility product of barium and sulphate ions (~ 1.1×10^{-10} mol^2/l^2) [Wong et al., 2001].

Table 3.3 Experimental conditions for $BaSO_4$ bulk precipitation.

Variation	Variation range	Experimental conditions
Initial molar ratio R_N^0 and stirring rate ω	R_N^0 = 1…5 (K_2SO_4 as feed) ω = 50 …800 min^{-1}	$c_{K_2SO_4,0}$ = 0.1 mol/l (fixed) $c_{BaCl_2,0}$ = 0.021 …0.107 mol/l V_f = 150 ml V_r = 700 ml S_i = 2184…4931 Q_f = 34 ml/min T = 25 °C
	R_N^0 = 1…0.2 ($BaCl_2$ as feed) ω = 50… 800 min^{-1}	$c_{BaCl_2,0}$ = 0.1 mol/l (fixed) $c_{K_2SO_4,0}$ = 0.021 …0.107 mol/l V_f = 150 ml V_r = 700 ml S_i = 2184…4931 Q_f = 34 ml/min T = 25 °C

(to be continued)

(continued)

Variation	Variation range	Experimental conditions
Feeding rate Q_f	$R_N^0 = 1$ (K_2SO_4 as feed) Q_f = 17.5 …130 ml/min	$c_{K_2SO_{4,0}}$ = 0.1 mol/l $c_{BaCl_{2,0}}$ = 0.021 mol/l V_f = 150 ml V_r = 700 ml S_i = 2184 ω = 300 min^{-1} T = 25 °C
	$R_N^0 = 1$ ($BaCl_2$ as feed) Q_f = 17.5 …130 ml/min	$c_{BaCl_{2,0}}$ = 0.1 mol/l $c_{K_2SO_{4,0}}$ = 0.021 mol/l V_f = 150 ml V_r = 700 ml S_i = 2184 ω = 300 min^{-1} T = 25 °C

During bulk phase precipitation, small suspension samples of about 10 ml were withdrawn, using a 50 ml pipette, from the reactor to analyse the evolution of the particle size with respect to time. Particle and size distribution measurement was performed by using the laser diffraction equipment CILAS 1180 L. The size distribution for this equipment should be in the range between 0.3 to 400 µm. The samples were diluted with a water volume of about 300 ml in a mixing chamber within the equipment in order to fulfill the concentration requirements. A further 2 min period was allowed after completion of the feed addition for final sampling to homogenize the content. Finally vigorous agitation at 500 min^{-1} was applied for around 1 min before samples were drawn from the suspension. Particle analyses are reported as the volume averaged mean particle diameter as well as the full particle size distribution.

3.4.2 Microemulsion precipitation

In the same way as in the bulk case, precipitation experiments of $BaSO_4$ nanoparticles in microemulsion were carried out in the same semi-batch reactor. The precipitation was performed in the single-phase microemulsion operating region being already identified in the investigation on phase behaviour of the microemulsion.

The microemulsion being applied for $BaSO_4$ nanoparticle precipitation in microemulsion systems consisted of cyclohexane (Merck with a purity of 99.9%) (as the continuous phase), the non-ionic technical surfactant Marlipal O 13/40 (Sasol Marl, Germany with a purity 98.0%) and water in which the reactants were dissolved.

Two water-in-oil microemulsions of identical composition containing different reactants in the aqueous phase were prepared. The volumes of the two reactant solutions were 150 ml. In the water phase of the first microemulsion, barium chloride ($BaCl_2$) with a purity of 99.9% (from Merck) was dissolved, while in the second microemulsion potassium sulphate (K_2SO_4, from Applichem) with 99.5% chemical purity was dissolved at varying concentrations. All chemicals were used without any further purification or conditioning. Water was purified and deionized using a Millipore treatment system. The feed reactant was dosed into the reactor by means of a peristaltic pump at a certain feeding rate Q_f. There were five variations of process parameters which had been investigated: the stirring rate, the feeding rate, the feeding sequence, the initial concentration, and the initial concentration ratio R_c^0 (see Table 3.4). The initial concentration ratio R_c^0 is defined by

$$R_c^0 = \frac{c_{BaCl_2,0}}{c_{K_2SO_4,0}} \,. \tag{3.8}$$

Table 3.4 Experimental conditions for $BaSO_4$ microemulsion precipitation.

Variation	Variation range	Experimental conditions
Feeding rate Q_f	$R_c^0 = 1$ ($BaCl_2$ as feed) Q_f = 17.5 …140 ml/min	$c_{K_2SO_4,0}$ = 0.1 mol/l $c_{BaCl_2,0}$ = 0.1 mol/l V_f = 150 ml V_r = 150 ml ω = 300 min^{-1} T = 25 °C α= 0.96 γ = 0.15
Stirring rate ω	$R_c^0 = 1$ ($BaCl_2$ as feed) ω = 50… 800 min^{-1}	$c_{K_2SO_4,0}$ = 0.1 mol/l $c_{BaCl_2,0}$ = 0.1 mol/l V_f = 150 ml V_r = 150 ml Q_f = 35 ml/min T = 25 °C α = 0.96 γ = 0.15

(continued)

Variation	Variation range	Experimental conditions
Feeding sequence	$R_c^0 = 1$ (K_2SO_4 as feed)	$c_{K_2SO_4,0}$ = 0.1 mol/l $c_{BaCl_2,0}$ = 0.1 mol/l V_f = 150 ml V_r = 150 ml Q_f = 35 ml/min ω = 300 min^{-1} T = 25 °C α = 0.96 γ = 0.15
Initial concentration $C_{i,0}$	$R_c^0 = 1$ ($BaCl_2$ as feed)	$c_{K_2SO_4,0}$ = 0.1..0.01 mol/l $c_{BaCl_2,0}$ = 0.1..0.01 mol/l V_f = 150 ml V_r = 150 ml Q_f = 35 ml/min ω = 300 min^{-1} T = 25 °C α = 0.96 γ = 0.15
Initial concentration ratio R_c^0	Set 1 R_c^0 = 1…0.05 ($BaCl_2$ as feed)	$c_{K_2SO_4,0}$ = 0.1 mol/l (fixed) $c_{BaCl_2,0}$ = 0.1 …0.005 mol/l V_f = 150 ml V_r = 150 ml Q_f = 35 ml/min ω = 300 min^{-1} T = 25 °C α = 0.96 γ = 0.15
	Set 2 R_c^0 = 1.33…20 ($BaCl_2$ as feed)	$c_{BaCl_2,0}$ = 0.1 mol/l (fixed) $c_{K_2SO_4,0}$ = 0.075…0.005 mol/l V_f = 150 ml V_r = 150 ml Q_f = 35 ml/min ω = 300 min^{-1} T = 25 °C α = 0.96 γ = 0.15

Stable transparent microemulsions were obtained throughout the reaction time. 20 min after the feeding was completed, samples were taken from the reaction mixture, and a small droplet of colloidal dispersion was put onto a carbon-covered grid placed on a filter paper.

As a sample carrier, copper grids with a diameter of 3.05 mm from the Plano Company were used. These copper grids were laminated with a carbon film. For the sample preparation, a small droplet (50 µl) of the sample solution was put onto a carbon film-covered copper grid placed on a filter paper. Cyclohexane and water were evaporated in air at ambient temperature and the surfactant was removed in a washing step with acetone-water solution (2:1) (a procedure suggested by [Schmidt, 2000].

For the observation of the nanoparticles, a transmission electron microscope TEM (CM200, Philips) equipped with a CCD camera (Keen view, SIS) was used. This device was working with high voltage of 200 kV producing De-Broglie wave length of 0.0025 nm. The resolution of the picture was 0.21 nm with a maximum magnification of 750000. A regular calibration was done by using spherical Latex particles and standardized grids. For statistical analysis, several pictures were taken from the grid and a sample of 200 particles was selected from different pictures. The particle size was then measured with AnalySis® from Soft Imaging Analysis GmbH. For the chemical analysis of the nanoparticles, an energy dispersive system DX4 from firma EDAX, Inc® was used.

Chapter 4

Experimental Results

4.1 Characterization of the microemulsion system

The aim of characterization of the microemulsion system in this study is to obtain important parameters for $BaSO_4$ nanoparticle precipitation where microemulsion is subsequently used as the reaction media. This characterization study includes investigations of the microemulsions phase behaviour, viscosity, and size of the water-in-oil (w/o) nano-droplets.

Lade et al. (2000) were the first to study the phase behaviour of ternary microemulsion consisting of water, cyclohexane, and non-ionic surfactants of Marlipal series. Nanoparticle precipitation in microemulsion systems requires a single-phase w/o-microemulsion as reaction medium. Therefore, the investigations on the phase behaviour of the microemulsion system were focused on the oil-rich region of the phase diagram where an isotropic and thermodynamically stable droplet dispersion of water in cyclohexane exists. This single-phase microemulsion appears to be an optically clear liquid of low viscosity, low electric conductivity, and low surface tension [Sottmann and Strey, 1997]. For practical reason, the phase behaviour is depicted in a quasi-binary diagram i.e. at constant surfactant content (see Fig. 4.1).

4.1.1 Influence of surfactant ethoxylation degree

The technical non-ionic surfactants used in this work are iso-alkyl polyglycol ether types (C_iE_j), denoted as Marlipal. These surfactant types are typically synthesized by the reaction of ethylene oxide with an alcohol (e.g. isotridecanol). Through this kind of reaction, surfactant molecules with different of ethoxylation (E_j) degrees can be obtained.

Fig. 4.1 shows the single-phase microemulsion region (marked as 1φ), as a channel from $\alpha = 0.85$ to $\alpha = 0.96$, as a function of temperature T for three different ethoxylation degrees of the surfactant Marlipal. The single-phase region (1φ) is bounded by a lower and an upper temperature boundary. At temperatures above the upper temperature boundary the mixtures become turbid, followed by the separation into two phases of a water-in-oil microemulsion in equilibrium with an excess water phase (2φ). At temperatures below the

lower temperature boundary, the phase separation into oil-in-water microemulsion is in equilibrium with an excess of oil (2φ') [Lade et al., 2000].

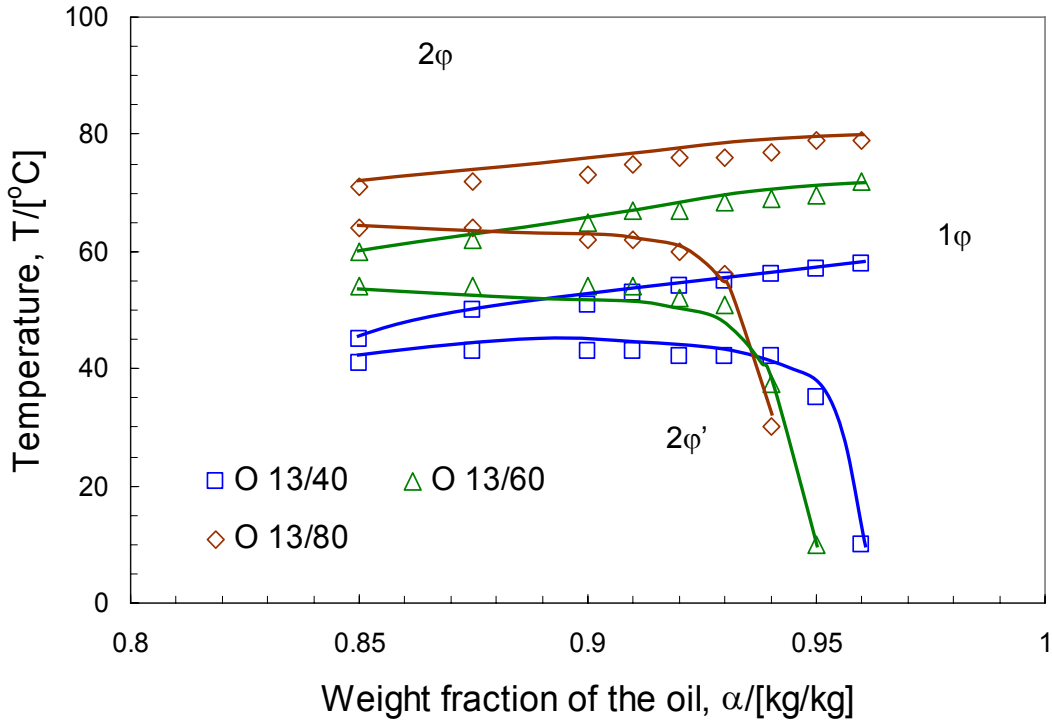

Fig. 4.1: Oil-rich part of the phase prism for different Marlipal surfactant degrees of ethoxylation (O) at surfactant weight fraction $\gamma = 0.15$.

When the Marlipal ethoxylation degree is high (see Fig. 4.1), the single-phase microemulsion region shifts towards higher temperatures. Schubert and Kaler (1996) found that the increase of the number of ethoxy-groups (E_j) made surfactants more hydrophilic, thereby more water soluble but less efficient. The surfactant efficiency is defined as the ability of the surfactant to solubilise equal amounts of water and cyclohexane (oil) [Sottman et al., 2002].

Compared to surfactants with higher ethoxylation degrees (Marlipal O 13/60 and Marlipal O 13/80), a microemulsion containing Marlipal O 13/40 shows a single phase behaviour at lowest temperatures. Therefore, with regard to technical applications, Marlipal O 13/40 is chosen as the surfactant to prepare microemulsions as reaction medium for $BaSO_4$ nanoparticle precipitation in this work.

There is a significant difference (approx. 10 °C higher) between the single-phase microemulsion region identified in this work and the literature data reported by Lade et al.

(2000). This difference could be explained by the fact that Marlipal is a technical grade surfactant being produced in large quantities. Therefore, the distribution of the ethoxylation degree, which is obtained in an industrial production process, can not be accurately controlled. These observations show that the temperature window of the single-phase microemulsion region could be adjusted by the ethoxylation degree of the surfactant.

4.1.2 Influence of surfactant weight fraction

Another important factor that determines the existence of the single-phase microemulsion region is the quantity of the used surfactant. Fig. 4.2 shows experimentally determined the single-phase (1φ) microemulsion existence region from $\alpha = 0.84$ to $\alpha = 0.96$, at different surfactant weight fractions γ. The lower temperature boundary shifts towards lower values and water-rich regions, when the surfactant content is increased. The upper temperature boundary remains almost unchanged. At the highest surfactant concentration ($\gamma = 0.3$), the lower boundary in this case could not be observed due to high surfactant solubilization. At lower concentration of the surfactant, less oil and water can be solubilized [Schubert and Kaler, 1996]. Therefore, with a decreasing surfactant concentration at equal oil weight fraction α and temperature, the single-phase microemulsion turns into a two-phase mixture.

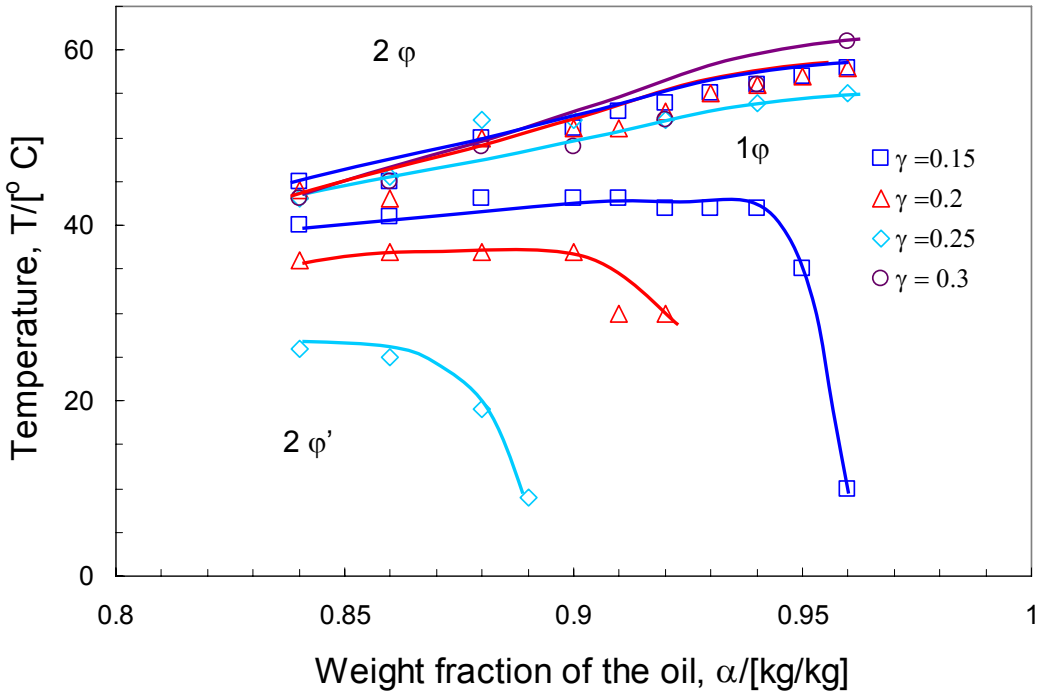

Fig. 4.2: Oil-rich part of the phase prism for different surfactant weight fractions γ (Marlipal O 13/40).

4.1.3 Influence of reactant concentrations

The influence of the ionic reactants on the existence and location of the single-phase microemulsion state was also investigated as an extension work published by Lade et al., (2000). The information derived from this investigation is important in order to fix suitable operating conditions for the precipitation reaction to be carried out in the microemulsion system. Reactants which are filled in nanodroplets may lead to a reactant-surfactant interaction, which may have an impact on the phase behaviour. Furthermore, the information about the amount of reactants which can be dissolved in the single-phase microemulsion without any change of the phase state can be used for adjustments of the range of the supersaturation level inside the water droplet.

Fig. 4.3 and Fig. 4.4 show the effect of dissolved $BaCl_2$ and K_2SO_4 as reactants on the phase behaviour of the microemulsion by variation of the molar salt concentration in the aqueous phase. The reactant free microemulsion is also depicted in these figures for the purpose of comparison.

When $BaCl_2$ salt is dissolved in the Marlipal O 13/40 microemulsion, there is a slight deviation of the upper and lower temperature boundary towards the lower temperatures. Fig. 4.3 illustrates this observation.

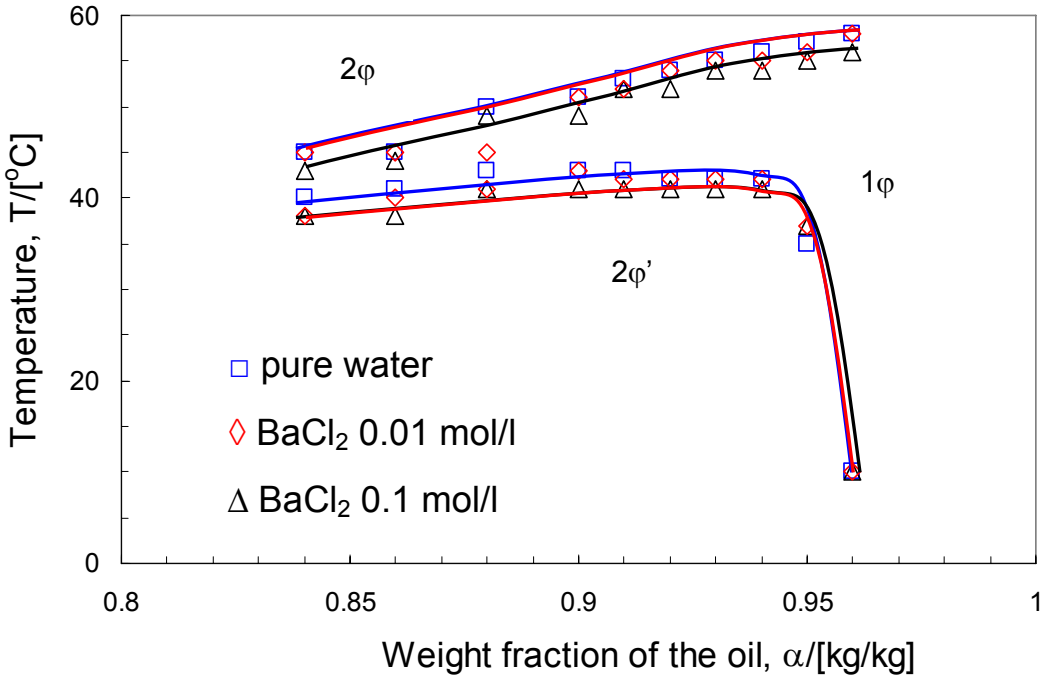

Fig. 4.3: Oil-rich part of the phase prism for 0.01 mol/l $BaCl_2$ and 0.1 mol/l $BaCl_2$ at a surfactant weight fraction $\gamma = 0.15$ (Marlipal O 13/40).

Particularly, when K_2SO_4 is dissolved in water droplets, there is a very pronounced shift of the single-phase region compared to the reactant-free microemulsion (see Fig. 4.4). Similar results for quaternary microemulsion systems were reported for non-ionic surfactant microemulsions with different reactants: Na_2CO_3 and $CaCl_2$ [Rauscher et al., 2005], NaCl [Schubert and Kaler, 1996], NaCl and $Ca(OH)_2$ [Nanni and Dei, 2003], and $(NH_4)_2SO_4$ and $Ba(OAc)_2$ [Qi et al.,1996].

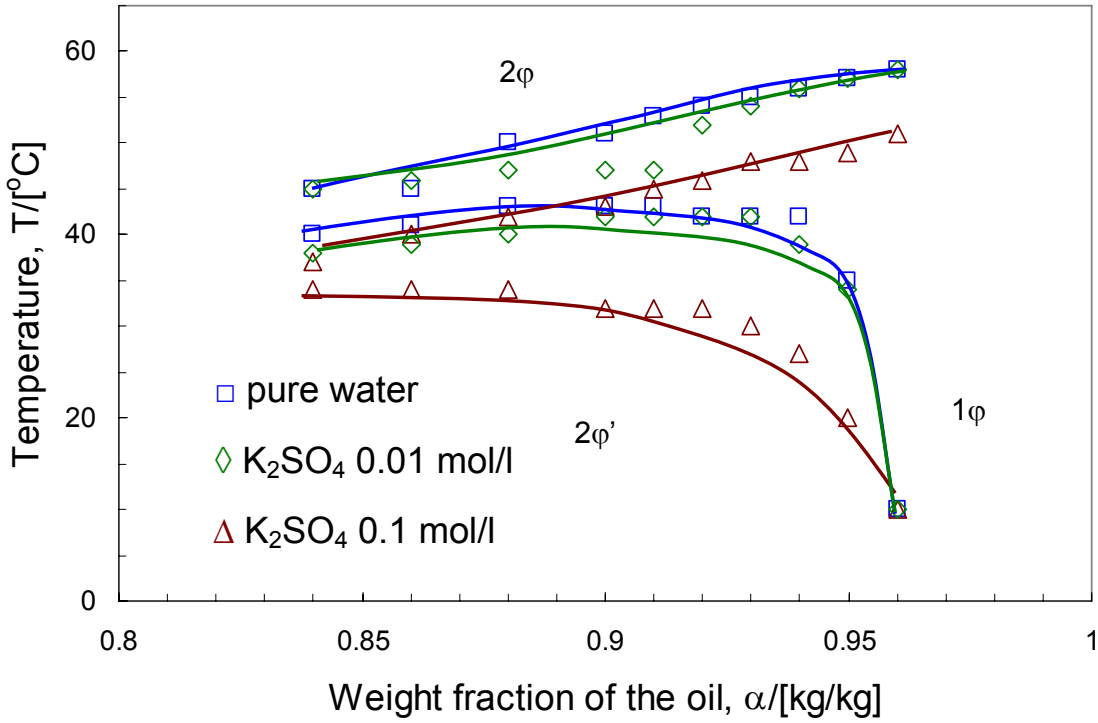

Fig. 4.4: Oil-rich part of the phase prism for 0.01 mol/l K_2SO_4 and 0.1 mol/l K_2SO_4 at a surfactant weight fraction $\gamma = 0.15$ (Marlipal O 13/40).

As shown in Fig. 4.5 and Fig. 4.6, microemulsions containing K_2SO_4 at a surfactant weight fraction of $\gamma = 0.2$ demonstrate the same manner compared to microemulsions at $\gamma = 0.15$. The apparently different effect of the two investigated salts on the single-phase microemulsion region can be explained by the 'Hofmeister series' [Rauscher et al., 2005]. The mutual solubility between water and non-ionic surfactants is decreased by the dissolved anions in the following order: $SO_4^{2-}>PO_4^{3-}>CO_3^{2-}>Cl^->Br^-$. These anions can be regarded as water structure builders and perform as salting out agents for the surfactant molecules. Due to this, the SO_4^{2-} ion will have more influence to decrease the mutual solubility between water and the non-ionic surfactant compared to the Cl^- ion. This causes a more pronounced shift of

the single-phase microemulsion towards lower temperatures for microemulsions with the dissolved K_2SO_4.

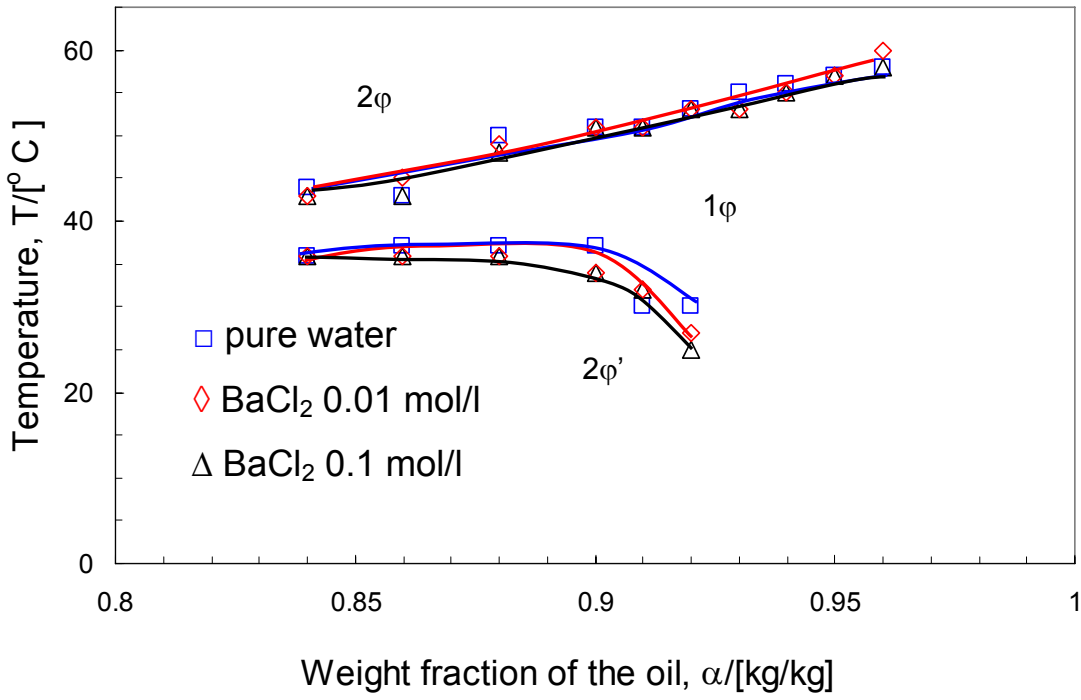

Fig. 4.5: Oil-rich part of the phase prism for 0.01 mol/l $BaCl_2$ and 0.1 mol/l $BaCl_2$ at a surfactant weight fraction $\gamma = 0.20$ (Marlipal O 13/40).

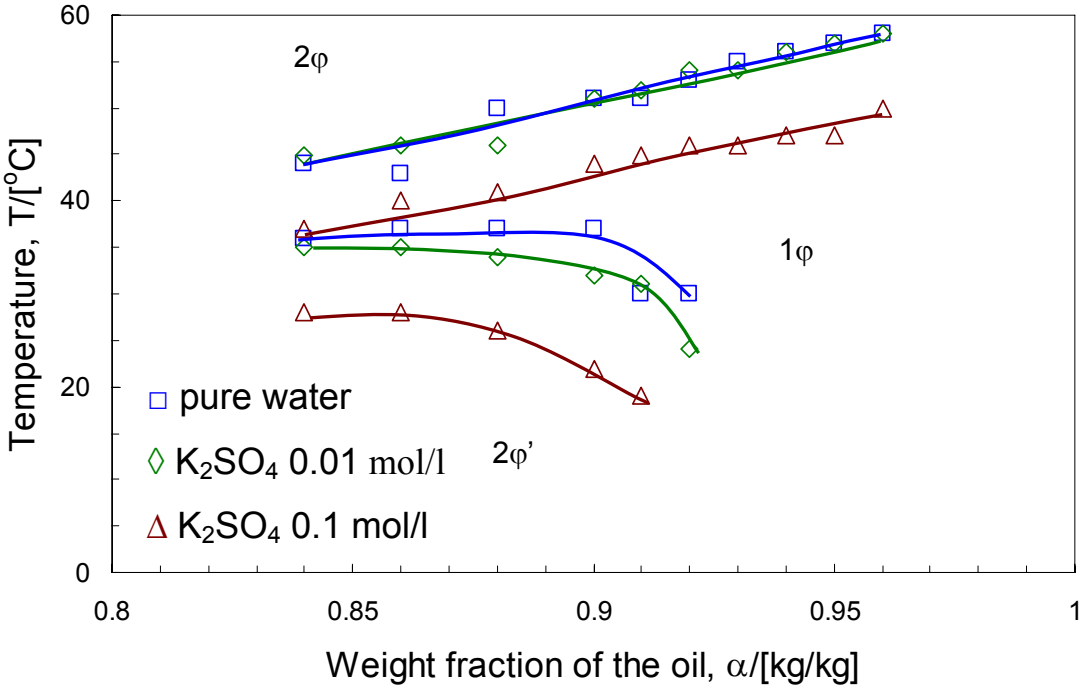

Fig. 4.6: Oil-rich part of the phase prism for 0.01 mol/l K_2SO_4 and 0.1 mol/l K_2SO_4 at a surfactant weight fraction $\gamma = 0.20$ (Marlipal O 13/40).

4.1.4 Determination of the operating region for microemulsion precipitation

Fig. 4.7 illustrates the intersection of the microemulsion existence regions being already shown in Fig. 4.3 and Fig. 4.4. Thereby, a suitable operating region to carry out the $BaSO_4$ nanoparticle precipitation is defined. It can be seen that different effects of reactants lead to a decrease of the available region for carrying out the precipitation reaction at microemulsion condition. Particularly at higher reactant concentrations the intersection area of the two single-phase regions where both microemulsions exist at the same temperature and composition shrinks considerably. In this work, the operating point for nanoparticle precipitation experiments in microemulsion was selected based on practical operating aspects: ambient temperature T = 25 ^oC, oil weight fraction $\alpha = 0.96$, and surfactant weight fraction $\gamma = 0.15$ (orange point in Fig. 4.7). The selected composition at $\alpha = 0.96$ is based on the idea that the highest possible amount of active water phase should be achieved at the selected operating temperature of 25 ^oC. At weight fractions lower than $\alpha = 0.96$, the single-phase microemulsion starts to separate into two phases.

4.1.5 Droplet size measurements

Dynamic light scattering (DLS) was used to determine the diameter of the water droplets in the single-phase microemulsion. The droplet size measurements were performed at the same operating conditions as being selected for the precipitation experiments (T = 25 ^oC, $\alpha = 0.96$, $\gamma = 0.15$). Measurements were carried out at various compositions (Table 4.1) in order to study the effect of dissolved reactants on the size of droplets.

Table 4.1 Mean droplet diameter.

	Pure water	**0.1 mol/l $BaCl_2$**	**0.01 mol/l $BaCl_2$**	**0.1 mol/l K_2SO_4**	**0.01 mol/l K_2SO_4**
Mean droplet diameter, d_{drop} [nm]	5 ± 1	5 ± 1	5 ± 1	5 ± 1	5± 1

At these conditions, the droplet size remained nearly the same (d_{drop} ~ 5nm) at all salt concentrations being analysed. Detailed investigations on various compositions and temperatures were performed by Rauscher et al. (2005) and Lade et al. (2000) using the same microemulsion system. Qualitatively, their results show that higher temperatures of the

microemulsion system lead to bigger droplet sizes at the same emulsion composition. An increase of the water content also causes a swelling of the droplets in the microemulsion.

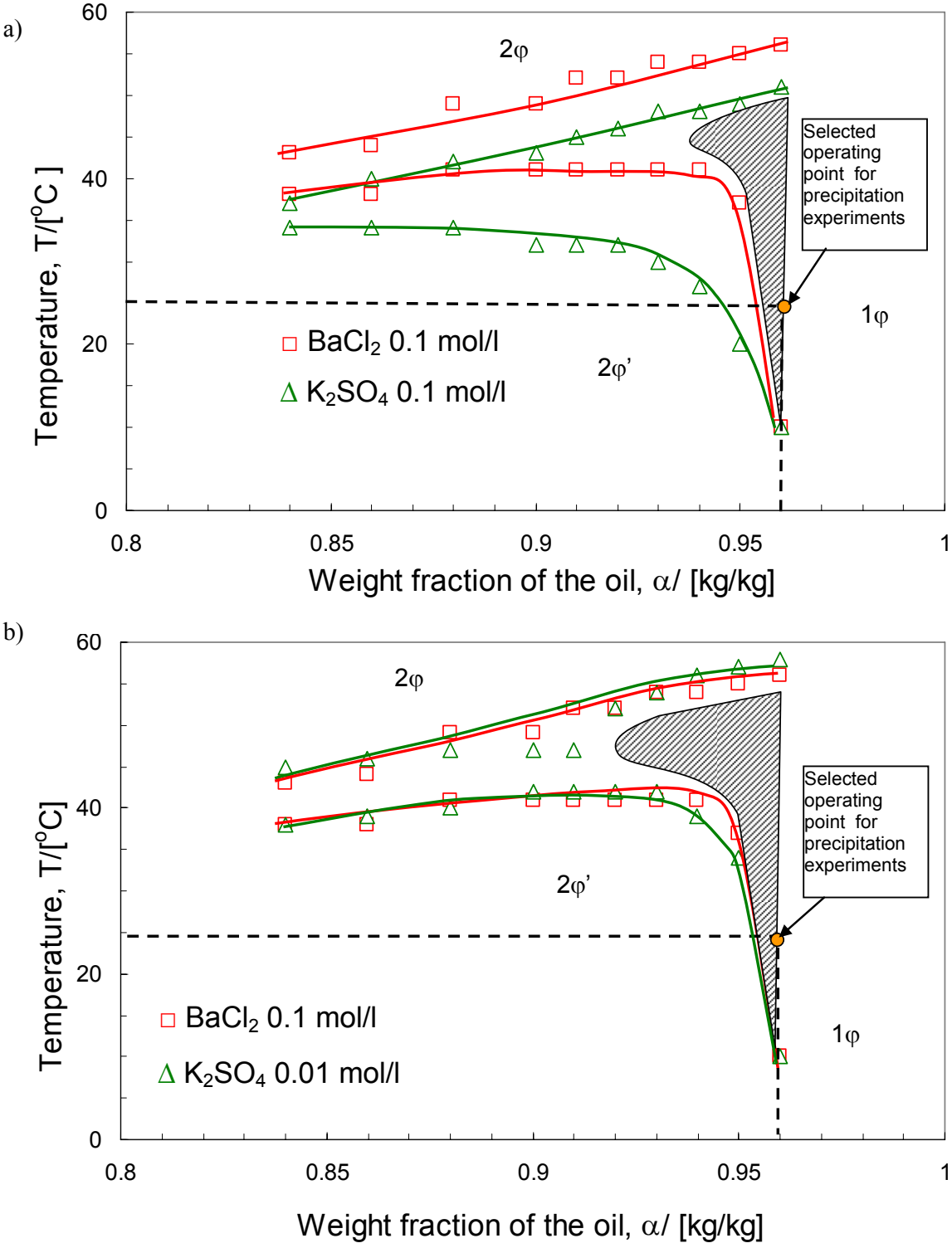

Fig.4.7: a) Oil-rich part of the phase prism for 0.1 mol/l $BaCl_2$ and 0.1 mol/l K_2SO_4 at surfactant weight fraction $\gamma = 0.15$. b) Oil-rich part of the phase prism for 0.1 mol/l $BaCl_2$ and 0.01 mol/l K_2SO_4 at surfactant weight fraction $\gamma = 0.15$ (Marlipal O 13/40).

4.1.6 Viscosity measurements

Single-phase microemulsion systems are usually considered as systems with a very low interfacial tension and viscosity [Sottmann and Strey, 1997]. Higher relative viscosity η_r values generally indicate qualitative structural changes of the microemulsion. These are normally observed within the narrow channel of the single-phase microemulsion in the phase diagram when approaching the lower temperature boundary or at higher water contents. In Fig. 4.8 the relative viscosity η_r is depicted as a function of temperature for the microemulsion under investigation.

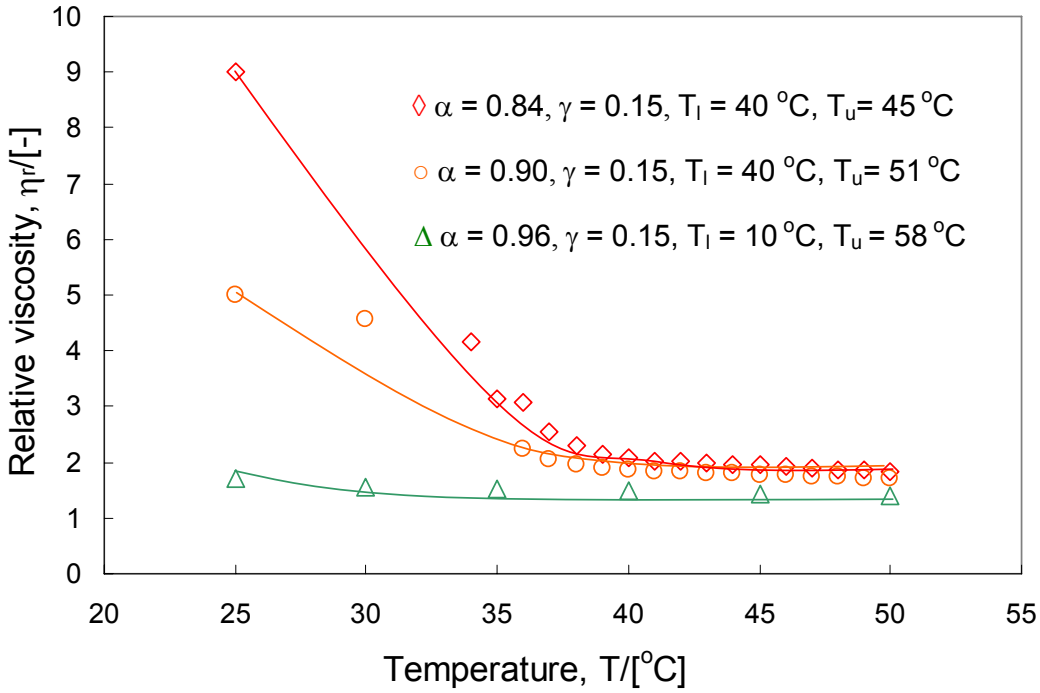

Fig. 4.8: Relative viscosity η_r versus temperature for the system water-cyclohexane-Marlipal O 13/40.

For three given compositions (α = 0.84, 0.90, 0.96), the relative viscosity increases when the temperature decreases. A significant increase of the viscosity is observed at the lowest oil weight fraction α. These changes of the relative viscosity qualitatively indicate a stronger droplet interaction or a higher degree of structural transformation particularly, when the ternary mixture is already in a phase state below the single-phase microemulsion region (curves at α = 0.84 and 0.90). On the contrary, towards temperatures (above the upper temperature boundary), no significant changes of the relative viscosity are detectable. In Fig. 4.8, it is shown that the chosen operating composition of the microemulsion (α = 0.96 and γ =

0.15) has the lowest viscosity compared to other compositions and does not show significant structural changes on temperature disturbances.

A higher concentration of the surfactant results in the higher relative viscosity (see Fig. 4.9). The reason is that the liquid non-ionic surfactant Marlipal being used has the highest viscosity among all components of the ternary mixture.

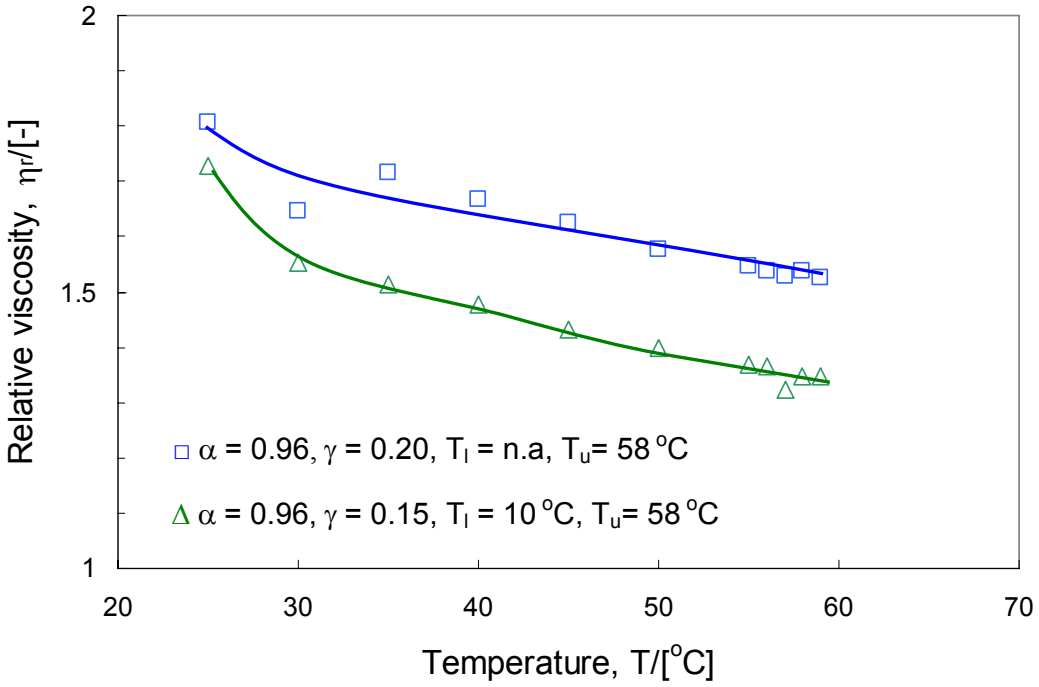

Fig. 4.9: Relative viscosity η_r versus temperature for the system water-cyclohexane-Marlipal O 13/40.

4.2 Bulk phase precipitation

Bulk $BaSO_4$ precipitation experiments had been studied by several researchers e.g. [Aoun et al., 1996, Balydiga et al., 1995 and Fitchett and Tarbell, 1990]. These studies, which were performed at various scales, revealed the key geometrical and operating parameters that play the major role in this process. Several investigations on mixing effects (e.g stirring rate ω, feed position in the reactor) led to conflicting results and interpretation. Most of these studies were carried out under stoichiometric conditions but only a little attention was paid to non-stoichiometric feed conditions, which inevitably occur during the semi-batch mixing of the two reactant solutions [Wong et al., 2001].

In this study, the bulk precipitation of $BaSO_4$ is considered as reference process for the purpose of comparison to the precipitation in the microemulsion system. Wong et al. (2001)

performed the precipitation of $BaSO_4$ in a 10 l tank, Na_2SO_4 and $BaCl_2$ as reactants, 4 baffles and a lower initial supersaturation ratio S_i compared to the 3 l tank, K_2SO_4 and $BaCl_2$ as reactants, and 18 baffles as used in the present work. In this study initial supersaturations S_i between 2200-5000 were applied (Table 4.2) as compared to 600-2500 in Wong's experiments.

Table 4.2 Experimental conditions chosen for $BaSO_4$ bulk precipitation.

K_2SO_4 Feed	**$C_{K_2SO_{4,0}}$ [mol/l]**	**$C_{BaCl_{2,0}}$ [mol/l]**	**Initial molar ratio, R_N^0**	**Initial supersaturation, S_i**
V_r = 700 ml	0.1	0.021	1	2184
V_f = 150 ml	0.1	0.042	2	3089
	0.1	0.107	5	4931
$BaCl_2$ Feed	**$C_{BaCl_{2,0}}$ [mol/l]**	**$C_{K_2SO_{4,0}}$ [mol/l]**	**Initial molar ratio, R_N^0**	**Initial supersaturation, S_i**
V_r = 700 ml	0.1	0.021	1	2184
V_f = 150 ml	0.1	0.042	0.5	3089
	0.1	0.107	0.2	4931

Three main parameters were studied in this particular $BaSO_4$ bulk-phase precipitation. In the first set of experiments, the effects of the initial molar ratio R_N^0 and of the stirring rate ω on the particle size distribution were investigated, while in the second part the effect of the feeding rate Q_f was analysed. In addition to these parameters, $BaCl_2$ and K_2SO_4 were applied as feed component alternatively.

4.2.1 Effect of initial molar ratio and stirring rate on the particle size

Fig. 4.10a ($BaCl_2$ as feed) and 4.10b (K_2SO_4 as feed) show the effect of the initial molar reactant ratio R_N^0 and the stirring rate ω on the final mean particle diameter for the two different feeds. For stoichiometric feeding (R_N^0 = 1), the biggest particle sizes and broadest distributions were achieved (see Fig. 4.11). This phenomenon can be explained by the fact that at initial molar ratios close to the stoichiometric value (R_N^0 = 1), a lower initial supersaturation S_i will be obtained (see Table 4.2). This lower initial supersaturation will

create fewer nuclei, which leads to a bigger particle size. On the contrary at non-stoichiometric conditions ($R_N^0 = 2$, 5 or 0.5, 0.2) a higher initial supersaturation ratios is realized which leads to bigger number of nuclei, resulting in smaller particles.

Overall, the stirring speed ω does not influence significantly the mean particle diameter d_{pm} but there is a slight tendency that at higher stirring rates ω, the mean particle diameter is smaller due to breakage of agglomerates.

The example of the final particle size distribution of different molar ratios ($BaCl_2$ feed) is shown in Fig. 4.11 below.

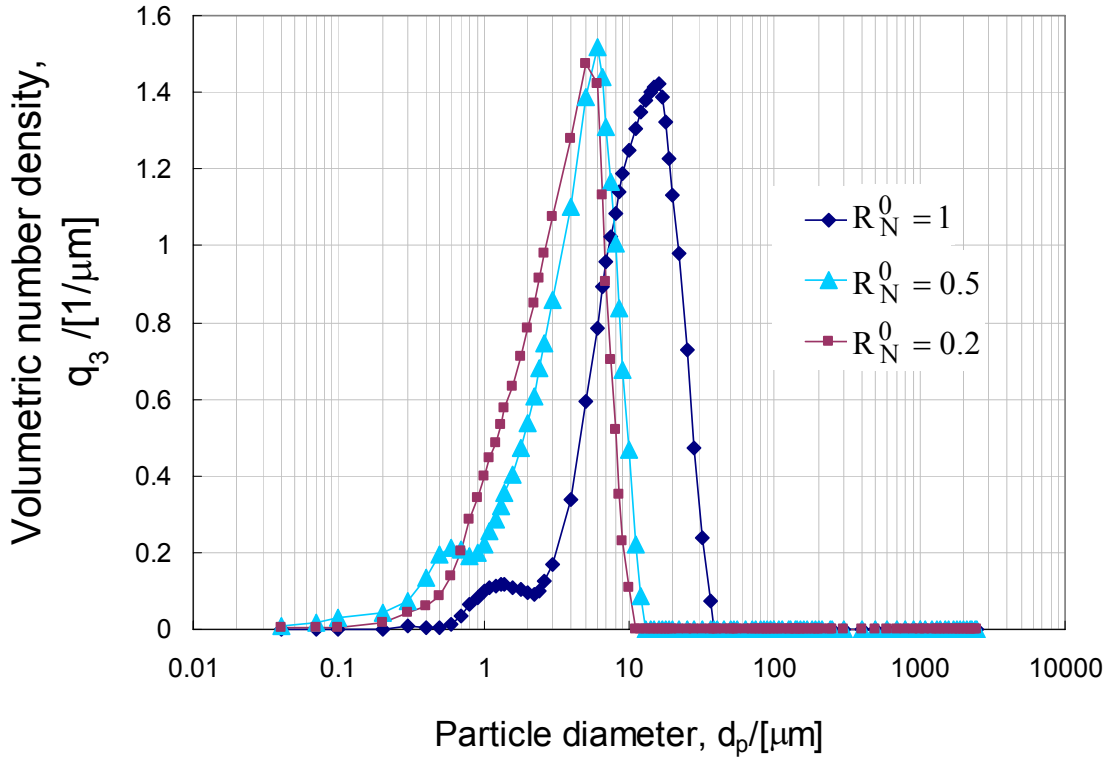

Fig. 4.11: Final particle size distribution as a function of the initial molar ratio R_N^0 at the stirring rate ω = 100 $min^{-1}$and the feeding rate Q_f = 34 ml/min ($BaCl_2$ feeding).

The particle size distributions of samples taken at different time intervals are shown in Fig. 4.12 (with $BaCl_2$ feed and at different stirring rates ω). There is a shift of the particle size distribution during 4.5 minutes of the feeding period towards larger particle size (see Fig. 4.12). After the feeding has been completed, there was no further particle growth observed as can be seen from the overlapping of the particle size distributions at 5, 10 and 15 minutes (the last samples taken).

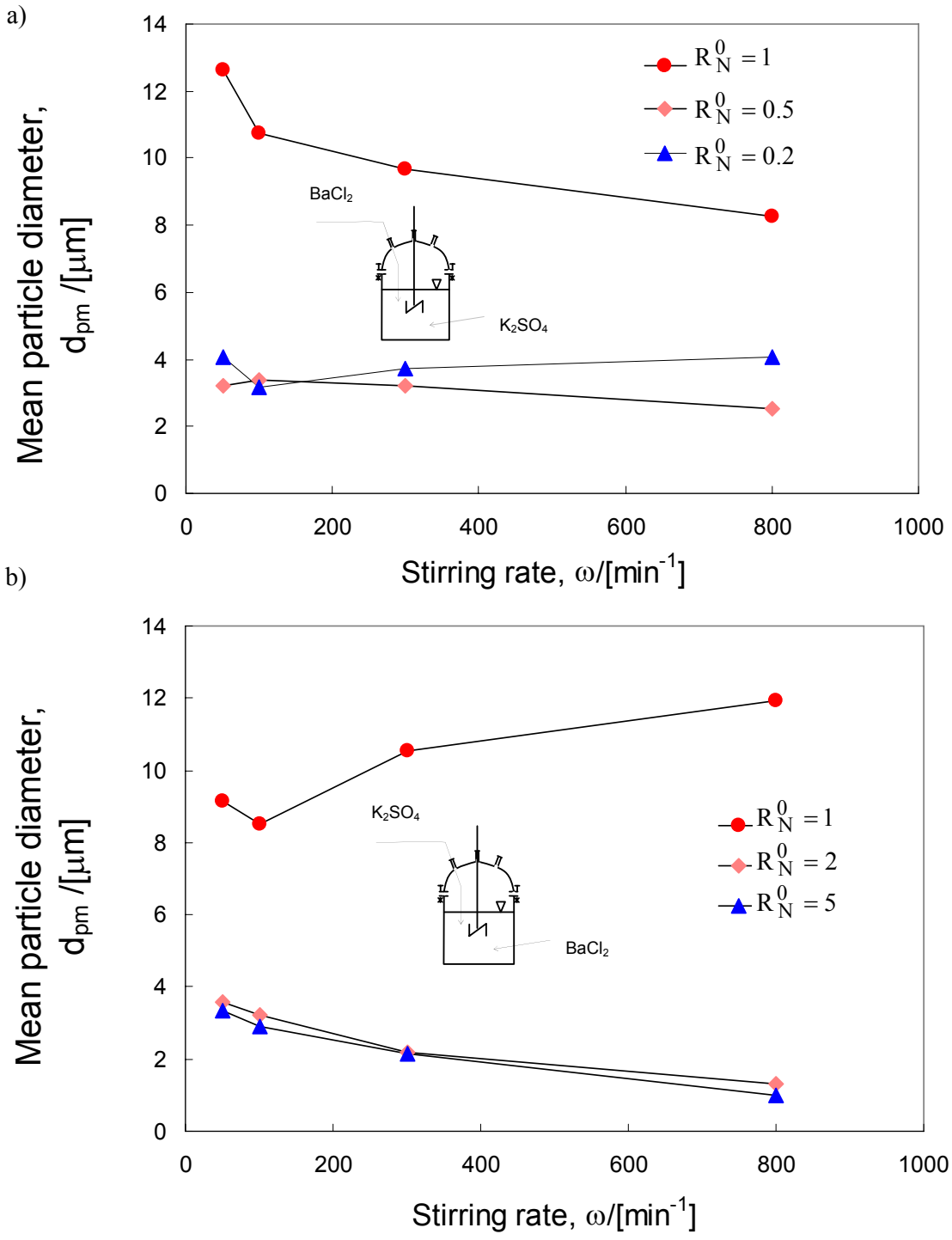

Fig. 4.10: a) Effect of the initial molar ratio R_N^0 and the stirring rate ω on the final mean particle diameter d_{pm} with the feeding rate Q_f = 34 ml/min ($BaCl_2$ feed). b) Effect of the initial molar ratio R_N^0 and the stirring rate ω on the final mean particle diameter d_{pm} with the feeding rate Q_f = 34 ml/min (K_2SO_4 feed).

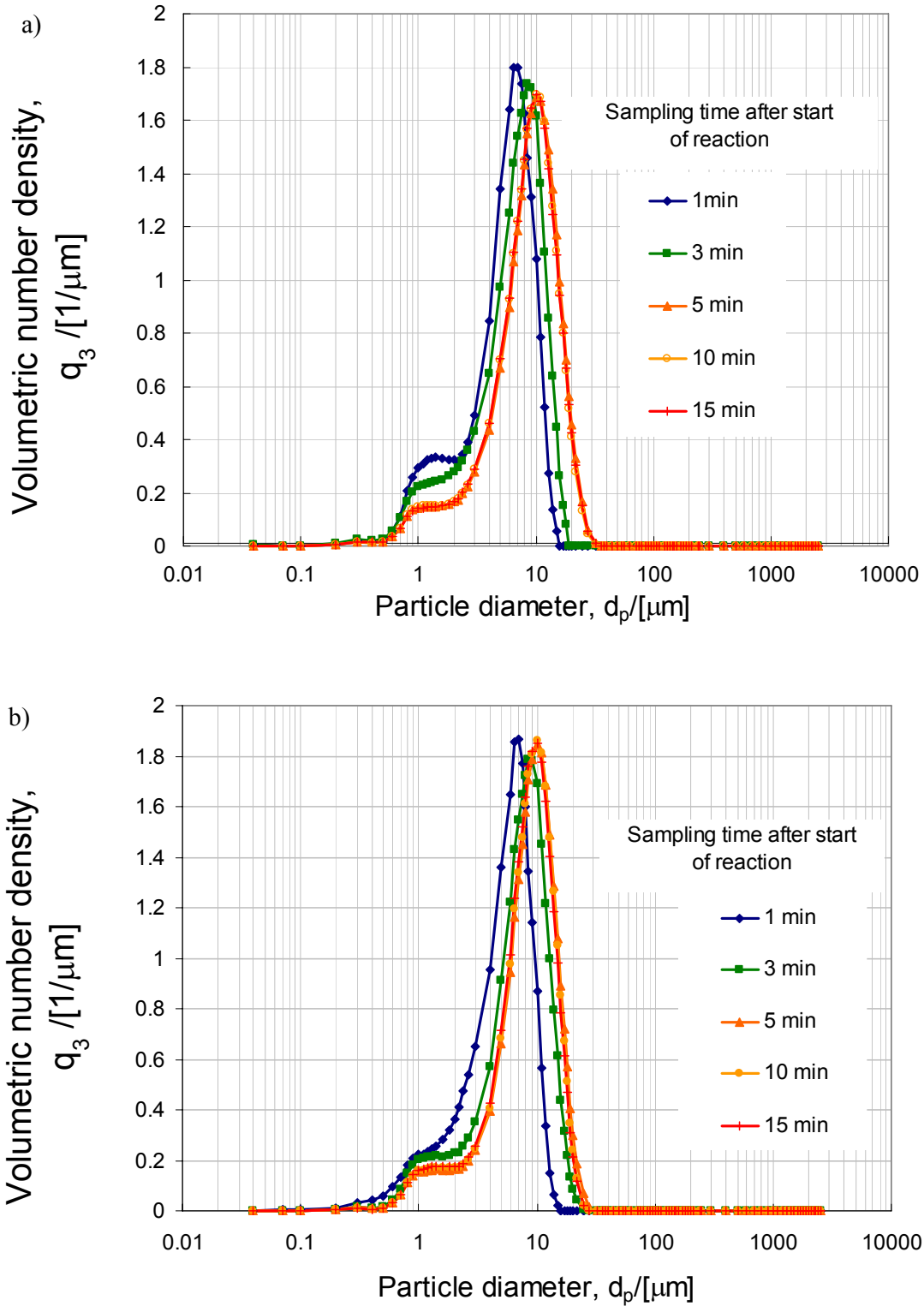

Fig. 4.12: a) Particle size distribution at the initial molar ratio R_N^0 = 1, the stirring rate ω = 300 min^{-1}, and the feeding rate Q_f = 34ml/min ($BaCl_2$ feeding). b) Particle size distribution at the initial molar ratio R_N^0 = 1, the stirring rate ω = 800 min^{-1}, and the feeding rate Q_f = 34ml/min ($BaCl_2$ feeding).

4.2.2 Effect of feeding rate on particle size

Fig. 4.13 shows the effect of the feeding rate Q_f in $BaSO_4$ bulk precipitation on the mean particle diameter at stoichiometric condition ($R_N^0 = 1$) and constant stirring rate. The Q_f-values were varied from 17.5 to 130 ml/min. It is observed that various feeding rates Q_f do not lead to a significant change of the particle size. The feeding rate used in the experiment is not slow enough to influence the particle size. As the typical nucleation time constant has the smallest value compared to other processes such as growth and mixing time constants, a significant slower feeding rate might lead to a situation where there are fewer nuclei formed spontaneously, and much of the feed material will be consumed by the growth process [Rauscher et al., 2005]. Eventually, this condition might lead to the generation of bigger particles.

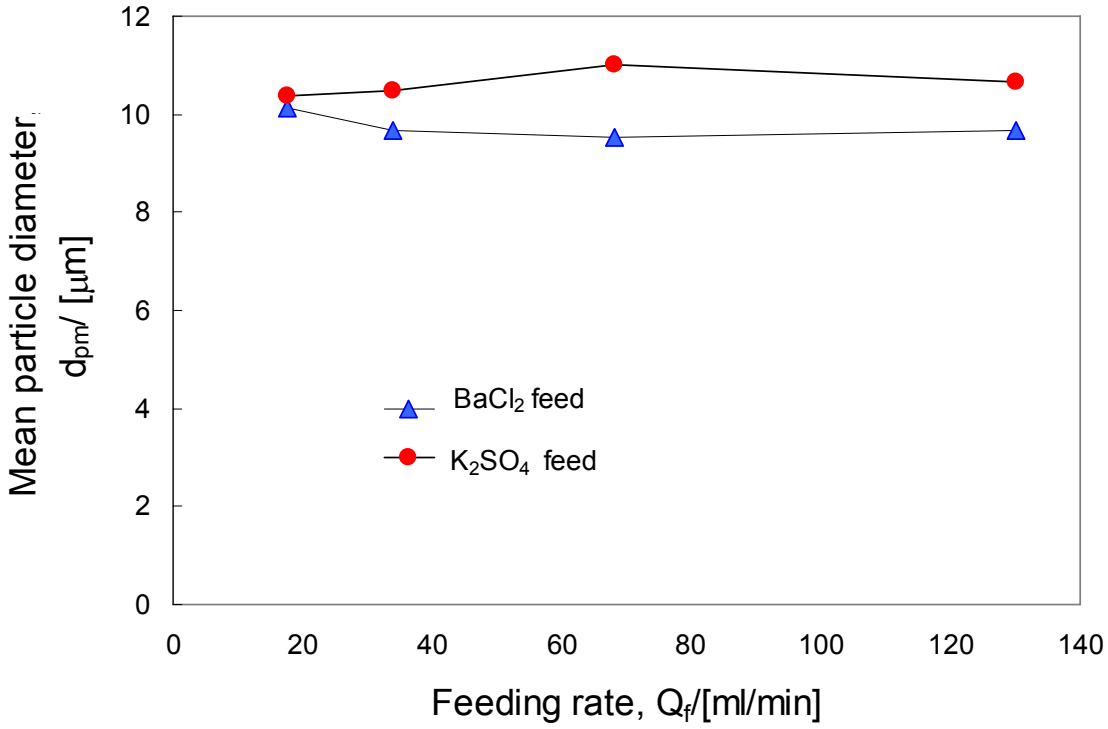

Fig. 4.13: Effect of the feeding rate Q_f on the final mean particle diameter d_{pm} with two feeding modes ($BaCl_2$ feed and K_2SO_4 feed), the initial molar ratio $R_N^0 = 1$, and the stirring rate $\omega = 300\ min^{-1}$.

Particle size distributions at different time intervals were determined to study the effect of the feeding rate Q_f (for $BaCl_2$ feed) and (K_2SO_4 feed) as depicted in Fig. 4.14 and Fig. 4.15. Due to slow feeding rate, it can still be seen the evolution of the particle size distribution due to growth during the feeding time especially for the slowest feeding rate $Q_f = 17.5$ ml/min.

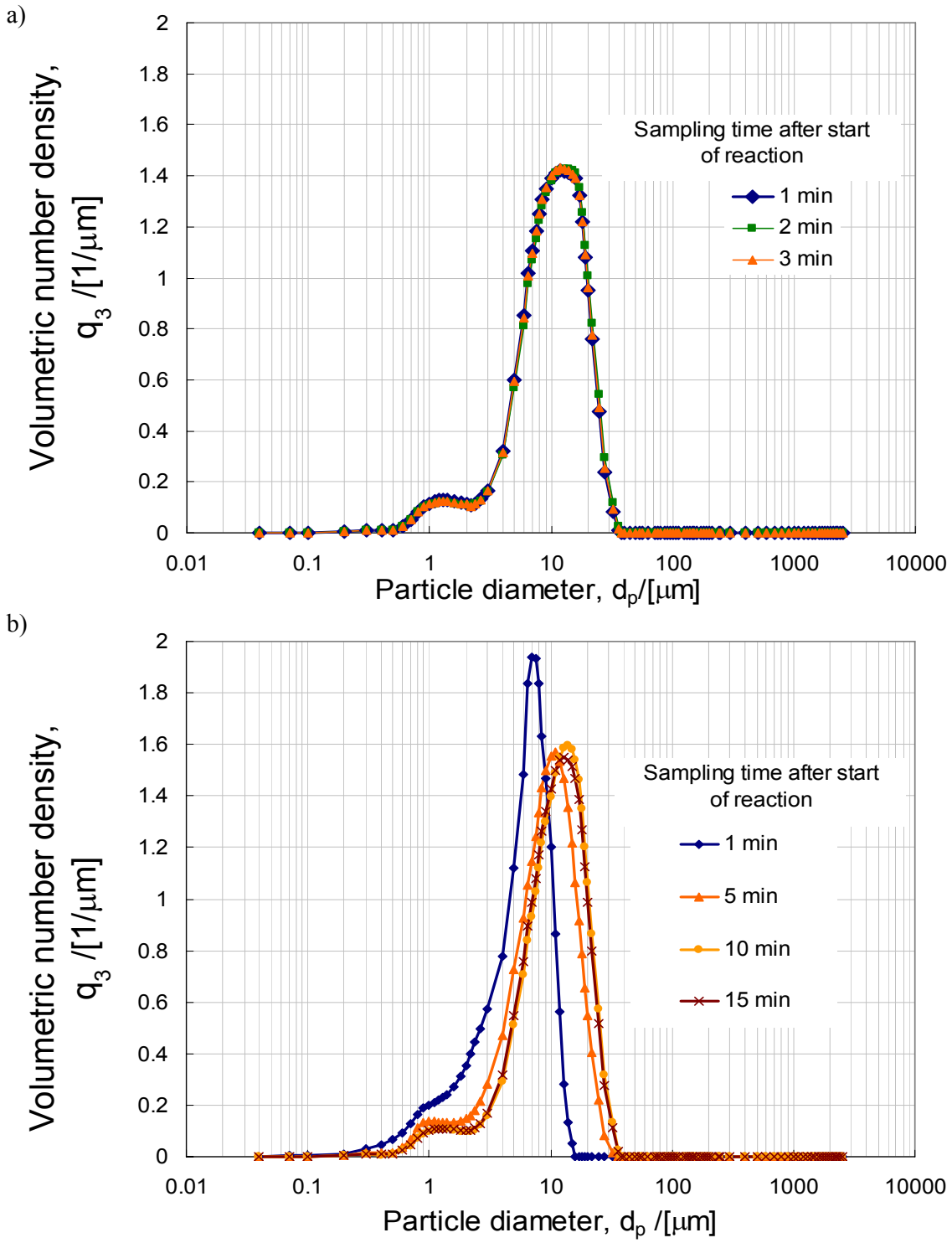

Fig. 4.14: a) Particle size distribution at the feeding rate Q_f = 130 ml/min, the initial molar ratio R_N^0 = 1, and the stirring rate ω = 300 min^{-1} ($BaCl_2$ feeding). b) Particle size distributionat the feeding rate Q_f = 17.5 ml/min, the initial molar ratio R_N^0 = 1, and the stirring rate ω = 300 min^{-1}($BaCl_2$ feeding).

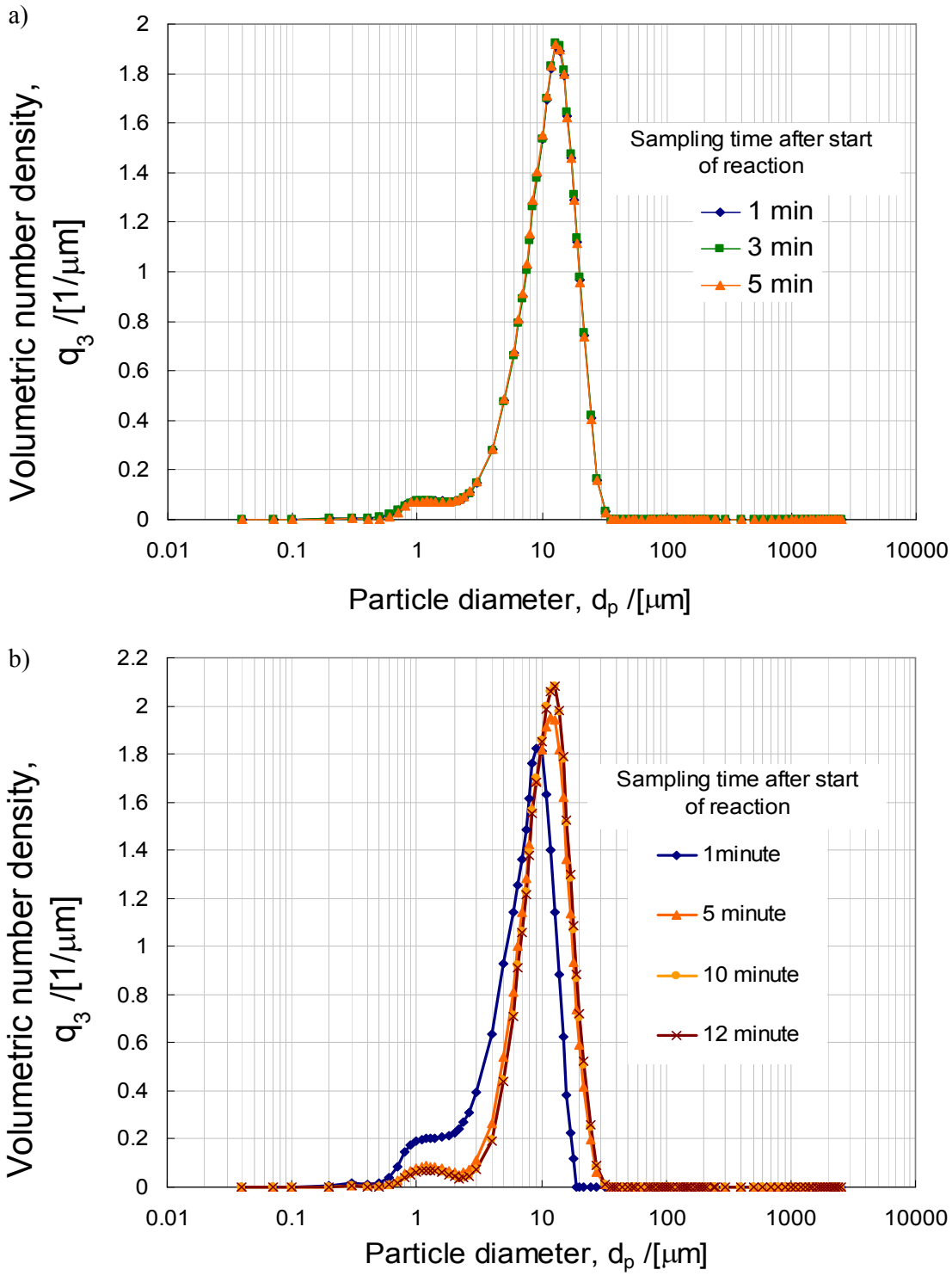

Fig. 4.15: a) Particle size distribution at the feeding rate Q_f = 130 ml/min, the initial molar ratio R_N^0 = 1, and the stirring rate ω = 300 min^{-1} (K_2SO_4 feeding) b) Particle size distribution at the feeding rate Q_f = 17.5 ml/min, the initial molar ratio R_N^0 = 1, and the stirring rate ω = 300 min^{-1} (K_2SO_4 feeding).

4.3 Precipitation of $BaSO_4$ nanoparticles in microemulsion

The feeding rate Q_f, the stirring rate ω, the feeding sequence, the absolute initial concentration level, and the initial concentration ratio R_c^0 were varied in order to investigate their influence on the particle size. The microemulsion composition as described in chapter 4.1.4 ($\alpha = 0.96$, $\gamma = 0.15$) was applied for precipitating $BaSO_4$ nanoparticles at T = 25 °C. A semi-batch mode as used in bulk precipitation was also applied with the same reactor configuration for microemulsion precipitation.

4.3.1 Stability and reproducibility

The size stability of the $BaSO_4$ nanoparticle produced in microemulsion precipitation over the time in this study is relatively high. Fig. 4.16 shows that the mean particle diameter of $BaSO_4$ nanoparticles d_{pm} does not change and shows no agglomeration even three months after the experiment.

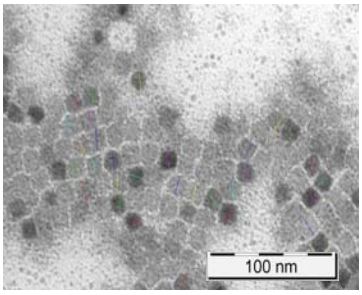

$d_{pm} = 16 \pm 3$ nm

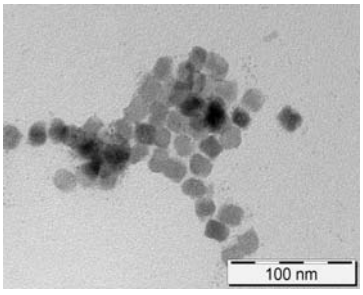

$d_{pm} = 16 \pm 3$ nm

Fig. 4.16: TEM images of $BaSO_4$ nanoparticles (left) fresh and 30 min after precipitation (right) 3 months without washing prepared at initial concentration ratio $R_c^0 = 10$. (Fixed conditions: $\alpha = 0.96$, $\gamma = 0.15$, T = 25 °C, $Q_f = 35$ ml/min, feeding sequence: $BaCl_2$ into K_2SO_4, and $\omega = 300$ min^{-1}).

An electron diffraction pattern of the generated cubic $BaSO_4$ nanoparticles (Fig. 4.17a right) reveals the crystalline structure. The energy dispersive X-ray analysis was also conducted and confirmed that the cubic particles were consisting of Ba, S, and O atoms, as illustrated in Fig. 4.17b.

a)

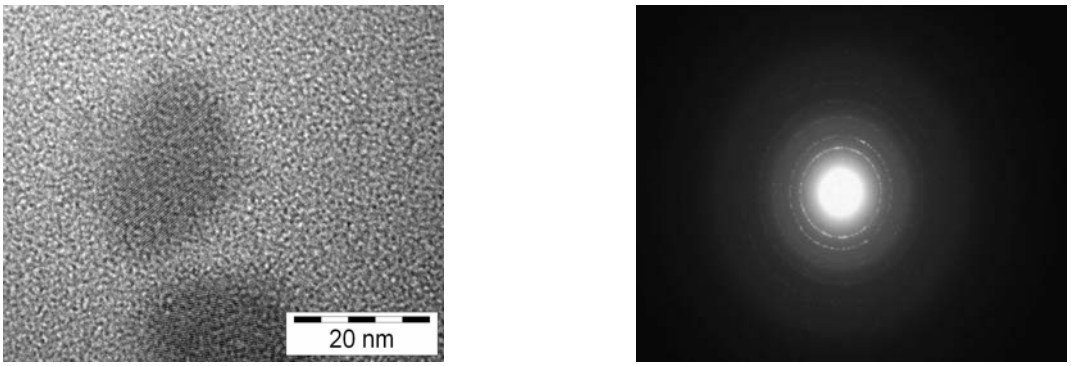

b)

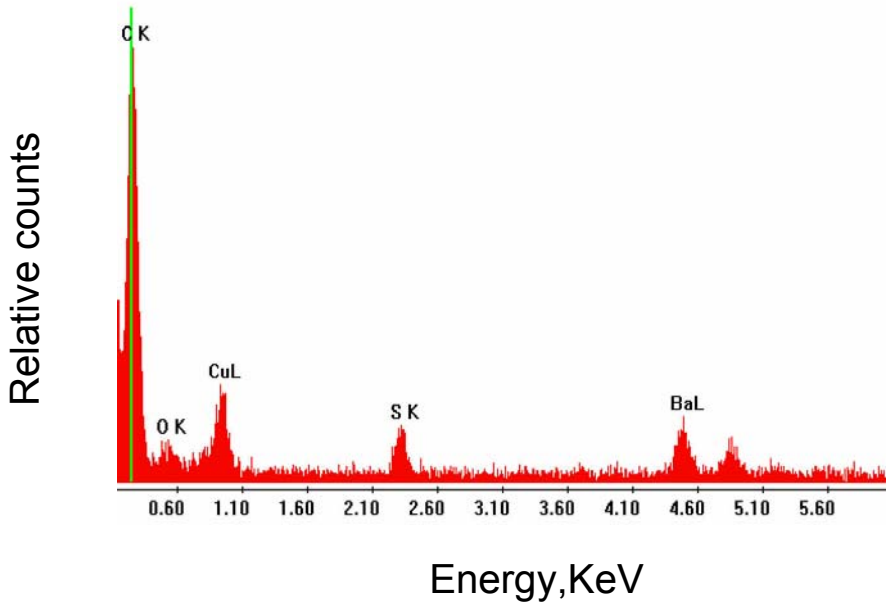

Fig. 4.17: a) HRTEM image of $BaSO_4$ nanoparticles at R_c^0 = 0.1 (left) and corresponding electron diffraction pattern (right). b) X-ray spectrum of cubic $BaSO_4$ nanoparticles (EDAX analysis).

The reproducibility of the experiment was checked by repeating experiments at several compositions twice. Fig. 4.18 depicts the result of the repetition experiment at R_c^0 = 10 and 0.1.

a)

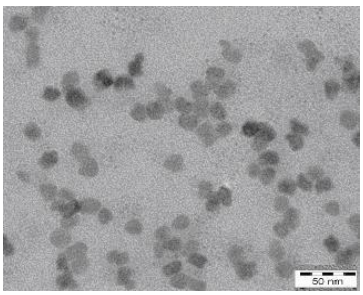

d_{pm} = 15 ± 2 nm

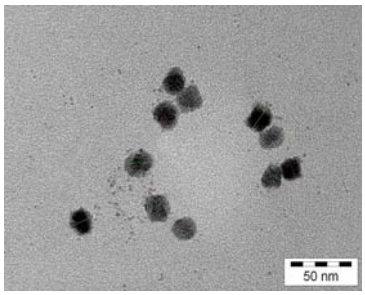

d_{pm} = 16 ± 3 nm

b)

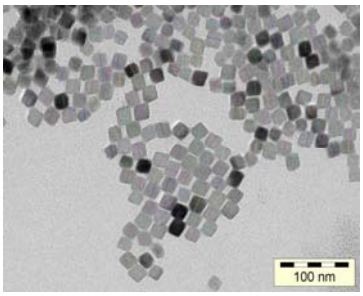

d_{pm} = 16 ± 2 nm

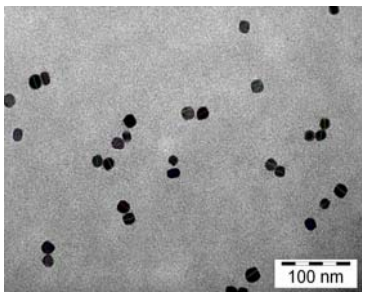

d_{pm} = 16 ± 2 nm

Fig. 4.18: a) TEM images of $BaSO_4$ nanoparticles: first experiment (left) and second experiment (right) performed with the initial concentration ratio R_c^0 = 10 (Fixed operating conditions: α = 0.96, γ = 0.15, T = 25 ^oC, Q_f = 35 ml/min, feeding sequence: $BaCl_2$ into K_2SO_4, and ω = 300 min^{-1}). b) TEM images of $BaSO_4$ nanoparticles: first experiment (left) and second experiment (right) performed with the initial concentration ratio R_c^0 = 0.1 (Fixed operating conditions: α = 0.96, γ = 0.15, T = 25 ^oC, Q_f = 35 ml/min, feeding sequence: $BaCl_2$ into K_2SO_4, and ω = 300 min^{-1}).

Fig. 4.18 shows that there is no significant difference of the mean particle diameter of two repeated experiments. In conclusion, the reproducibility of $BaSO_4$ nanoparticle precipitation in this work is qualitatively proved.

4.3.2 Feeding rate

In order to investigate the effect of the feeding rate Q_f on the mean particle diameter, precipitation experiments were carried out in a semi-batch mode with the initial reactant concentration of 0.1 mol/l for both reactants ($BaCl_2$ as feed and K_2SO_4 in the reactor) at a temperature of T = 25 ^oC with a constant surfactant weight fraction of $\gamma = 0.15$ and an oil weight fraction of $\alpha = 0.96$.

150 ml of the w/o-microemulsion containing K_2SO_4 were placed inside the reactor while the other 150 ml of the w/o-microemulsion containing the $BaCl_2$ were supplied at a specific feeding rate. When the feeding started, the reactor was stirred at 300 min^{-1}. Isotropic and clear reaction mixtures were always obtained during the feeding period.

Feeding rates Q_f were varied from 35, 70 up to 140 ml/min where a microemulsion with $BaCl_2$ as the feeding reactant was used. The increase of the feeding rate simultaneously decreases the feeding time from 257 s to about 65 s for the same volume of the feeding reactant. As shown in Fig. 4.19, the variation of feeding rates does not lead to a significant change of the particle size. We argue that the applied feeding rate parameters lie in a larger time scale than the time scale of the droplet fusion-fission exchange which is a prequisite for nanoparticle precipitation [Voigt et al., 2005].

Schmidt (2000) predicted a significant increase in the mean particle diameter of the palladium nanoparticles (up to 3 nm) by decreasing appreciably the feeding time (about 37.5 min (Q_f = 2.4 ml/min) compared with 4.5 min (Q_f = 35 ml/min) of this study). Initial supersaturation at a longer feeding time is much smaller than that at a faster feeding time. According to the classical nucleation theory, a lower supersaturation is leading to a smaller number of nuclei and a bigger particle size. Model simulations show a similar trend [Voigt et al., 2005] which is also confirmed by the experimental results in this work.

a)

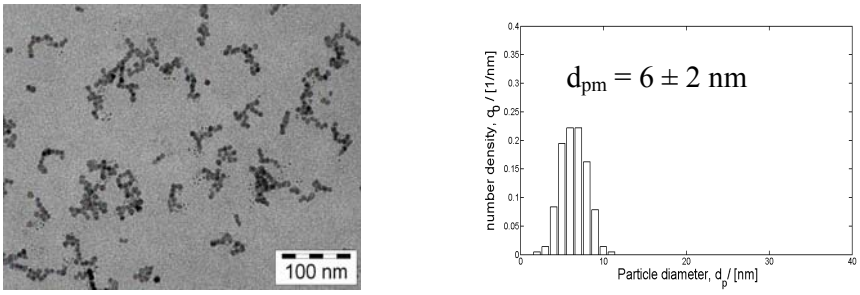

b)

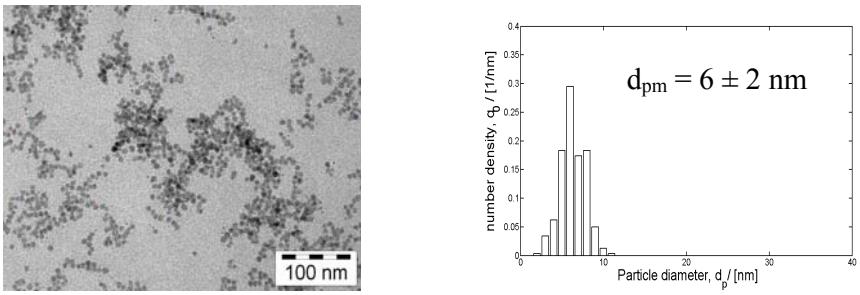

c)

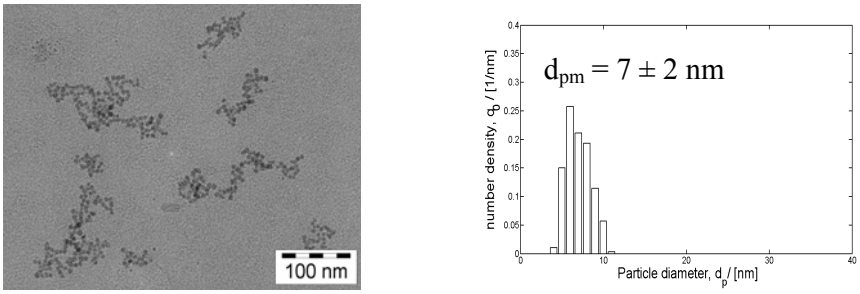

Fig. 4.19: TEM images of $BaSO_4$ nanoparticles (left) and the corresponding particle size distribution histogram (right) for different feeding rates: a) Q_f = 35 ml/min b) Q_f = 70 ml/min, c) Q_f = 140 ml/min (fixed operating conditions: α = 0.96, γ = 0.15, T = 25 °C, initial concentration ratio R_c^0 = 1, feeding sequence: 0.1 mol/l $BaCl_2$ into 0.1 mol/l K_2SO_4, ω = 300 min^{-1}).

4.3.3 Stirring rate

The effect of the stirring rate ω on the mean particle diameter was also investigated. The stirring rates were varied from 50 to 800 min^{-1}. The reaction mode was the same as in the previous feeding rate investigations (150 ml of the microemulsion containing K_2SO_4 was charged into the reactor and the other 150 ml of the microemulsion containing $BaCl_2$ was fed with a feeding rate Q_f of 35 ml/min, α = 0.96, γ = 0.15, and T = 25 °C.

The experimental results show that the increase of the stirring rate ω does not change significantly the particle size (Fig. 4.20).

a)

b)

c)

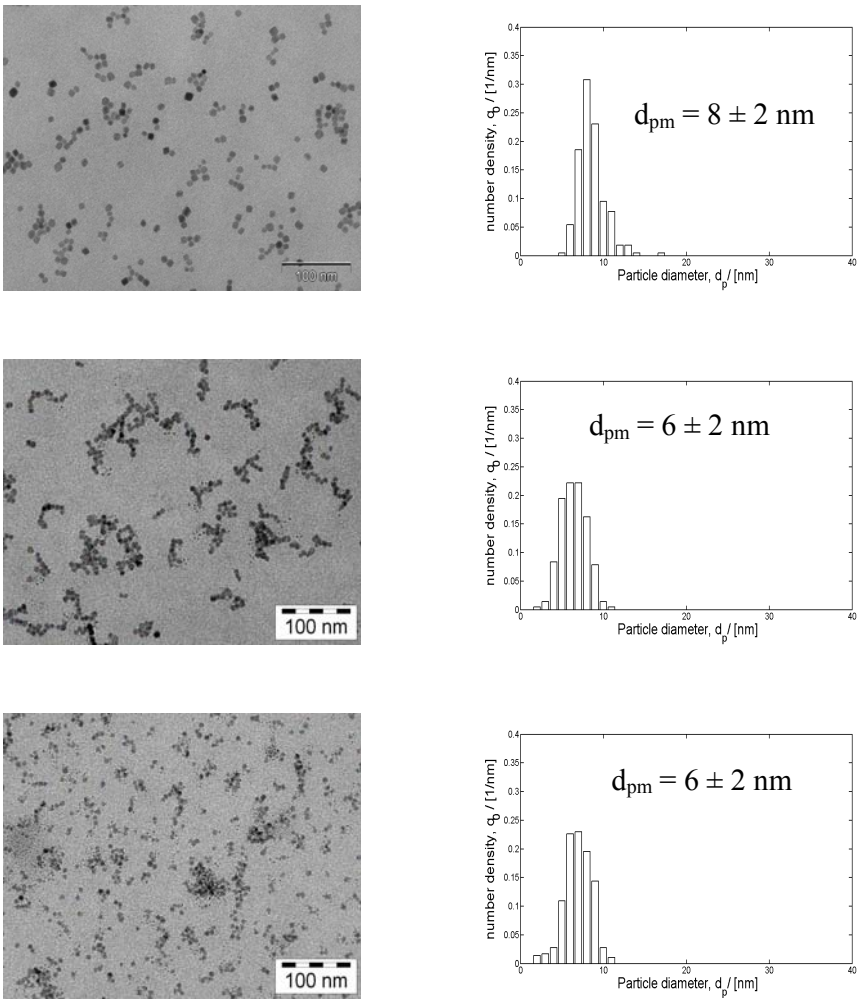

Fig. 4.20: TEM images of $BaSO_4$ nanoparticles (left) and the corresponding particle size distribution histogram (right) for different stirring rates ω : a) ω = 50 min^{-1} b) ω = 300 min^{-1}, c) ω = 800 min^{-1} (Fixed operating conditions: α = 0.96, γ = 0.15, T = 25 °C, initial concentration ratio R_c^0 = 1, feeding sequence: 0.1 mol/l $BaCl_2$ into 0.1 mol/l K_2SO_4, and Q_f = 35 ml/min).

4.3.4 Feeding sequence

In order to investigate the effect of the feeding sequence on the mean particle diameter, microemulsion precipitations were carried out in two different ways. Firstly, precipitation was carried out by feeding a $BaCl_2$ microemulsion into a K_2SO_4 microemulsion in the reactor.

Secondly, a K_2SO_4 microemulsion was fed into a $BaCl_2$ microemulsion in the reactor. Experiments were carried out at $\alpha = 0.96$, $\gamma = 0.15$, $T = 25\ ^oC$, $\omega = 300\ min^{-1}$, and $Q_f = 35$ ml/min.

a)

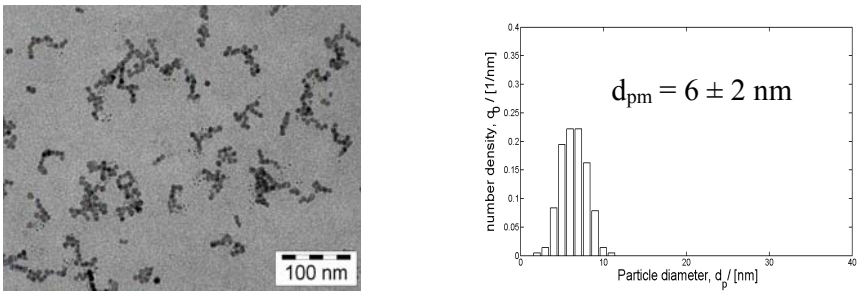

b)

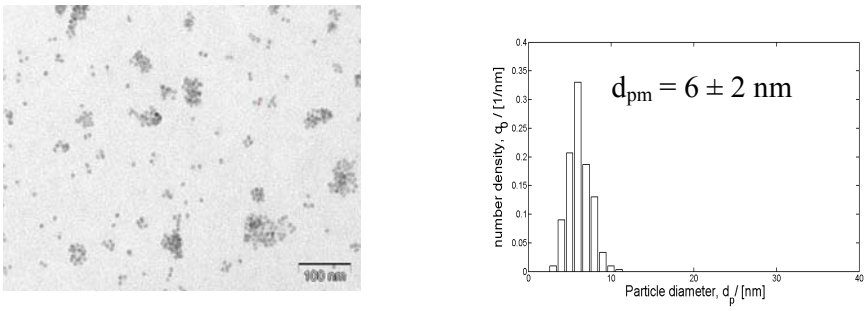

Fig. 4.21: TEM images of $BaSO_4$ nanoparticles (left) and the corresponding particle size distribution histogram (right) prepared with different feeding sequences: a) 0.1 mol/l $BaCl_2$ into 0.1 mol/l K_2SO_4 b) 0.1 mol/l K_2SO_4 into 0.1 mol/l $BaCl_2$ (Fixed operating conditions: $\alpha = 0.96$, $\gamma = 0.15$, $T = 25\ ^oC$, $Q_f = 35$ ml/min, $\omega = 300\ min^{-1}$, and initial concentration ratio $R_c^0 = 1$).

Fig. 4.21 shows that the feeding sequence does not change significantly the mean particle diameter. This result is in agreement to Schmidt's (2000) findings. He demonstrated for Pd-particle precipitation that the feeding sequence of reactant does not have a significant impact on the final mean particle size.

4.3.5 Initial concentration

Lamer and Dinegar (1959) described that the supersaturation is mainly influenced by the reactant concentration. A higher concentration of the reactant leads to a higher supersaturation level resulting in a high number of smaller particles. In order to investigate the

effect of the initial reactant concentration, microemulsions containing different initial concentrations of both reactants ($BaCl_2$, K_2SO_4) were applied in the present study.

a)

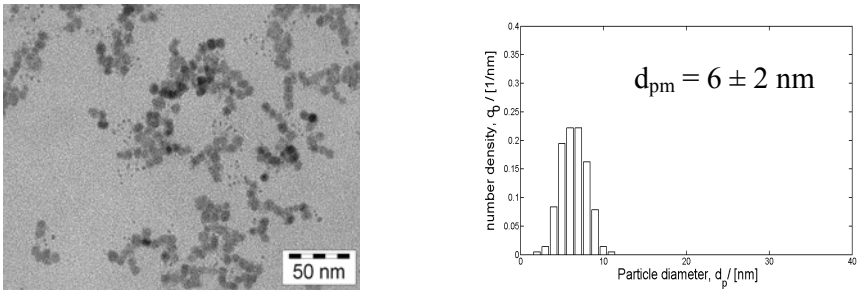

b)

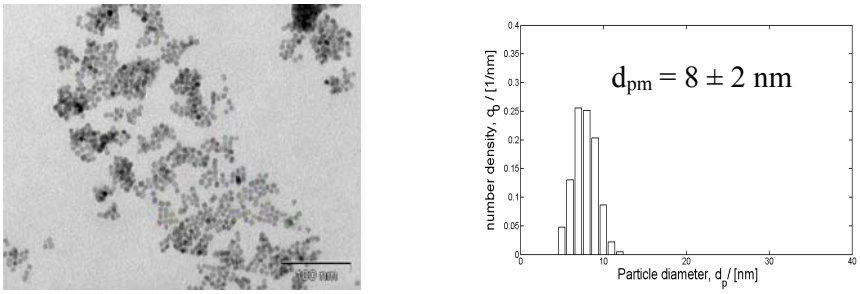

c)

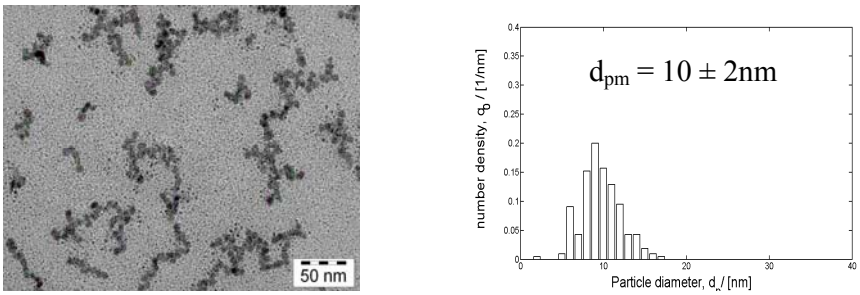

Fig. 4.22: TEM images of $BaSO_4$ nanoparticles (left) and the corresponding particle size distribution histogram (right) for different initial concentrations : a) 0.1 mol/l $BaCl_2$ and 0.1 mol/l K_2SO_4, b) 0.05 mol/l $BaCl_2$ and 0.05 mol/l K_2SO_4, c) 0.01 mol/l $BaCl_2$ and 0.01 mol/l K_2SO_4 (Fixed operating conditions: $\alpha = 0.96$, $\gamma = 0.15$, T = 25 ^oC, $Q_f = 35$ ml/min, feeding sequence: $BaCl_2$ into K_2SO_4, and $\omega = 300$ min^{-1}).

Fig. 4.22 presents TEM micrographs and corresponding particle size distributions of $BaSO_4$ nanoparticles prepared with different initial concentrations of both reactants. They show that the particles prepared with a higher initial concentration are smaller in size. For explanation one has to consider the droplet occupancy number. This number represents the

average number of liquid $BaSO_4$ molecules inside one single droplet. In the case of higher initial concentrations the occupancy number increases resulting in a larger number of nuclei being formed in the microemulsion droplet population and a smaller final mean particle diameter correspondingly.

4.3.6 Initial concentration ratio

In this particular study, microemulsion precipitations had been carried out using 11 different initial concentration ratios R_c^0 in two sets of experiments. In Set 1, the K_2SO_4 concentration was kept constant at 0.1 mol/l and the $BaCl_2$ concentration was varied at 0.1 mol/l, 0.075 mol/l, 0.05 mol/l, 0.025 mol/l, 0.01 mol/l, and 0.005 mol/l. Fig. 4.23 displays the obtained TEM images and corresponding particle size distributions.

a)

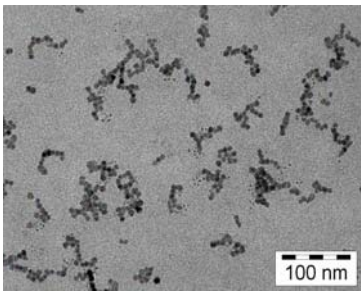

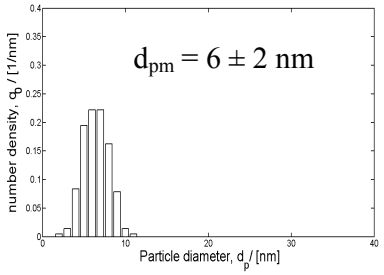

b)

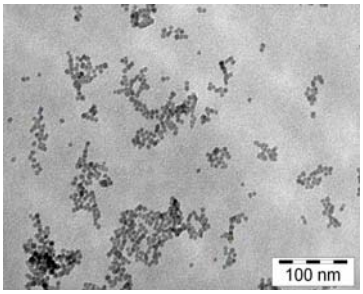

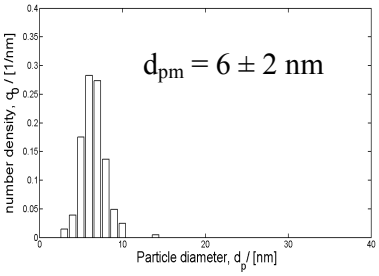

c)

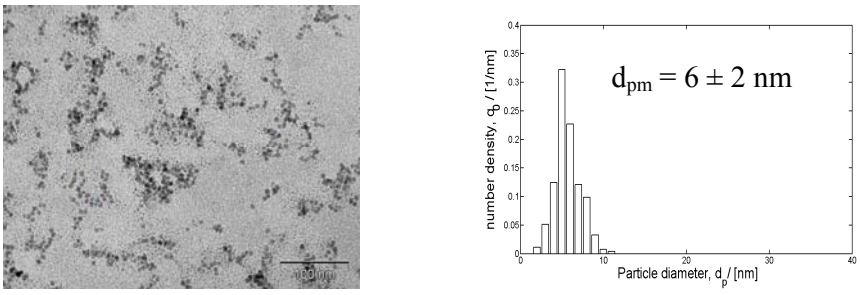

d)

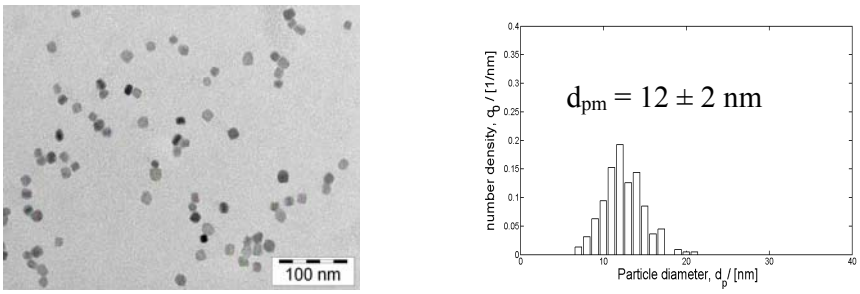

e)

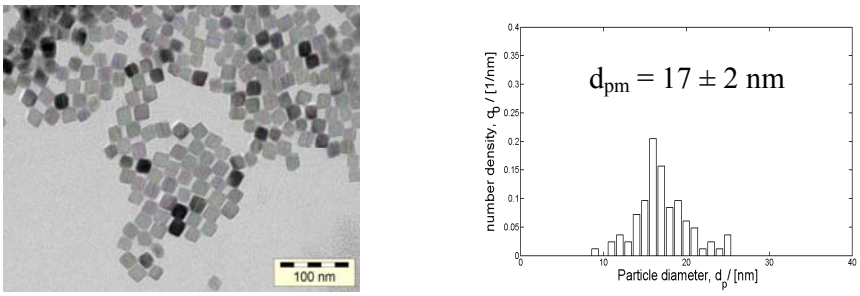

f)

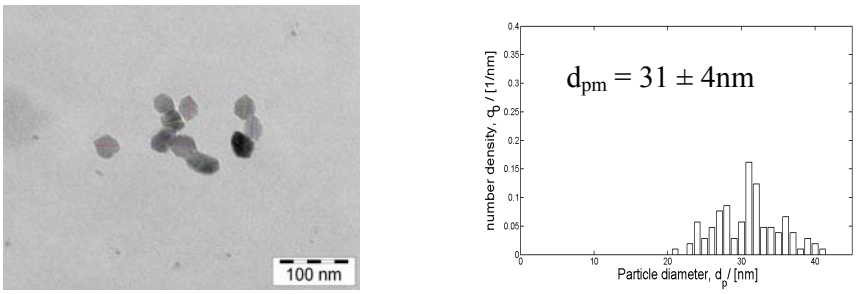

Fig. 4.23: TEM images of $BaSO_4$ nanoparticles (left) and the corresponding particle size distribution histogram (right) prepared with different initial concentration ratios R_c^0: a) 1.0 b) 0.75 c) 0.5 d) 0.25 e) 0.1 f) 0.05 (Fixed operating conditions: $\alpha = 0.96$, $\gamma = 0.15$, $T = 25\ ^oC$, $Q_f = 35$ ml/min, feeding sequence: $BaCl_2$ into K_2SO_4, and $\omega = 300\ min^{-1}$).

The corresponding experimental results for Set 2 where the $BaCl_2$ concentration was kept constant at 0.1 mol/l and the K_2SO_4 concentrations was varied at 0.1 mol/l, 0.075 mol/l, 0.05 mol/l, 0.025 mol/l, 0.01 mol/l, and 0.005 mol/l are illustrated in Fig. 4.24.

a)

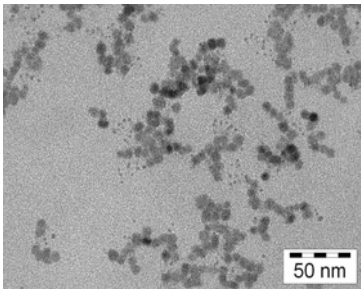

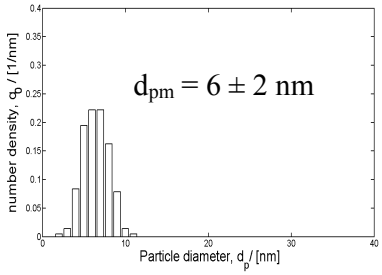

b)

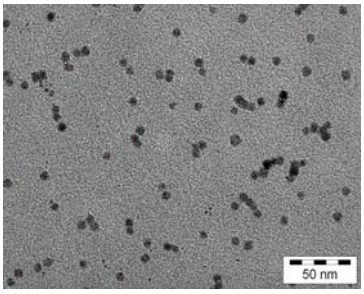

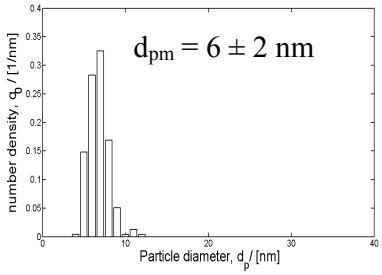

c)

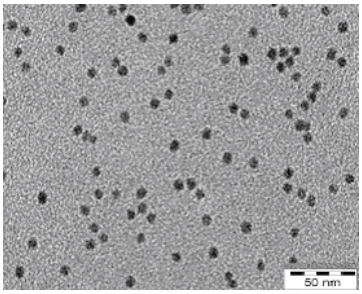

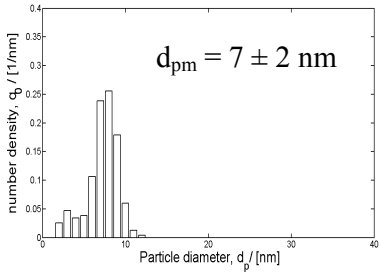

d)

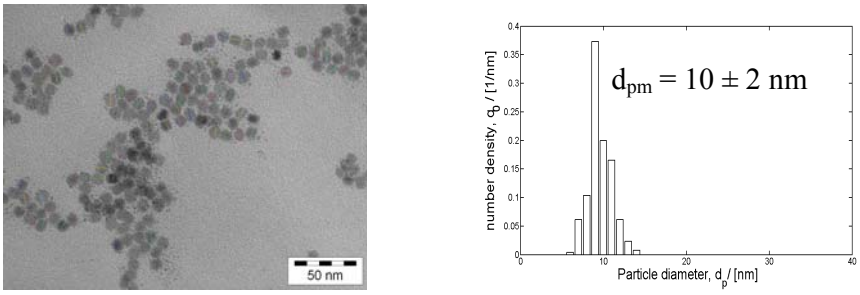

e)

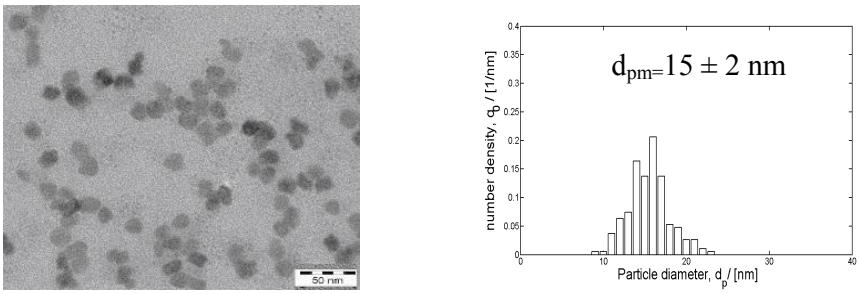

f)

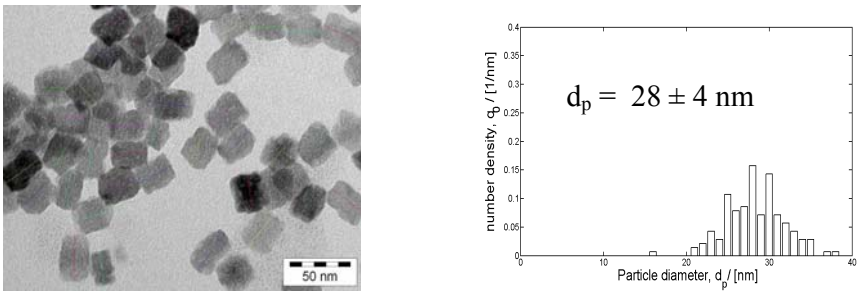

Fig. 4.24: TEM images of $BaSO_4$ nanoparticles (left) and the corresponding particle size distribution histogram (right) prepared with different initial concentration ratios R_c^0: a) 1.0, b) 1.33 c) 2 d) 4 e) 10 f) 20. (Fixed operating conditions: α = 0.96, γ = 0.15, T = 25 ^oC, Q_f = 35 ml/min, feeding sequence: $BaCl_2$ into K_2SO_4, and ω = 300 min^{-1}).

Fig. 4.25 presents the data from microemulsion precipitation experiments (Fig. 4.23 and 4.24), in a single plot. Since the decreasing of the initial concentration ratio for Set 1 and the increasing of the initial concentration ratio for Set 2 represents non-stoichiometric conditions. These non-stoichiometric feeding conditions will lead to lower supersaturation and result in bigger particles. On the contrary in the case of bulk precipitation non-stoichiometric feeding conditions which lead to higher supersaturation were being applied (see chapter 3.4.1). Therefore, the non-stoichiometric conditions in bulk phase precipitation in this work will

result in smaller particles while microemulsion precipitation results in bigger particles. Concerning the shape of particles, it is observed that smaller particles do have a spherical shape, whereas larger particles have a cubic shape.

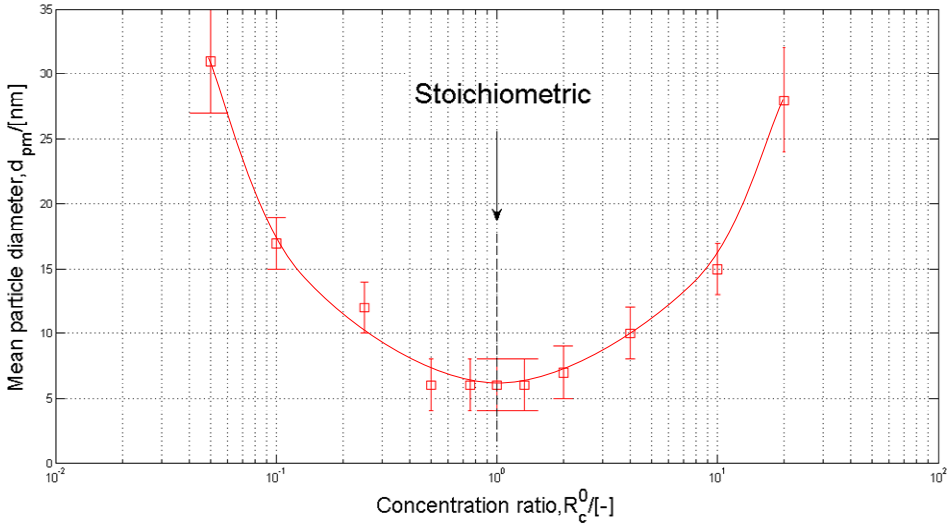

Fig. 4.25: Mean particle diameter d_{pm} at different initial concentration ratios

The bigger particles obtained from non-stoichiometric condition experiments can be explained also by the possible liquid $BaSO_4$ molecules occupancy in the emulsion droplets. As one single molecule of liquid $BaSO_4$ inside the droplet already leads to a supersaturation S above a value of 2000 (see Fig. 2.17), the concentration of reactants applied in this experiment already fixed likewise the supersaturation condition inside the water droplets. It can be calculated that inside a 5 nm water droplet only 3.9×10^{-4} $BaSO_4$ molecules can be dissolved. This consideration implies that the droplet occupancy number plays a very important role. The exchange of molecules during droplet fusion-fission events may lead to an increase of the number of molecules inside one particular droplet. This leads to the accumulation of dissolved $BaSO_4$ molecules in the droplets and after reaching a critical number N_{crit}, nuclei inside the droplets are formed. Subsequent droplet fusion-fission events may then transport additional $BaSO_4$ molecules into the droplet and these molecules grow onto the already generated nucleus.

Based on the previous discussion, as the initial concentration ratio moves from the stoichiometric condition for microemulsion precipitation, one can argue that the number of molecules reaching the critical molecules number for nucleation N_{crit} inside the droplets also decreases due to lower probability of the nucleation event. If this reason is true, then only a

few particles can undergo growth and subsequently result in a bigger particle diameter. On the contrary, if the initial concentration ratio is closer to the stoichiometric conditions ($R_c^0 = 1$), then the number of $BaSO_4$ molecules being dissolved inside the droplets is increased, the supersaturation inside the droplets increases, more nucleation events take place and this would reduce the mean particle diameter.

Unfortunately, the total number of particles precipitated in the microemulsion is not easily accessible from TEM pictures. Several preparation steps were applied between the precipitation and the final size measurement, and the total number of particles in an experiment can hardly be measured according to Adityawarman et al., (2005). However, numerical simulations can also be used to estimate the total number of particles [Voigt et al., 2005 and Niemann et al., 2006].

It also can be seen that the droplet size is usually smaller than the mean particle diameter. A possible explanation is related to the ultra-high interfacial elasticity between the water core and the oily phase at the present microemulsion system [Kandori et al., 1988]. This high interfacial elasticity makes the size and the shape of the particle inside the droplet strongly dependent on the reaction conditions. At the following chapter 5, the experimental results will be qualitatively analyzed in more detail by the mathematical model which is developed.

Chapter 5

Discussion and model-based interpretation

5.1 Process model for the nanoparticle synthesis in microemulsions

The formation of nanoparticles in microemulsions is a complex process arising from different involved population dynamic mechanisms like droplet fusion and fission, chemical reaction, nucleation and growth of particles. A fundamental understanding and analysis of this process is only possible by the formulation of an appropriate process model on different levels of detail. Mathematical models are developed and used as simulation tools for:

- the analysis of interactions between the various population dynamic mechanisms,
- the estimation of important kinetic parameters which are not accessible by experiment like the droplet exchange rate and the nucleation and growth rate constant,
- the prediction of the scale-up behaviour and
- for model-based process control of technical-scale production process.

Several model structures and solution methods have been reported in the literature. Those are namely the population balance method [Sato et al., 1995, Natarajan et al., 1996, Bandyopadhyaya, 1997, Kumar et al., 2004, Niemann et al., 2006], the Monte-Carlo method [Li and Park, 1999, Bandyopadhyaya, 2000, Voigt et al., 2005], and model based on the moment equations [Bandyopadhyaya, 2001] and several analytical steady state process models [Nagy, 1999, Hirai, 1993, Schmidt, 2000]. A strategy for combining the population balance equation and the Monte-Carlo method was proposed as well by Hernandez (2002) and Bandyopadhyaya (2000).

In the following study a reduced deterministic model is presented. All important population dynamic mechanisms are implemented in the model equations and a numerically efficient solution is obtained by the use of mean values and an equilibrium distribution instead of the dynamic solution of the population balance equation. The major output of the studied model is the mean particle diameter as a function of the initial concentration ratio R_c^0. The mean particle diameter is an easily obtainable parameter which gives first important information about the quality of a particulate product.

The derived model is based on performed experiments (see chapter 4). A scheme of the used process and important population dynamic mechanisms are given in Fig. 5.1. The semi-batch operated stirred tank reactor was initially filled with a microemulsion containing

dissolved K_2SO_4 inside the droplets (V_r = 150 ml), while a second microemulsion with the same volume (150 ml) and the second dissolved reactant $BaCl_2$ was used for the feed (with a constant feed rate Q_f). Once two microemulsions are mixed, droplet fusion and fission leads to the formation of the liquid $BaSO_4$ molecules (denoted by C) by chemical reaction. When the amount of C molecules reaches the critical number of molecules needed to form a stable nucleus $N_{crit,}$ particles P are formed. A particle P grows into a bigger particle P' by the consumption of C, which entered the droplet by fusion and fission with other droplets containing C molecules.

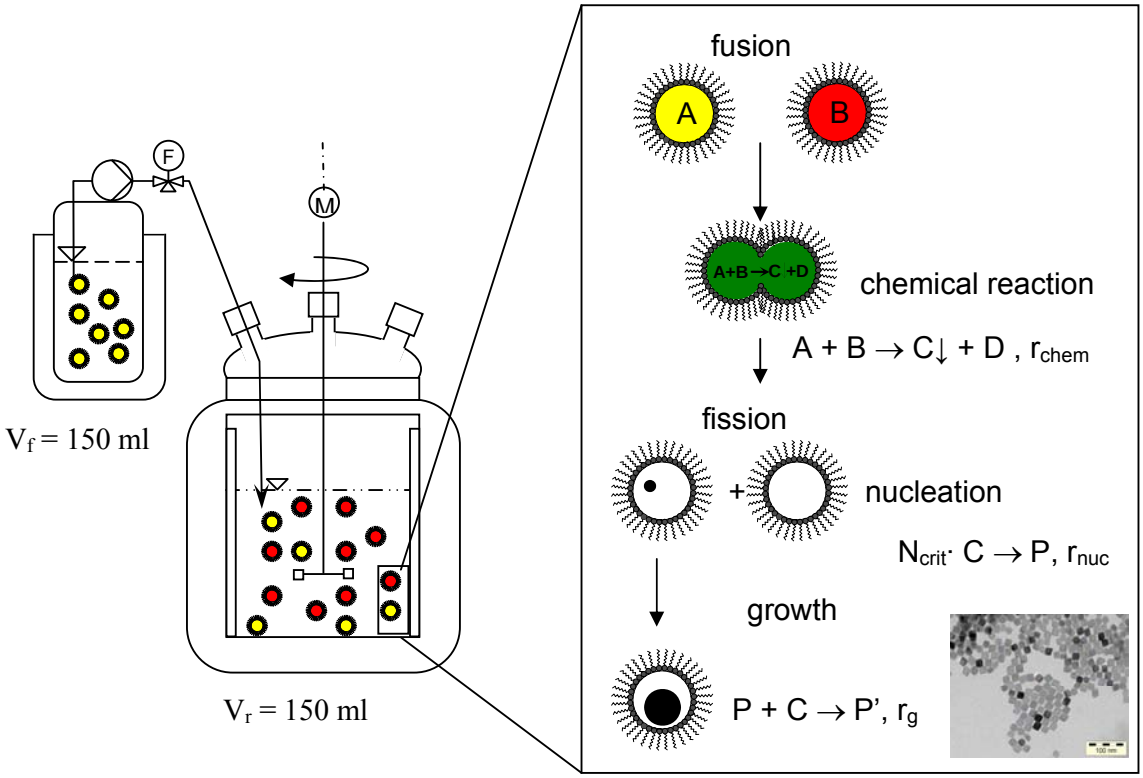

Fig. 5.1: Process scheme (left) and important population dynamic mechanisms (right).

The derived process model is developed to investigate mainly the dependency of the initial concentration ratio R_c^0 on the mean particle diameter and also for a detailed analysis of the process dynamics for a better understanding of the nanoparticle formation mechanism inside microemulsion droplets. The nucleation and growth rate constants ($k_{n,me}$ and $k_{g,me}$) of the kinetic rate expressions are estimated to fit best the experimental result presented in chapter 4.3.6. Furthermore, the influence of important model parameters such as the droplet size d_{drop} and the critical number of molecules N_{crit} on the predicted parameters is studied in detail by a sensitivity analysis. In the following paragraph each stage of the particle formation

process inside the water droplets is explained: chemical reaction, nucleation and particle growth.

Chemical reaction

Rauscher et al. (2005) presented a time scale analysis for the precipitation of $CaCO_3$ in a similar microemulsion system as used in the present work, where typical time constants for the chemical reaction τ_{chem}, the droplet exchange τ_{ex}, and nucleation τ_{nuc} and particle growth τ_g were estimated. The time constants of the regarded mechanisms are specified in Table 5.1.

Table 5.1: Typical time constants for microemulsion precipitation [Rauscher et al., 2005].

τ_{chem}	τ_{nuc}	τ_{ex}	τ_g
10^{-12}-10^{-8}s	10^{-12}-10^{-8}s	10^{-8}-10^{-3}s	10^{-3}-10^{-1}s

The presented time constants show that the chemical reaction and the nucleation are the fastest phenomena occurring in the microemulsion system. Due to the same time scales of these processes the chemical reaction is regarded as an instantaneous step in this study. Thus, the fastest dynamics in this process is represented by the nucleation. By this implementation of the chemical reaction the liquid molecules C are instantaneously formed, when droplets with either one of the reactants are mixed by the droplet exchange [Nagy, 1989 and Natarajan et al., 1996]. In this study the liquid molecules C ($BaSO_4$) and the consequent solid precipitation product are formed according to the following reaction scheme:

$$BaCl_2\,(l) + K_2SO_4\,(l) \rightarrow BaSO_4(s)\downarrow + 2\,KCl\,(l). \tag{5.1}$$

Symbolically, equation 5.1 is represented by

$$A + B \rightarrow C\downarrow + D\,. \tag{5.2}$$

The notation, A, B, C, and D corresponds to barium chloride ($BaCl_2$), potassium sulphate (K_2SO_4), barium sulphate ($BaSO_4$), and potassium chloride (KCl), respectively.

Atik and Thomas (1981) showed by their experimentally obtained data that the distribution of the dissolved salts inside the water droplets of microemulsion system followed a Poisson distribution. The use of a Poisson distribution in the presented model leads to the assumption that liquid molecules C inside all droplets of the reactor are distributed according to the Poisson distribution and that newly formed C inside one droplet is immediately distributed by the droplet exchange within the reactor to conserve this equilibrium distribution [Hirai, 1993, Bandyopadhyaya, 2000]. The side product KCl is assumed to have no effect on

the particle formation of $BaSO_4$. It is therefore not taken into account in the presented simulation study.

The Poisson distribution gives the number of droplets containing i molecules of C as proportion p_i of the total amount of droplets in the system (i is an integer number). The only parameter needed to calculate p_i is the average droplet occupancy λ with liquid molecules C. The Poisson distribution is then defined by

$$p_i(t) = \frac{\lambda(t)^i \cdot \exp(-\lambda(t))}{i!}. \tag{5.3}$$

The average droplet occupancy λ with the liquid molecules C at a specific time t is given by

$$\lambda(t) = \frac{n_C(t)}{n_{drop}(t)}, \tag{5.4}$$

where $n_C(t)$ is the total amount of liquid molecules C inside the reactor in moles (see equation 5.30) and $n_{drop}(t)$ is the total number of droplets inside the reactor at a specific time in moles. $n_{drop}(t)$ can be calculated from the total amount of water at a specific time $V_w(t)$ and the droplet diameter d_{drop}. This relation is given by

$$n_{drop}(t) = \frac{V_w(t)}{k_{vd} \cdot {d_{drop}}^3 \cdot N_A}, \tag{5.5}$$

where k_{vd} is the droplet shape factor and N_A is Avogadro's number.

A typical Poisson distribution of the liquid molecules C ($BaSO_4$ molecules) is depicted in Fig. 5.2 for an occupancy number of $\lambda = 3.5$.

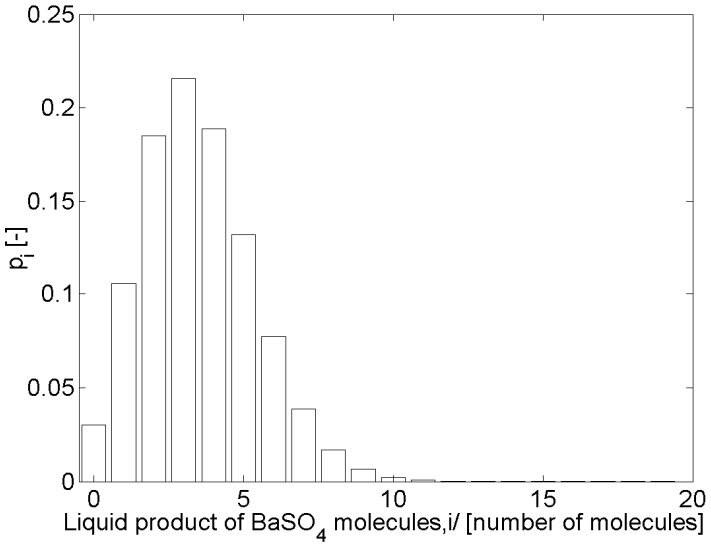

Fig. 5.2: Poisson distribution for $\lambda = 3.5$.

The Poisson distribution in Fig. 5.2 shows that droplets, which contain exactly 5 molecules, amount about 13% of all droplets in the system.

Nucleation

After the establishment of the Poisson distribution of the liquid molecules C, the second step of the nanoparticle formation is the nucleation. Nucleation occurs inside the water droplets similar to the known bulk phase precipitation reaction scheme. New particles P are born if the number of C molecules inside one droplet is greater than the critical number of molecules needed to form a stable nucleus N_{crit} [Hirai, 1993, Schmidt, 2000, Voigt et al., 2005, and Niemann et al., 2006]. Typical values of N_{crit} found in the literatures are ranging between 2 and 8, but also values above 10 could be found for bulk precipitation [Kashchiev and Van-Rosmalen 2003]. Table 5.2 gives an overview on the models proposed in literature and corresponding N_{crit} values (for details see Niemann et al., 2006).

Table 5.2 List of proposed models and the corresponding N_{crit} values.

Literature source	**N_{crit}**	**Numerical method**	**Experimental system**
Bandyopadhyaya (1997)	5	Moment	$CaCO_3$
Bandyopadhyaya (2000)	2…5	Monte-Carlo	$CdS/Fe(OH)_3$
Jain and Mehra (2004)	2	Monte-Carlo	CdS
Kumar (2004)	2…8	Population Balance	CdS
Natarajan (1996)	2…6	Population Balance	Ni_2B
Ravet/Nagy (1987)/(1989)	2	Analytical	Ni_2B,Co_2B, NiCoB
Schmidt (2000)	5	Analytical	Pd
Hirai (1993)	5	Analytical	TiO_2

The nucleation mechanism can be represented by the following scheme:

$$N_{crit} \cdot C \rightarrow P\,. \tag{5.6}$$

The molecular nucleation rate r_{nuc} of the dissolved C can be obtained from the nucleation rate B_{nuc} and Avogadro's number N_A according to equation 5.7:

$$r_{nuc} = \frac{B_{nuc}}{N_A}\,. \tag{5.7}$$

Microemulsion-specific nucleation rate approaches are not available in the literature so far and therefore an own microemulsion specific nucleation rate approach will be presented in this study. The used approach for B_{nuc} is based on the nucleation theory for bulk phase precipitation of $BaSO_4$ published by Baldyga et al. (1995), where the main driving force for nucleation is assumed to be the supersaturation concentration difference Δc (see equation 5.8).

$$B_{nuc} = k_n \cdot \Delta c^b. \tag{5.8}$$

The nucleation rate constant is denoted as k_n and the order of the nucleation rate as b. The concentration difference Δc is calculated from the difference between the square root of the actual concentrations of both reactant ions (barium and sulphate ions) and the solubility product of $BaSO_4$, K_{sp}, in water. It is given by:

$$\Delta c = \left(\sqrt{c_{Ba^{2+}} \cdot c_{SO_4^{2-}}} - \sqrt{K_{sp}} \right), \tag{5.9}$$

where the solubility product K_{sp} is calculated from:

$$K_{sp} = c_{Ba^{2+}}^{sat} \cdot c_{SO_4^{2-}}^{sat}. \tag{5.10}$$

In Baldyga et al. (1995) the parameters of the nucleation rate approach were classified according to the concentration range. For $\Delta c < 0.01$ mol/l, B_{nuc} is defined as

$$B_{nuc} = 6 \cdot 10^{12} \Delta c^{1.775}, \tag{5.11}$$

and for $\Delta c > 0.01$ mol/l, B_{nuc} is defined as

$$B_{nuc} = 2.53 \cdot 10^{39} \Delta c^{15}. \tag{5.12}$$

Since the solubility product K_{sp} of $BaSO_4$ is very low (1.1×10^{-10} mol^2/l^2) [Wong et al., 2001], the term of K_{sp} in equation 5.9 can be neglected due to the fact that already one molecule inside a droplet with a diameter of 5 nm equals to a concentration in the order of 10^{-2} mol/l which is 3 order higher than saturation concentration of $c_{BaSO_4}^{sat}$ ($\sim \sqrt{K_{sp}}$). Thus, in the microemulsion-specific nucleation rate approach, Δc can be reduced to Δc_{me} with the definition:

$$\Delta c_{me} = \sqrt{c_{Ba^{2+}} \cdot c_{SO_4^{2-}}}. \tag{5.13}$$

With this definition, the proposed microemulsion-specific nucleation rate approach $B_{nuc,me}$ is expressed as follows:

$$B_{nuc,me} = k_{n,me} \cdot \Delta c_{me}^{N_{crit}}, \tag{5.14}$$

where $k_{n,me}$ is the nucleation rate constant. As the nucleation rate order b approach are usually very high and are only empirically obtained from experimental data then in this work, the nucleation rate order b in the bulk phase approach is exchanged by N_{crit} for the microemulsion-specific nucleation approach.

Growth

The growth of the small nuclei to bigger particles can be initiated by several mechanisms as explained in chapter 2.2.3. Mechanisms like the transport of dissolved $BaSO_4$ molecules by diffusion or convection to the particle surface followed by a reaction on the surface or the agglomeration of small nuclei can be responsible for particle growth. In the case of microemulsion precipitation, the second mechanism can be neglected due to the protecting surfactant monolayer around each droplet and the very low occupancy of droplets with particles (see also Schmidt, 2000). The growth of one particle P into a bigger particle P' by the consumption of C is expressed by equation 5.15.

$$P + C \rightarrow P' . \tag{5.15}$$

In this study, the consumption rate of dissolved molecules C due to growth is represented by r_g. It is derived from the total molar transfer flux due to crystal growth [Gerstlauer et al., 2002] by:

$$r_g = \frac{3 \cdot k_{vp} \cdot \rho_C}{M_C} \cdot \int_0^\infty d_p{}^2 \cdot G \cdot f(d_p) \cdot d(d_p) , \tag{5.16}$$

where k_{vp} is the particle shape factor, ρ_C and M_C are the density and the molecular weight of $BaSO_4$, respectively. The growth rate G can be interpreted as the velocity of particle growth. In order to use equation 5.16 in the model, a further assumption is proposed here. The integral term in equation 5.16 is simplified by using the mean particle diameter d_{pm} in the presented model instead of the whole distribution. Thereby, the particle number density function $f(d_p)$ is replaced by the dirac delta function δ as illustrated in Fig. 5.3.

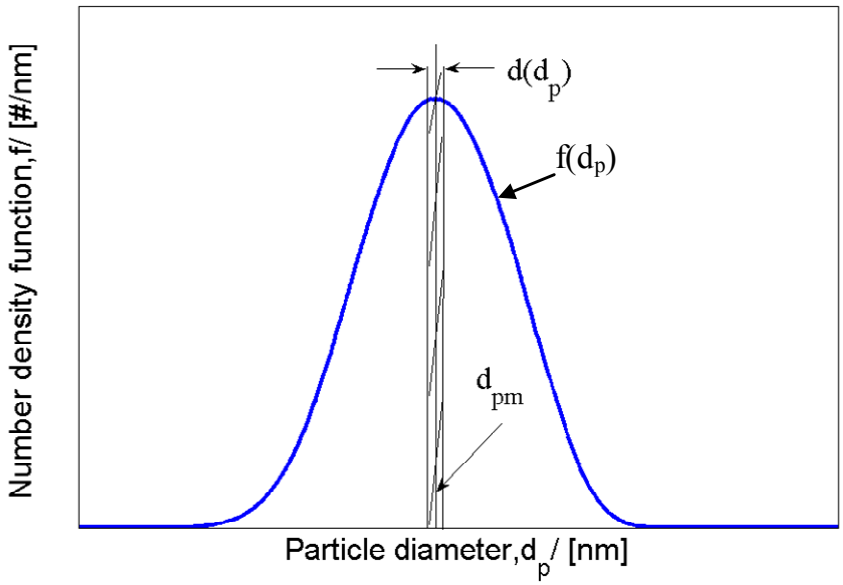

Fig. 5.3: Representation of $f(d_P)$ and the mean particle diameter d_{pm}.

If a size-independent growth rate G is assumed, the integral part in equation 5.16 can be written as:

$$\int_0^\infty d_p^{\,2} \cdot G \cdot f(d_p) \cdot d(d_p) \approx G \int_0^\infty d_p^{\,2} \cdot \delta(d_p - d_{pm}) \cdot d(d_p). \tag{5.17}$$

By inserting the expression

$$N_P = \int_0^\infty \delta(d_p - d_{pm}) \cdot d(d_p) \tag{5.18}$$

for the total number of particles N_P into equation 5.17, the rate r_g can be simplified as follows:

$$r_g = \frac{3 \cdot k_{vp} \cdot \rho_C \cdot d_{pm}^{\,2} \cdot G \cdot N_P}{M_C}. \tag{5.19}$$

As r_g should depend on n_P in moles instead of the total number of particles N_p, equation 5.19 is rewritten in the following form:

$$r_g = \frac{3 \cdot k_{vp} \cdot \rho_C \cdot n_P \cdot N_A \cdot d_{pm}^{\,2} \cdot G}{M_C}, \tag{5.20}$$

where

$$N_p = n_P \cdot N_A. \tag{5.21}$$

Similar to the nucleation rate approach, the growth rate G also depends on the concentration of the dissolved C molecules in the liquid phase. The microemulsion-specific

growth rate G_{me} is also derived from the bulk phase approach published by Baldyga et al. (1995) and modified according to equation 5.22:

$$G_{me} = k_{g,me} \cdot \Delta c_{me}{}^{g}, \tag{5.22}$$

where the growth rate surface integration–controlled growth g = 2 is used in accordance with Balydyga et al. (1995) and Δc_{me} is calculated by equation 5.13. In this work, the diffusional growth inside the water droplet can be neglected due to the very small droplet size and very rapid droplet fusion-fission events.

Mass balances

Since the formation of nanoparticles inside water droplets involves several components, the underlying specific mass balance equations are formulated to quantify the dynamic behaviour of each component during the reactor operation. The material balances are limited to the water phase and therefore the water droplets of the microemulsion system can be regarded as a pseudo-homogeneous reaction medium [Schmidt, 2000].

Under consideration of the feeding rate $n_A{}^F$ in the semi-batch process, the component mass balance for reactant A ($BaCl_2$) is given by

$$\frac{dn_A}{dt} = n_A{}^F - r_{chem} \cdot V_w(t). \tag{5.23}$$

The rate of chemical reaction r_{chem} in equation 5.23 is defined by

$$r_{chem} = k_{chem} \cdot c_A \cdot c_B. \tag{5.24}$$

In case of a very fast chemical reaction, the reactant A ($BaCl_2$) as feeding reactant is consumed instantaneously together with an equal amount of the second reactant B (K_2SO_4) and both are immediately converted into the liquid molecules C ($BaSO_4$). Therefore, during the feeding time, the concentration of the feeding reactant c_A in the reactor is close to 0 and equation 5.23 can be simplified in the following way:

$$\frac{dn_A}{dt} \approx 0 \approx n_A{}^F - r_{chem} \cdot V_w(t), \tag{5.25}$$

where

$$n_A{}^F \approx r_{chem} \cdot V_w(t), \tag{5.26}$$

and therefore

$$r_{chem} \approx \frac{n_A{}^F}{V_w(t)}. \tag{5.27}$$

The mass balance of reactant B (K_2SO_4) initially present inside the reactor is given by

$$\frac{dn_B}{dt} = -r_{chem} \cdot V_w(t) \approx -n_A{}^F . \tag{5.28}$$

The total volume of the water phase at a specific time $V_w(t)$ can be calculated by

$$V_w(t) = V_w(0) + Q_w \cdot t , \tag{5.29}$$

where Q_w stands for the feeding rate of the water phase into the reactor.

The mass balance of the dissolved molecules C ($BaSO_4$ molecules) is given by

$$\frac{dn_C}{dt} = r_{chem} \cdot V_w(t) - N_{crit} \cdot r_{nuc} \cdot V_{wr}(t) - r_g . \tag{5.30}$$

The initial conditions for the mass balances are given by $n_A(t = 0) = 0$, $n_B(t = 0) = n_{B,0,}$ $n_C(t = 0) = 0$, $n_P(t = 0) = 0$, $n_{drop}(t = 0) = n_{drop,0}$,$V_w(t = 0) = V_w(0)$, $V_{wr}(t = 0) = 0$.

The term on the left side of equation 5.30 represents the accumulation of the dissolved molecules C and the first term of the right side represents the production of dissolved molecules C due to the chemical reaction, which equals to the feeding rate according to equation 5.27. Moreover, the last two terms on the right side are the depletion C due to nucleation and particle growth.

The number of particles n_P in moles is balanced by

$$\frac{dn_P}{dt} = r_{nuc} \cdot V_{wr}(t) , \tag{5.31}$$

where $V_{wr}(t)$ corresponds to the reactive volume of the water phase volume $V_w(t)$ at a specific time which contains at least the critical number of molecules for nucleation N_{crit}. This reactive volume can be calculated by the reduction of the total water volume $V_w(t)$ by the part of the water, which contains less than N_{crit} molecules. This relation is given by

$$V_{wr}(t) = V_w(t) \cdot \left(1 - \sum_{i=0}^{N_{crit}-1} p_i(t) \right). \tag{5.32}$$

For the calculation of the mean particle diameter at a specific time $d_{pm}(t)$ the total amount of C molecules being bound in solid phase $n_C{}^{solid}(t)$ must be known. This quantitiy is assessable by the subtraction of the amount of dissolved molecules C, $n_C(t)$, from the total amount of C molecules $n_C{}^{total}(t)$ present in the system according to

$$n_C{}^{solid}(t) = n_C^{total}(t) - n_C(t) . \tag{5.33}$$

With this value the total number of molecules forming one particle $N_C{}^P(t)$ at a specific time can be calculated from

$$N_C{}^P(t) = \frac{n_C{}^{solid}(t)}{n_P(t)} . \tag{5.34}$$

Then the mean particle diameter at a specific time $d_{pm}(t)$ can be easily determined as follows:

$$d_{pm}(t) = \sqrt[3]{\left(\frac{V_C \cdot N_C^{\,P}}{k_{vp}} \right)}, \tag{5.35}$$

where V_C is the molecular volume of one $BaSO_4$ molecule (equation 5.36). Note that this equation is only valid when ripening and aggregation of particles can be neglected during the particle formation process.

$$V_C = \frac{M_C}{\rho_C \cdot N_A}. \tag{5.36}$$

Spherical geometry of the particles is assumed and thus $k_{vp} = \pi/6$. This assumption is based on experimental results from high resolution TEM pictures. The precipitated barium sulphate nanoparticles have a regular crystalline structure like in bulk phase precipitated barium sulphate and a spherical shape [Adityawarman et al., 2005].

The proposed model mainly consists of two differential equations (equations 5.30 and 5.31), which can be solved simultaneously by numerical methods implemented in Matlab® (version 6.5). Calculation times for the proposed model are below one second, which makes this model interesting for process control and fluid dynamic simulation studies. Unknown parameters like $k_{n,me}$, $k_{g,me}$, and N_{crit} must be fitted to the experimental data, because these values are not obtainable from the literature.

5.2 Identification of model parameters from experimental results

In this chapter the optimal model parameters concerning different initial concentration ratios R_c^0 and the feeding rates Q_f are reported. The fitted parameters are the critical number of molecules needed to form a stable nucleus N_{crit}, the nucleation rate constant $k_{n,me}$ and the growth rate constant $k_{g,me}$. It is necessary to optimize all of these parameters, because valid values for the used reaction system are not reported in the literature. The same parameter optimization procedure was chosen for each run. N_{crit} was fixed to a reasonable discrete value and the two rate constants of the particle formation mechanisms ($k_{n.me}$ and $k_{g,me}$) were estimated by the minimizing the sum of squares QS between the experimentally obtained mean particle diametesr and the simulated mean particle diameters:

$$QS = \sum_{1}^{13} \left(d_{pm\_exp} - d_{pm\_sim} \right)^2 \tag{5.37}$$

where d_{pm_exp} is the mean particle diameter from experiments and d_{pm_sim} is the mean particle diameter from the simulation. All further parameters and experimental conditions which are

used in the model, are summarized in Table 5.3 and Table 5.4 as well as the estimated optimal parameters of the particle formation mechanisms for different N_{crit}.

Table 5.3: Data used for the model simulations.

Reactor:	
$V_r(t = 0)$	= 150 ml
V_f	= 150 ml
ω	= 300 min^{-1} (Rushton turbine)
T	= 25 ^oC
Microemulsion:	
α	= 0.96
γ	= 0.15
V_{wt}	= 8.21 ml (reactor and feed)
d_{drop}	= 5 nm (DLS measurement)
Experiments:	
K_2SO_4 dissolved in the droplets inside the reactor.	
$BaCl_2$ dissolved in the droplets inside the feed.	
Set 1 (6 experiments):	
$c_{K_2SO_{4,0}}$	= 0.1 mol/l
$c_{BaCl_{2,0}}$	= 0.1/0.075/0.05/0.025/0.01/0.005 mol/l
Set 2 (5 experiments):	
$c_{K_2SO_{4,0}}$	= 0.075/0.05/0.025/0.01/0.005 mol/l
$c_{BaCl_{2,0}}$	= 0.1 mol/l
Feeding rate variation (2 experiments):	
$c_{K_2SO_{4,0}}$	= 0.1 mol/l
$c_{BaCl_{2,0}}$	= 0.1 mol/l
Q_f	= 70 and 140 ml/min
Total number of experiments for parameter fitting: 13	

Table 5.4 Optimal parameters.

N_{crit}	$k_{n,me}$ [(-)/(ls)(l^4/mol^4)]	$k_{g,me}$ [(nm/s)(l^2/mol^2)]	QS [nm^2]
4	$7.59x10^{28}$	$9.66x10^{2}$	873.02
5	$7.59x10^{29}$	$1.35x10^{2}$	133.60
6	$7.59x10^{31}$	$1.35x10^{1}$	923.83
7	$7.74x10^{33}$	1.35	1271.14
8	$7.74x10^{37}$	1.35	1336.99

A comparison of the mean particle diameters d_{pm} from experiments and simulations obtained for the two sets of experiment as well as for the feeding rate variations are shown in Fig. 5.4, Fig. 5.5 and Fig. 5.6 below. The optimum parameters which are obtained from the simulations are listed in Table 5.4.

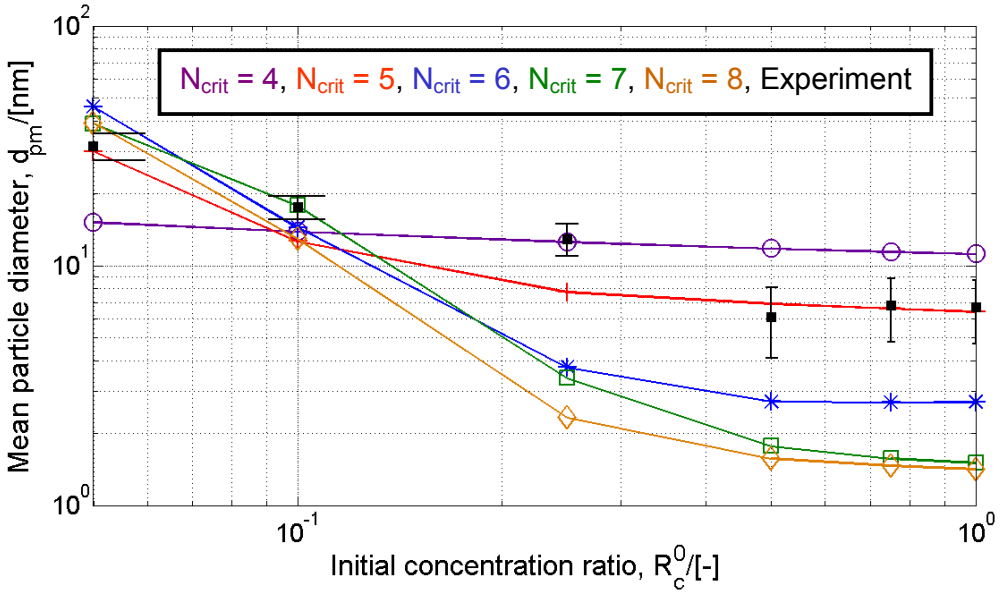

Fig. 5.4: Mean particle diameter for different initial concentration ratios R_c^0 and different N_{crit} values (Set 1).

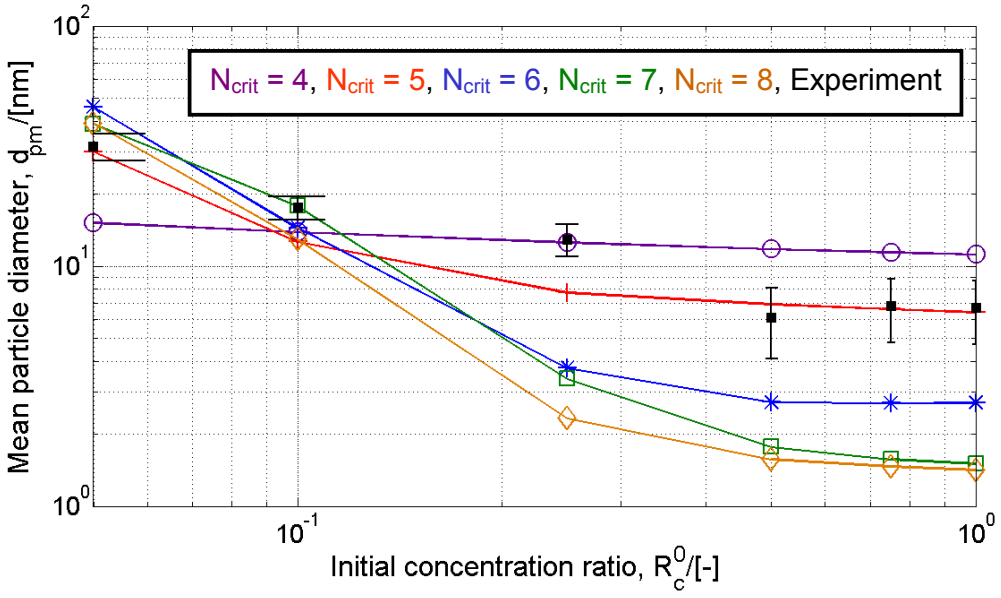

Fig. 5.5: Mean particle diameter for different initial concentration ratios R_c^0 different N_{crit} values (Set 2).

In general it was possible to find an optimal set of parameters for each specified N_{crit}, where the simulated and experimentally obtained mean particle diameters are in the same order of magnitude for all experiments. The best fit with the smallest QS-value for Set 1, Set 2, and the feeding rate experiments together is obtained for:

- $N_{crit} = 5$,
- $k_{n,me} = 7.59 \times 10^{29}$(-)/(ls)($l^5/mol^5$),
- $k_{g,me} = 1.35 \times 10^{2}$(nm/s)($l^2/mol^2$).

A comparison of both sets shows that bigger particles are generally obtained if the two reactants are initially present in a non-stoichiometric amount. For Set 1 the tendency towards bigger particles is observed for a lower initial concentration ratio R_c^0 and for Set 2 bigger particles are achieved for a higher R_c^0-value. A detailed analysis of the influence of R_c^0 on the resulting mean particle diameter will be given by investigation of the dynamic behaviour of the system (see chapter 5.3). Furthermore, the minimum of the mean particle diameter value observed in the simulations for Set 2 (Fig. 5.5) with $N_{crit} = 5$ can be explained also by the analysis of the dynamic behaviour in chapter 5.3.

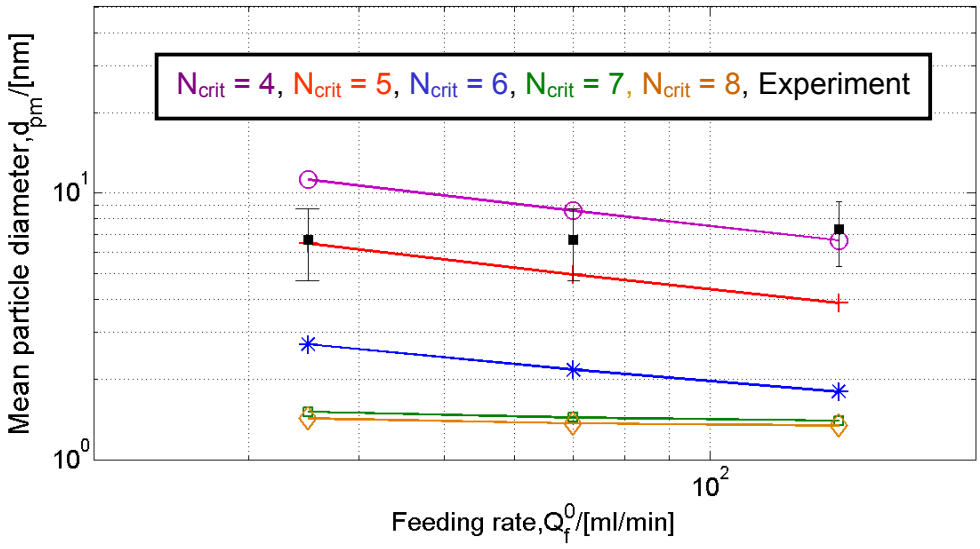

Fig. 5.6: Mean particle diameter d_{pm} for different feeding rates with $R_c^0 = 1$.

A dependence of the mean particle diameter on the feeding rate (see Fig. 5.6) is only observed in the performed simulations. Within the simulations a bigger particle size could be obtained at a lower feeding rate, whereas the experimental results indicate that the mean particle diameter is independent on the feeding rate [Voigt et al., 2005].

5.3 Simulated process dynamics

Fig. 5.7 shows the simulated dynamics of the average droplet occupancy λ for the complete Set 1. The-λ values represent the mean concentration of C inside the whole reactor and also the average supersaturation.

The general dynamic behaviour of λ is similar for all simulations of Set 1. Initially λ = 0 for all simulations, because only one reactant is present inside the reactor. With the beginning of the feeding of the second reactant λ starts to increase towards a maximum due to the formation of dissolved $BaSO_4$. The maximum is reached, when the consumption of $BaSO_4$ molecules by particle formation mechanisms is equal to the amount of newly formed $BaSO_4$ by the instantaneous chemical reaction. Particle formation and the dilution by new droplets lead to a decrease of the λ-value until the end of the feeding period.

a)

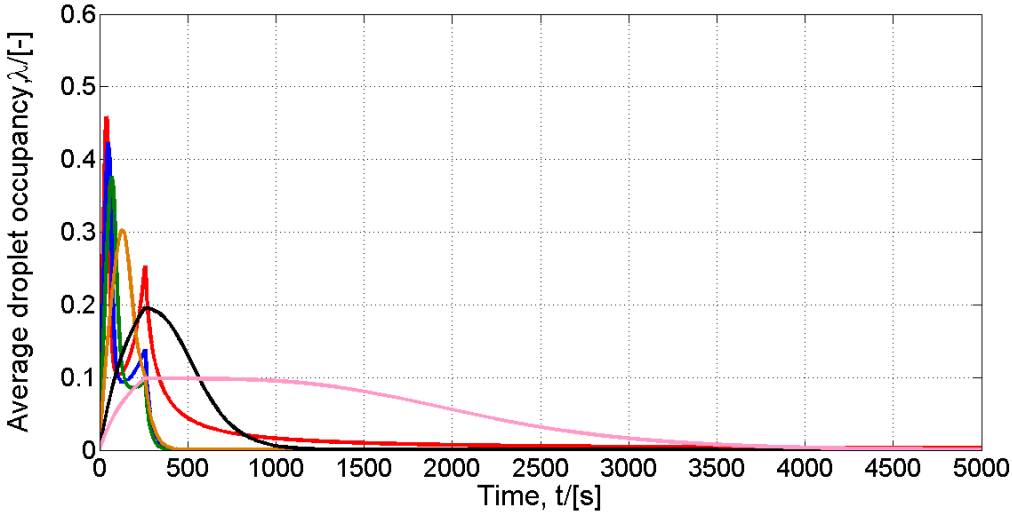

b)

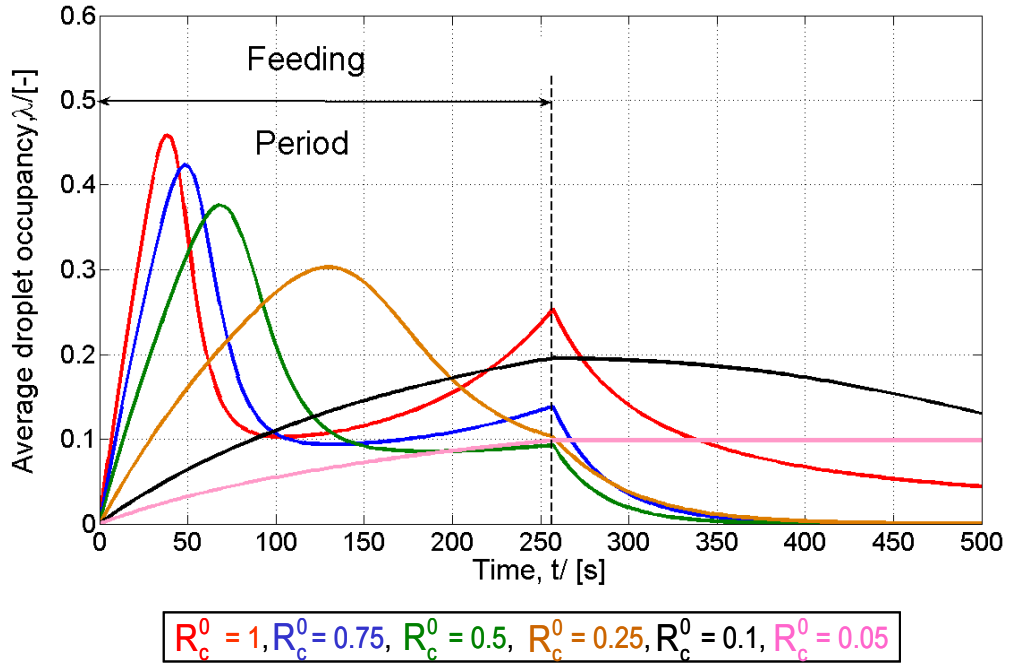

R_c^0 = 1, R_c^0 = 0.75, R_c^0 = 0.5, R_c^0 = 0.25, R_c^0 = 0.1, R_c^0 = 0.05

Fig. 5.7: a) Long-term dynamics of the average droplet occupancy λ for different initial concentration ratios R_c^0 (Set 1). b) Short-term dynamics of the average droplet occupancy λ for different initial concentration ratios R_c^0 (Set 1).

For the two smallest R_c^0-values, the maximum coincides to the end of the feeding period, because concentrations in this case are too low so that the kinetics are too slow to compensate the effect of the feeding of new reactants.

In particular, lower R_c^0-values lead to slower dynamics, because of the decreasing reactant concentration inside the droplets. The lower concentrations are tantamount to a lower supersaturation and therefore lower the rates of the particle formation processes. Simulations with the smallest R_c^0-value reach the steady state after 4000 seconds, while simulations with the higher R_c^0-value are stationary after a few hundred seconds. Additional important information in these figures can be obtained from λ-values themselves. All λ-values are below 0.5 which consequently means that there are a lot of droplets without any reactant molecule in the system. This effect results from the applied semi-batch operation and indicates that the reactants are quickly consumed by the particle formation mechanisms without a significant accumulation.

In Fig. 5.8 the time evolution of the number of particles N_P is given for all simulations concerning the experimental Set 1.

a)

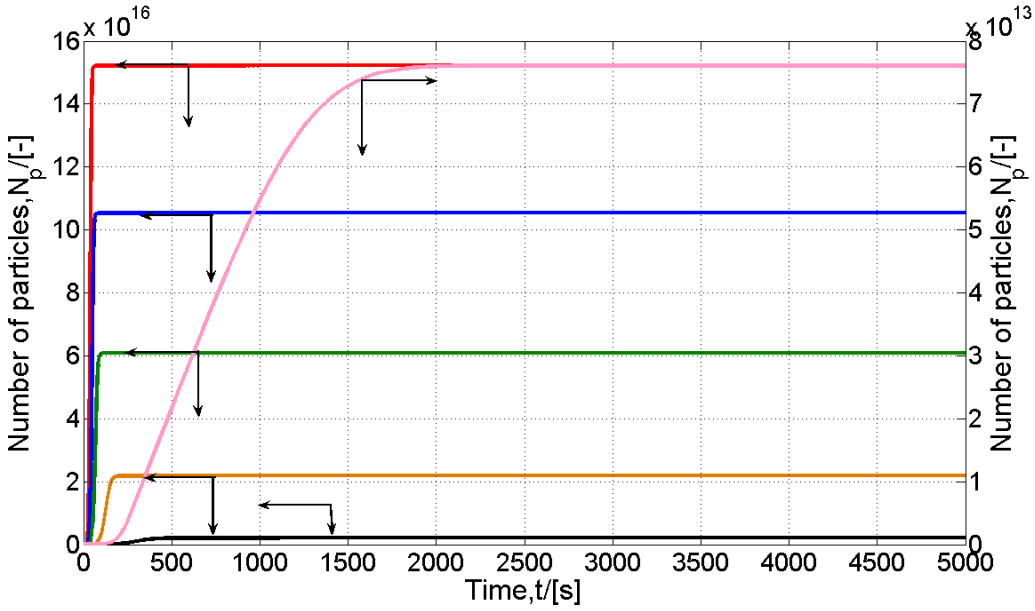

b)

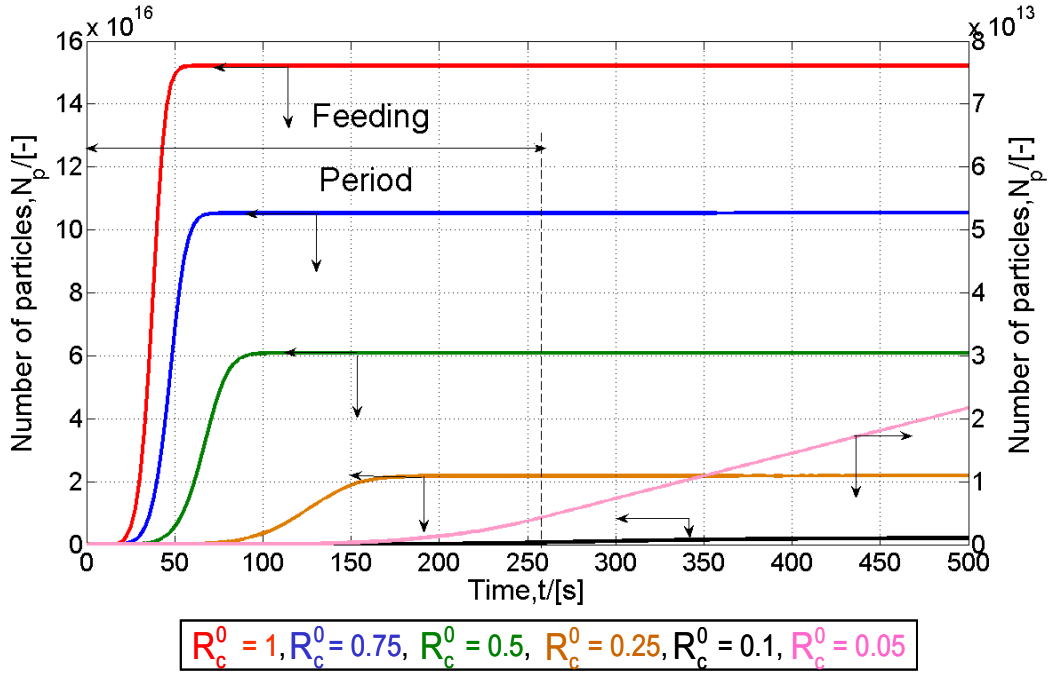

Fig. 5.8: a) Long-term dynamics of the number of particles N_p for different initial concentration ratios R_c^0 (Set 1). b) Short-term dynamics of the number of particles N_P for different initial concentration ratios R_c^0 (Set 1).

The number of particles N_P is considered for this analysis because it reflects the qualitative nucleation dynamics. Additionally, the number of particles can be correlated with the mean particle diameter if a complete consumption of the product C is assumed. The general observable behaviour validates the trends already observed for the dynamics of λ. After a short period in the beginning, where no particles are present in the system, the number of particles is increasing to the steady state value. The short period without particle formation in the beginning results from the necessary accumulation of dissolved $BaSO_4$ to reach N_{crit}. The period with an increasing number of particles corresponds to the time range where the nucleation of particles occurs. This range is short for high R_c^0-values and long for low R_c^0-values, which corresponds to the fast and slow dynamics of λ as depicted in Fig. 5.7. But the comparison of Fig. 5.7 and Fig. 5.8 shows as well a different dynamic behaviour of the nucleation mechanisms and the overall process dynamics. The nucleation of particles covers only a small part of the overall process dynamics at the beginning of the reactor operation. The dynamic behaviour after nucleation was stopped is only influenced by particle growth.

This behaviour is especially pronounced for the four highest R_c^0-values with the maximum of λ within the feeding period. For these values nucleation of particles stops shortly after the maximum and the rest of the dynamics is completely controlled by the growth kinetics. Taking figures 5.4, 5.7 and 5.8 into account the following rule can be determined:

$$\textit{Short nucleation period} \Rightarrow \textit{Fast dynamics} \Rightarrow \textit{High } R_c^0 \Rightarrow \textit{High } N_P \Rightarrow \textit{Small } d_{pm}.$$

This rule can be easily explained by the concentration of the reactants and therefore consequently the supersaturation. High R_c^0-values correspond to high concentrations and therefore to a high supersaturation. A high supersaturation leads to especially fast nucleation kinetics (order of N_{crit} compared to the order of 2 for growth) and thus a lot of particles N_P. If a complete consumption of C is assumed, smaller particles are formed when more particles are present (mass conservation).

The consumption rate of C due to nucleation $r_{nuc\text{-}cons}$ as a function of time is shown in Fig. 5.9 for the different initial concentration ratios R_c^0 of Set 1. The presented nucleation dynamics prove the results derived from the previous figure. A high R_c^0-value leads to fast dynamics with a high consumption rate of C and a low R_c^0-value leads to slower dynamics with a low consumption rate of C. Additionally, it can be shown that nucleation is the dominating particle formation mechanism at the beginning of the reactor operation and that especially the four highest R_c^0-values lead to very fast nucleation dynamics compared to the overall dynamics.

a)

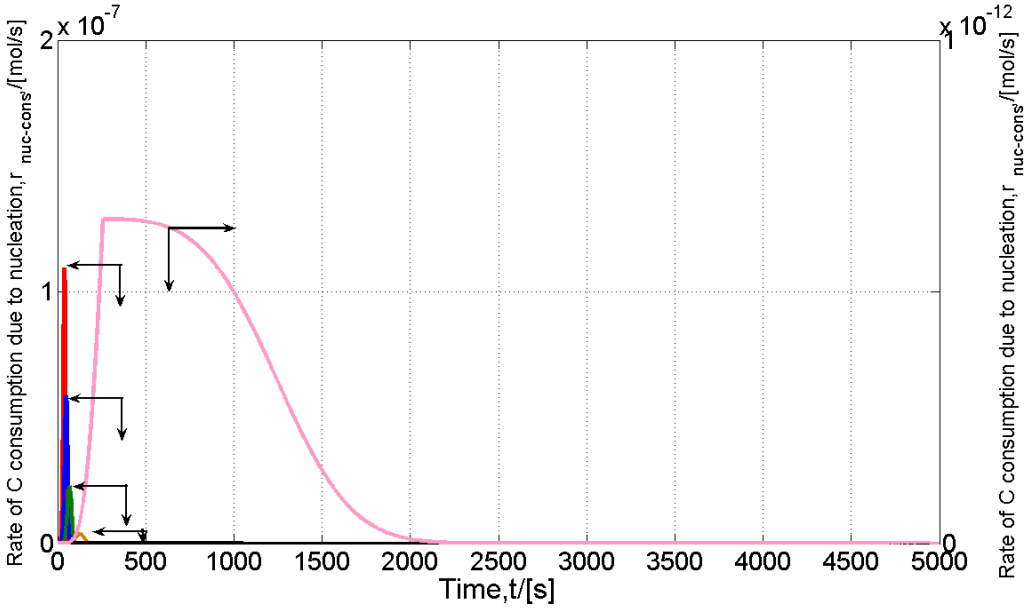

b)

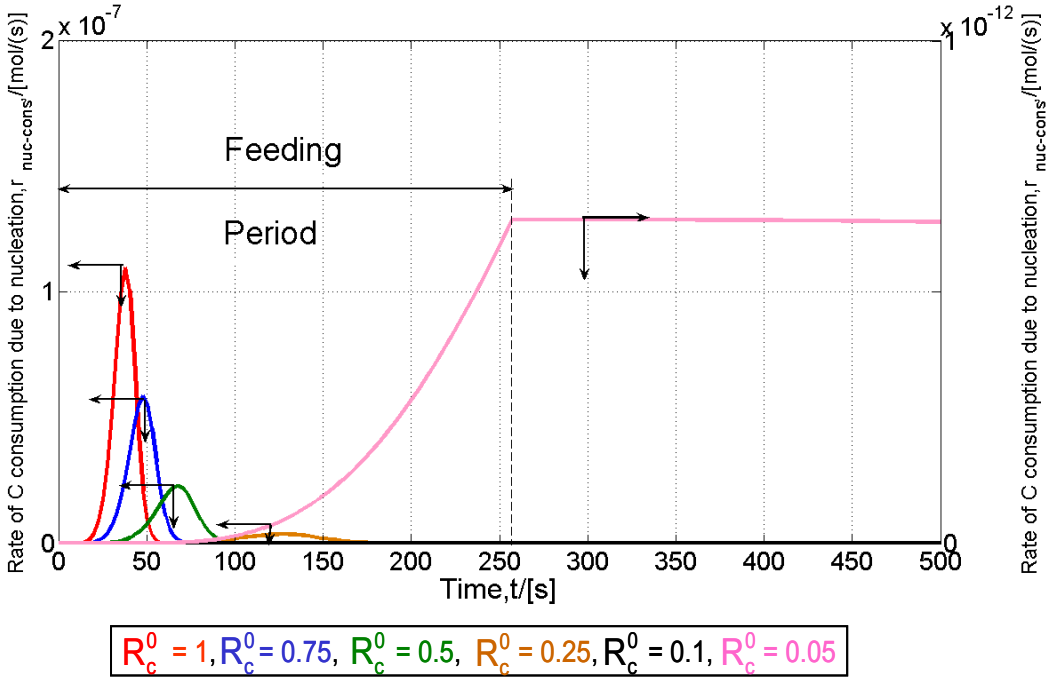

Fig. 5.9: a) Long-term dynamics of the consumption rate of C due to nucleation $r_{nuc\text{-}cons}$ for different initial concentration ratios R_c^0 (Set 1). b) Short term dynamics of the consumption rate of C due to nucleation $r_{nuc\text{-}cons}$ for different initial concentration ratios R_c^0 (Set 1).

To complete the analysis of the different population dynamic mechanisms the time evolution of the consumption rate of C due to growth r_g is presented in Fig. 5.10 for Set 1. In comparison to the nucleation kinetics, growth is present for the complete time range until the steady state is reached. Growth of particles starts after a considerable amount of nuclei are formed and is towards the end of the reactor operation.

a)

b)

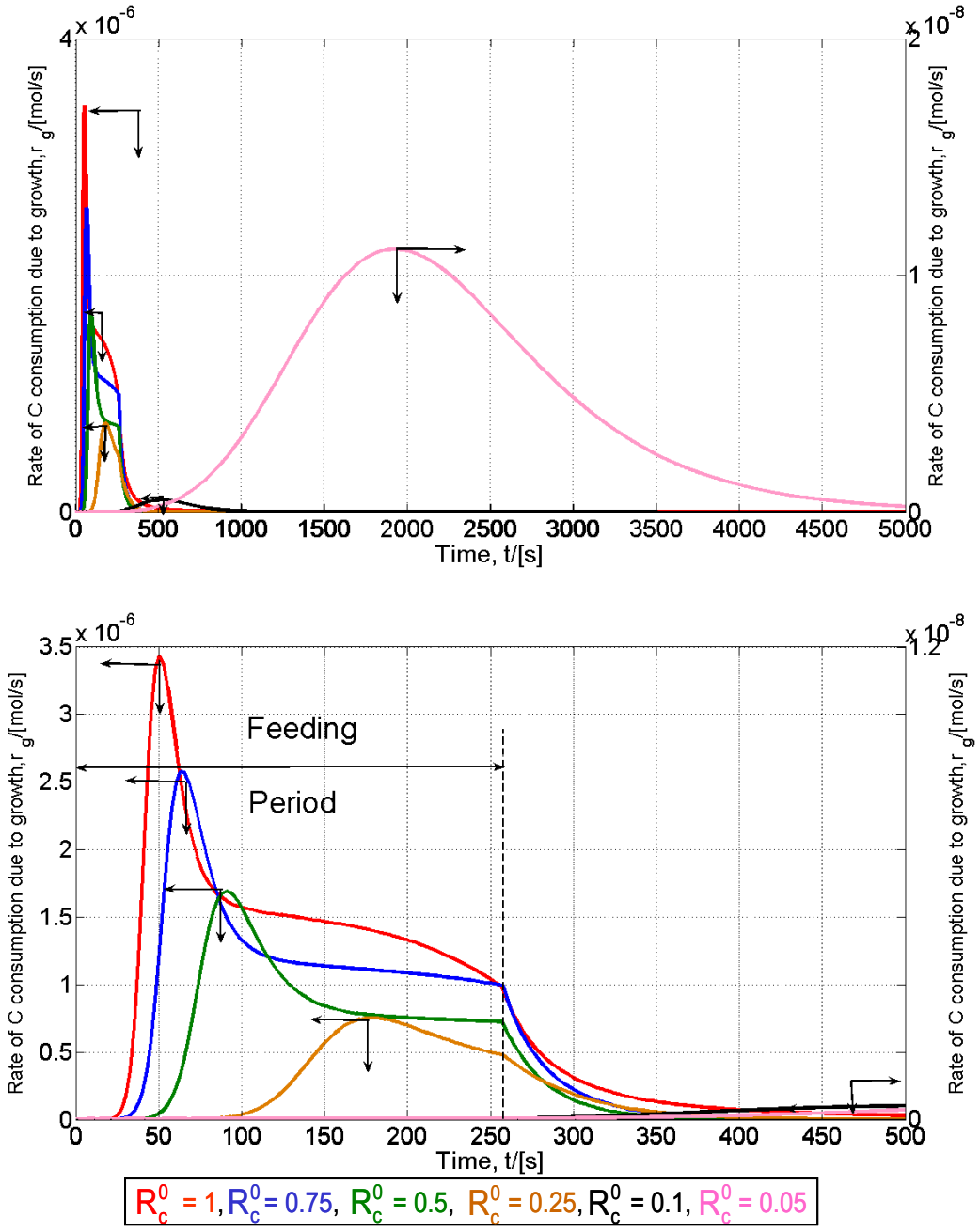

Fig. 5.10: a) Long-term dynamics of the consumption rate of C due to growth r_g for different initial concentration ratios R_c^0 (Set 1). b) Short-term dynamics of the consumption rate of C due to growth r_g for different initial concentration ratios R_c^0 (Set 1).

The maximum value of the consumption rate of C due to growth is observed shortly after the maximum in the nucleation kinetics. In contrast to the consumption of C due to nucleation, the consumption due to growth does not stop after the peak. While the amount of

C after the peak is not enough for nucleation (N_{crit} is not reached), the rest material will be consumed only by growth.

As already mentioned in the analysis of Fig. 5.8, the number of particles can be directly correlated with the mean particle diameter d_{pm} if a complete consumption of C is assumed. In Fig. 5.11, the mean particle diameter as function of time is presented. By comparison with Fig. 5.8, it can be concluded that small particle sizes are obtained for a large number of particles ($R_c^0 = 1$) and bigger particle sizes are obtained for lower numbers of particles (small R_c^0 values).

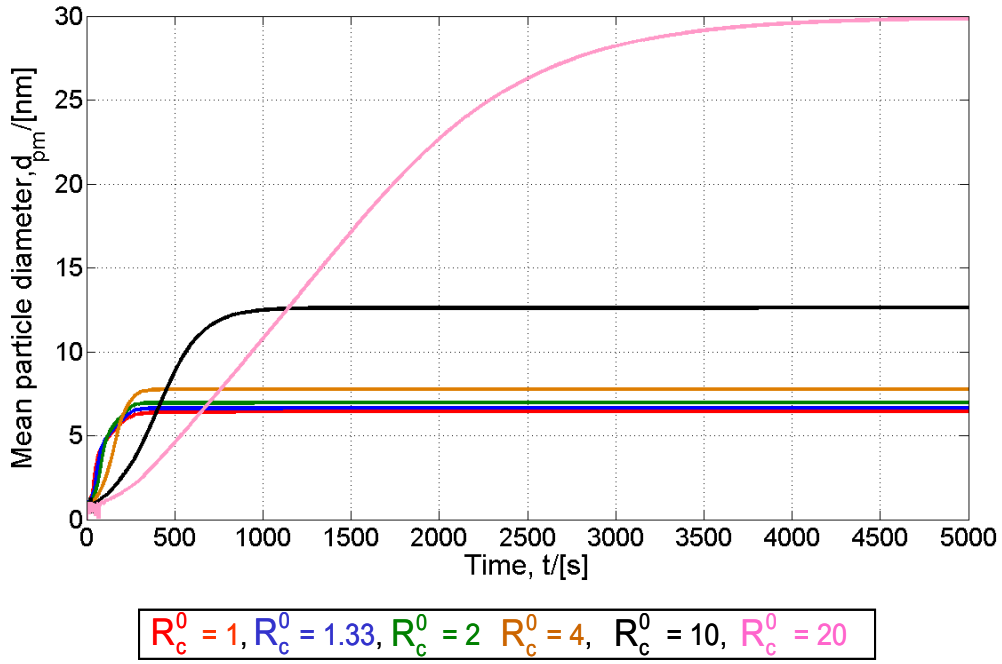

Fig. 5.11: Mean particle diameter d_{pm} as function of time for different initial concentration ratios R_c^0 (Set 1).

The results and conclusions from Set 1 are similar to the results obtained from the simulations of Set 2. Therefore, only two representative figures are shown for Set 2. Fig. 5.12 shows the time evolution of the average droplet occupancy λ and Fig.5.13 shows the mean particle diameter as a function of time. Note that the concentration of K_2SO_4 in Set 2 is smaller than for Set 1. Thus, higher R_c^0-values correspond to the non-stoichiometric conditions, while the smallest R_c^0-value ($R_c^0 = 1$) equals to the use of the two reactants in stoichiometric amounts.

The main difference between the curves for λ is visible in the discontinuities of the gradients within the feeding period for high R_c^0-values of Set 2. Simulations of Set 1 only show discontinuities exactly at the end of the feeding period. These discontinuities result from the applied instantaneous chemical reaction, because the concentration inside the droplets of the feed is higher than the concentration of the droplets within the reactor and the complete amount of K_2SO_4 (initially in the droplets within the reactor) is converted into the product C by the chemical reaction before the end of the feeding period. With a decrease of the initial concentration ratio inside the droplets of the reactor (increase of R_c^0 values), the discontinuity can be observed at an earlier time (less product C can be formed).

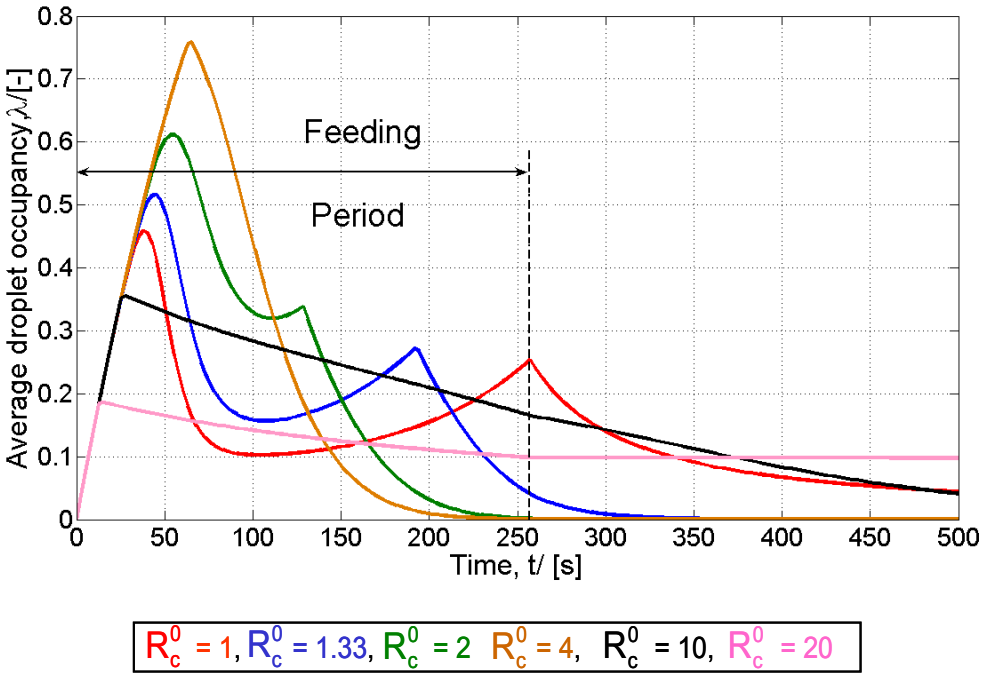

Fig. 5.12: Short-term dynamics of the average droplet occupancy λ for different initial concentration ratios R_c^0 (Set 2).

A second effect of the instantaneous chemical reaction on the results of Set 2 can be found in the values of λ at the first maximum. The four lowest R_c^0-values have an increasing λ-value with an increasing R_c^0-value, while the two highest R_c^0-values show the opposite behaviour due to the earlier consumption of K_2SO_4 (discontinuity). This effect explains the minimum value in the mean particles sizes for Set 2 observed in Fig. 5.5 and Fig. 5.12.

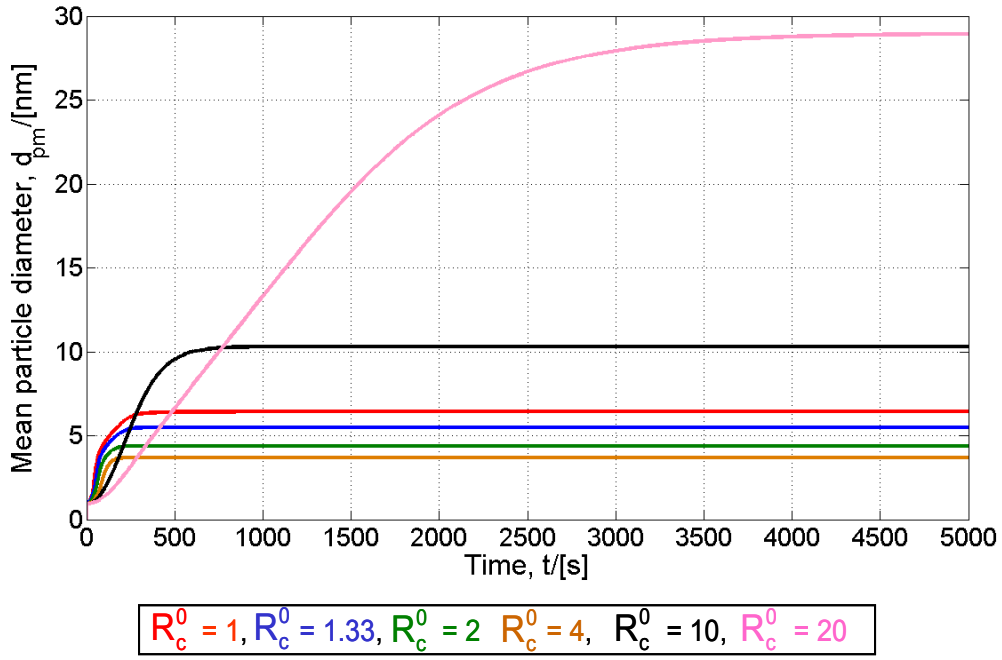

Fig. 5.13: Mean particle diameter d_{pm} as function of time for different initial concentration ratios R_c^0 (Set 2).

With the high λ-value at the maximum a lot of nuclei are formed and therefore the number of particles is increasing with an increasing R_c^0-value. The formation of a high number of nuclei consumes so many C molecules that these nuclei can not grow to bigger particles and thus the particle size for the four lowest R_c^0-values is decreasing with an increasing R_c^0-value. Due to the low-λ value for the two highest R_c^0-values only a few nuclei are formed and these nuclei can then grow without the concurrence of a large amount of nuclei, which results in much bigger particles.

5.4 Predicted parametric sensitivities

Sensitivity studies have been carried out to investigate the reliability of the estimated parameters N_{crit}, $k_{n,me}$ and $k_{g,me}$ as well as the influence of the droplet diameter d_{drop} on the resulting mean particle diameter. The latter parameter has been chosen because of possible errors in the experimental estimation of this parameter.

5.4.1 Critical number of molecules needed to form a stable nucleus

Simulations in the previous chapter 5.3 are carried out with a constant value of $N_{crit} = 5$, because the best fit of the experimental data is obtained with this value. However, N_{crit}-values for microemulsion precipitation reported in the literature are in the range between 2 and 8 [Niemann et al., 2006]. $N_{crit} < 2$ is implausible because this is equivalent to one molecule. A value of $N_{crit} > 8$ is difficult to realize due to the very high supersaturation level in such a droplet. Therefore, for the sensitivity study N_{crit} values of 2, 4, 5, 6, 7, and 8 molecules per droplet will be used in the simulation. All other parameters were fixed: the initial concentration ratio $R_c^0 = 1$, the nucleation rate constant $k_{n,me} = 7.59x10^{29}(-)/(ls)(l^5/mol^5)$, the growth rate constant $k_{g,me} = 1.35x10^2(nm/s)(l^2/mol^2)$, and the droplet size $d_{drop} = 5$ nm.

In Fig. 5.14 the mean particle diameter d_{pm} as a function of the critical molecule number for nucleation is shown. It can be seen that an increase of N_{crit} leads to the formation of bigger particles if all other parameters are kept constant. This behaviour could be expected because an increase of N_{crit} limits the number of droplets which are able to form a nucleus. If fewer particles are formed with a constant amount of available reactant the resulting particles must consequently be of a bigger size.

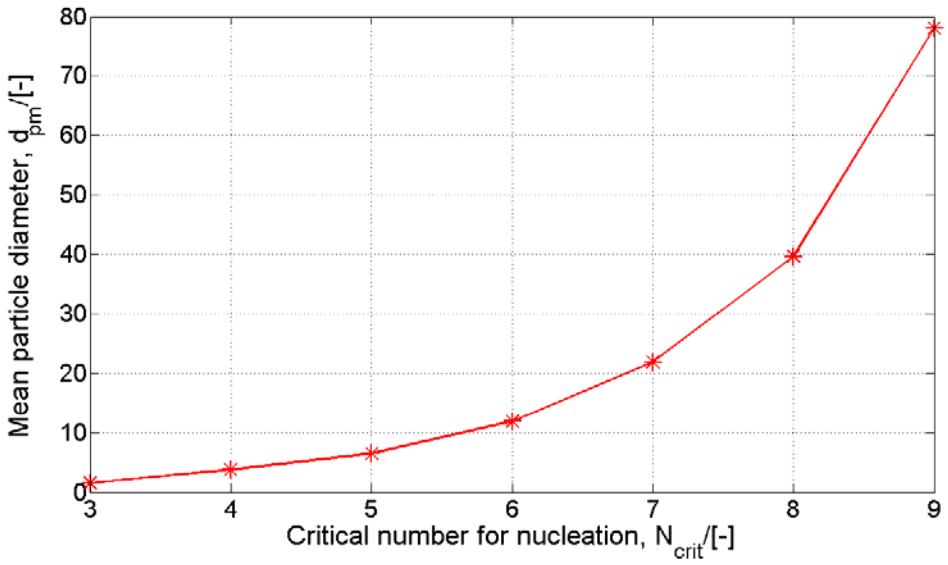

Fig. 5.14: Mean particle diameter d_{pm} at different N_{crit}.

5.4.2 Kinetic constants

The sensitivity studies of the kinetic constants were performed separately. For the analysis of the nucleation rate constant (see Fig. 5.15) the following parameters were kept

constant: the initial concentration ratio R_c^0 = 1, the growth rate constant $k_{g,me}$ = 1.35x10^2(nm/s)(l^2/mol^2), and the droplet size d_{drop} = 5 nm. For the analysis of the growth rate constant (see Fig. 5.16) is performed with the following set of constant parameters: the initial concentration ratio R_c^0 = 1, the nucleation rate constant $k_{n,me}$ = 7.59x10^{29}(-)/(ls)(l^5/mol^5), and the droplet size d_{drop} = 5 nm.

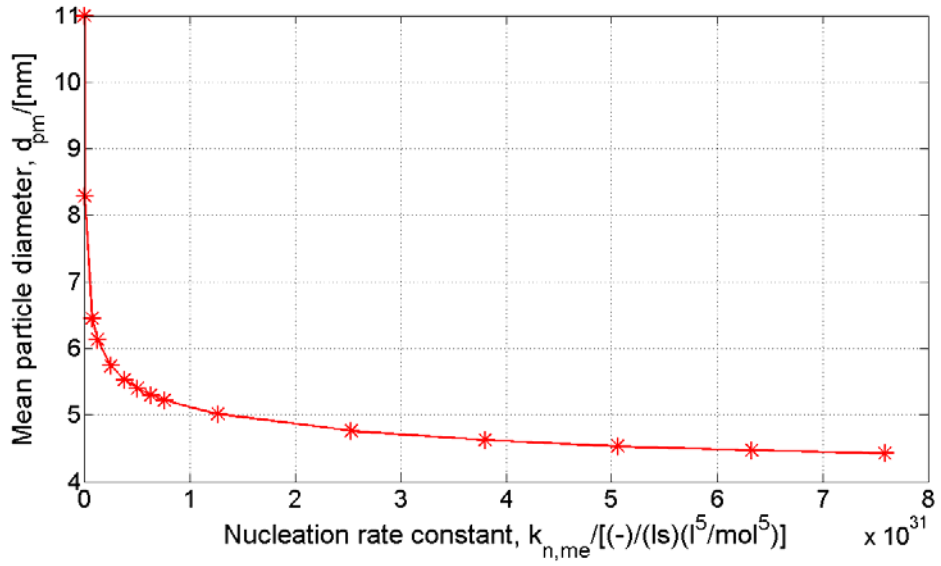

Fig. 5.15: Mean particle diameter d_{pm} for different nucleation rate constant $k_{n,me}$.

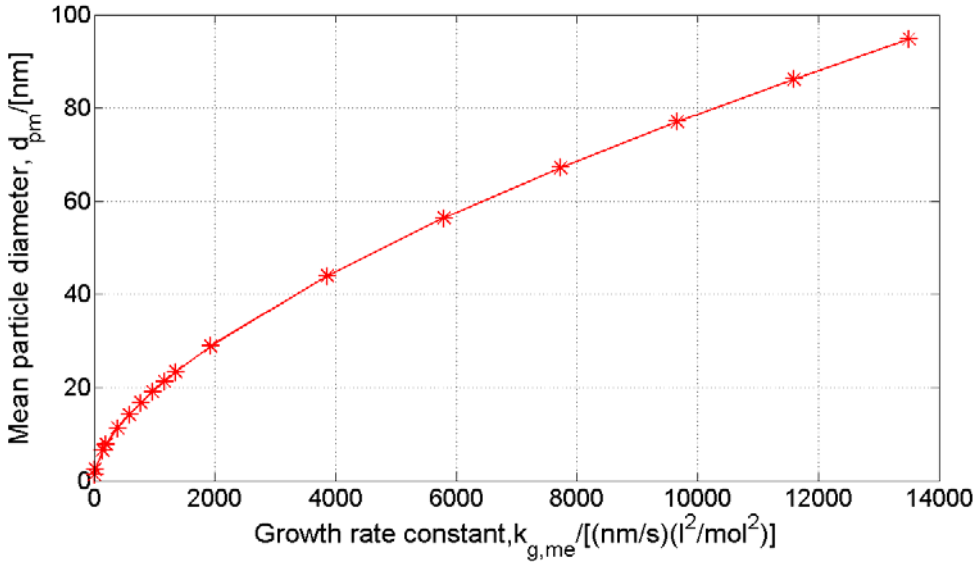

Fig. 5.16: Mean particle diameter d_{pm} for different growth rate constant $k_{g,me}$.

Both figures 5.15 and 5.16 show as well an expected behaviour. An increase of the nucleation rate constant leads to the formation of more nuclei and therefore at the end smaller particles are obtained, while an increase of the growth rate leads to an increasing mean particle diameter.

5.4.3 Droplet size

As one of the major physical properties of a microemulsions system, the droplet size plays an important role because it determines the size and the amount of available "nanoreactors" for the precipitation reaction. The used droplet diameter for the simulations (5 nm) is chosen based on the experimental data and results in a total number of 1.25×10^{20} droplets in 300 ml microemulsion (see chapter 4). For the present sensitivity study, droplet sizes of 3 – 8 nm are investigated resulting in droplet numbers between 5.8×10^{20} and 3.06×10^{19}, respectively. The following parameters are kept constant for this simulation study: the initial concentration ratio $R_c^0 = 1$, the nucleation rate constant $k_{n,me} = 7.59 \times 10^{29}$[(-)/(ls)(l^5/mol^5)], the growth rate constant $k_{g,me} = 1.35 \times 10^2$[(nm/s)(l^2/mol^2)], and $N_{crit} = 5$.

Fig. 5.17 shows the results of the sensitivity study with respect to the droplet size. If a lot of droplets are present in the system (small droplet size) bigger particles are obtained and for fewer droplets (bigger droplets) smaller particles are obtained. This result can be explained by the droplet occupancy with the dissolved product C. A low occupancy and therefore lower nucleation rates are realized in smaller droplets. A low nucleation rate leads to the formation of only a few nuclei, which can grow to big particles. Correspondingly, a high occupancy in bigger droplets leads to the formation of a high number of nuclei and therefore only small particles at the end of the process.

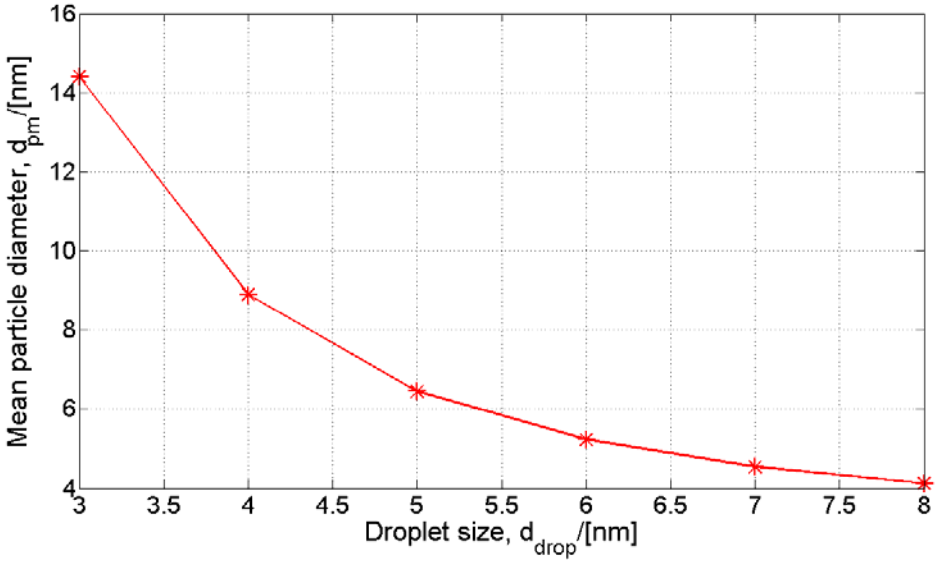

Fig. 5.17: Mean particle diameter d_{pm} for different droplet sizes d_{drop}.

Chapter 6

Conclusions

The controlled and scalable production of nanoparticles in large quantities is an actively pursued field of research due to numerous emerging applications and the intriguing possibilities of such products. In this work the investigation of a new and alternative process for the production of nanoparticles with tailor-made properties on a technical scale, the microemulsion-based precipitation synthesis is presented. The microemulsion precipitation process was carried out for the example of barium sulphate precipitation and contrasted with the same but bulk phase reaction under similar process design conditions in a stirred tank reactor.

Precipitation reactions are widely used in particle technology, but as has been shown also here in this work (chapter 4.2), the bulk phase precipitation in stirred tank reactors usually leads to particles on the micrometer scale with a broad size distribution. A number of process conditions and physical mechanisms like macro- and micromixing effects, particle agglomeration, and particle breakage limit the application for nanomaterial production. These deficits in the production technology may be overcome with the investigated microemulsion precipitation approach presented in this work.

The focus of this investigation is the applicability of the microemulsion precipitation approach on a technical scale. Therefore, the materials selected had to be easily accessible, handable and reasonably priced. The production process should be well-established and relatively easy to control with regular equipment which is already used in industry on a daily basis. Nevertheless the process should be implemented so that a number of process parameters are applicable to control the particulate product in a desired way.

Keeping these conditions and limitations in mind a particular process was chosen in order to carry out a number of important investigations for a technical process of producing tailor-made nanoparticles. The barium sulphate precipitation has been chosen as the example reaction as this system is well-known from bulk phase reaction processes, the crystal morphology of the solid is unique and the precipitated nanoparticles might be of interest in a number of applications. The microemulsion system consists of cyclohexane, water and the non-ionic surfactant MarlipalO13/40 (Sasol GmbH, Marl) as all materials are fullfilling the aformentioned requirements of acessibility, handling and price. The process has been carried

out in a regular stirred tank with a Rushton turbine, similar to equipment used nowadays for other particle production processes.

In order to carry out the investigations on the microemulsion precipitation the microemulsion, it has to be characterized and suitable operating conditions have to be selected (see chapter 4.1). As the most important part of my work, a number of variations of process parameters such as the stirring rate ω, the feeding rate Q_f, the feeding sequence, and the initial concentration ratio R_c^0 were varied in order to investigate their influence on the particle size, size distribution, and particle shape. A change of the initial concentration ratio of the two reactants ($BaCl_2$ and K_2SO_4) resulted in a significant change of the particle size. Therefore, the focus was on this particular operating parameter. With this parameter, the particle size of $BaSO_4$ nanoparticles could be adjusted in the range between 5 nm and 35 nm. Concerning the shape of the particles, it is observed that smaller particles have a more spherical shape, whereas larger particles have a cubic shape.

A corresponding mathematical model was developed to analyse the complex interaction between the different involved population mechanisms like fusion and fission of droplets, chemical reaction, and nucleation and growth of particles during microemulsion precipitation. The combination of mass balances and kinetic approaches for particles results in a reduced mathematical model which can be solved numerically in a few seconds only. The major outcome of the model simulation is the temporal evolution of the mean particle diameter for different initial ratios R_c^0. A good qualitative agreement between the experimental data and the simulation results was achieved after optimisation of the model parameters.

In the future, further work is to transfer experimental and simulation results based on this work into a technical-scale process. The feeding rate Q_f could be another potential control parameter for the particle size and should be analysed in detail. An efficient method for particles extraction and recycling of the continuous phase in a “closed system” should be a further target for this technology with regard to industrial application purposes.

References

Abu-Daabes, M.A., Pinto, N.G. (2005). Synthesis and characterization of a nano-structured sorbent for the direct removal of mercury vapor from flue gases by chelation, *Chemical Engineering Science,* 60(7), 1901-1910.

Adityawarman, D., Voigt, A., Veit, P., Sundmacher, K. (2005). Precipitation of $BaSO_4$ nanoparticles in non-ionic microemulsions, *Chemical Engineering Science*, 60, 3373-3381.

Aikens, P.A., Friberg, S.E. (1999). Microemulsions in cosmetics, in: Kumar., P. (Ed.), *Handbook of Microemulsion Science and Technology,* Marcel Dekker Inc, New York.

Allen, T. (1999). Particle size measurement : powder sampling and particle size measurement, Chapman and Hall, London.

Aoun, M., Plasari, E., David, R., Villermaux, J. (1996). Are Barium Sulphate kinetics sufficiently known for testing precipitation reactor models? *Chemical Engineering Science,* 51(10), 2449-2458.

Arriagada, F.J., Osseo-Asare, K. (1999). Synthesis of nanosize silica in a non-ionic water-in-oil microemulsion, *Journal of Colloid and Interface Science,* 211, 210-220.

Atik, S.S., Thomas, J., K. (1981). Transport of photoproduced ions in water in oil microemulsions: movements of ions from one water pool to another, *Journal of American Chemical Society*, 103, 3543-3550.

Ayyup, P., Multani, M., Barma, M., Palkar., V.R., Vijayaraghavan, R. (1988). Size-induced structural phase transitions and hyperfine properties of microcrystalline Fe_2O_3, *Journal of Physics C: Solid State Physics*, 21, 2229-2245.

Bagwe, R.P., Khilar, K.C. (2000). Effects of intermicellar exchange rate on the formation of silver nanoparticles in reverse microemulsions of AOT, *Langmuir,* 16(3), 905-910.

Baldyga, J., Podgorska, W., Pohorecki, R. (1995). Mixing-precipitation model with application to double feed semibatch precipitation, *Chemical Engineering Science*, 50, 1281-1300.

Bandyopadhyaya, R., Kumar, R., Gandhi, K.S., Ramkrishna, D. (1997). Modeling of precipitation in reverse micellar systems, *Langmuir*, 13(14), 3610-3620.

Bandyopadhyaya, R., Kumar, R., Gandhi, K.S. (2001). Modelling of $CaCO_3$ nanoparticle formation during over basin of lubricating oil additives, *Langmuir*, 17(4), 1015-1029.

Bandyopadhyaya, R. (2000). *Modelling of precipitation in reverse micelles*, Ph.D. Thesis, Indian Institute of Science, Bangalore.

Boakye, E., Radovic, L. R., Osseo-Asare, K. (1994). Microemulsion-mediated synthesis of nanosize molybdenum sulfide particles, *Journal of Colloid and Interface Science,* 163 (1), 120-129.

Boutonnet, M., Kizling, J., Stenius, P. (1982). The preparation of monodisperse colloidal metal particles from microemulsions, *Colloids Surface,* 5 (3), 209-225.

Brookhaven, (2004).Theory of dynamic light scattering, http:/www.bic.com/DLSbasics.html.

Burban, H., He, M., Cussler, E.L. (1995). Organic microporous materials made by bicontinuous microemulsion polymerization, *AIChE Journal*, 41, 907-914.

Candau, F. (1999). Polymerization in microemulsions, in: Kumar, P. (Ed.), *Handbook of Microemulsion Science and Technology,* Marcel Dekker Inc, New York.

Castro, T., Reifenberger, R., Choi, E., Andres, R, P. (1990). Size dependent melting temperature of individual nanometer-sized metallic clusters, *Physical Review B,* 13, 8548-8553.

Charles Cao, Y., Jin, Rongchao., C, Thaxton, Shad., Mirkin, Chad A. (2005). A two-color-change nanoparticle-based method for DNA detection, *Talanta,* 67(3), 449-455.

Chen, G., Luo,G., Xu, J., Wang. (2005). Preparation of barium sulfate particles using filtration dispersion precipitation method in O/W system, *Powder Technology,* 153(2), 90-94.

Chioui, H., Li, L., Hu, T., Chan, H., Chen, J., Yun, J. (2006). Production of salbutamol sulfate for inhalation by high-gravity controlled antisolvent precipitation**,** *International Journal of Pharmaceutics*, In Press.

Chhabra, V., Free, M., L., Kang, P.K., Truesdail, S.E., Shah, D.O. (1997). Microemulsion as an emerging technology, *Tenside: Surfactants Detergents*, 34, 156-168.

Chang, C., Fogler, H.S. (1996). Kinetics of silica particle formation in non-ionic w/o microemulsions from TEOS, *AIChE Journal*, 42, 3153-3163.

Chen, H., Chang, H. (2005). Synthesis of nanocrystalline cerium oxide particles by the precipitation method, *Ceramics International*, 31(6), 795-802.

Chern, C. S., Tang, H. J. (2003). Particle nucleation and growth mechanisms in styrene microemulsion polymerisation, *Polymer Reaction Engineering,* 11(3), 213-232.

Debuigne, F., Cuisenaire, J., Jeunieau, L., Masereel, B., Nagy, J. B. (2001). Synthesis of limesulfide nanoparticles in the microemulsion epikuron/isopropyl 46 myristate/water/n-butanol (or isopropanol). *Journal of Colloid and Interface Science,* 243 (1), 90-101.

Dirksen, J.A., Ring, T.A. (1991). Fundamentals of crystallization: kinetic effects on particle size distributions and morphology, *Chemical Engineering Science,* 46(10), 2389-2427.

Ding, S., Wang, M. (2006). Studies on synthesis and mechanism of nano-$CaZn_2(PO_4)_2$ by chemical precipitation*, Dyes and Pigments*, In Press.

Dutta, P.K., Robbins, D. (1989). Novel routes of zeolite synthesis, *Proceedings of the Symposium on New Catalytic Materials and Techniques,* September 10-15, Miami, USA.

Engström, S., Larsson, K. (1999). Microemulsions in foods, in: Kumar., P (Ed.), *Handbook of Microemulsion Science and Technology,* Marcel Dekker Inc, New York.

Espiard, P., Guyot, A., Mark, J.E. (1995). Surface functionalized colloidal silica particles from inverse microemulsion sol gel process, *Journal of Inorganic and Organometallic Polymers*, 5(4), 391-407.

Esquena, J., Tadros, T.F., Kostarelos, K., Solans, C. (1997). Preparation of narrow size distribution silica particles using microemulsions, *Langmuir,* 13 (24), 6400-6406.

Fitchett, D.E., Tarbell, J.M. (1990). Effect of mixing on the precipitation of barium sulfate in a MSMPR reactor, *AIChE Journal*, 36, 511-512.

Fletcher, P.D. I., Howe, A.M., Robinson, B. H. (1987). The kinetics of solubilisate exchange between water droplets of water in oil microemulsion, *Journal of the Chemical Society Faraday Transactions*, 83(4), 985-1006.

Gerstlauer, A., Motz, S., Mitrovic, A., Gilles, E.D. (2002). Development, analysis and validation of population models for continuous and batch crystallizers, *Chemical Engineering Science*, 57(20), 4311-4327.

Herrero-Vanrell, R., Rincón, A.C., Alonso, M., Reboto, V., Molina-Martinez, I.T., Rodríguez-Cabello, J.C. (2005). Self-assembled particles of an elastin-like polymer as vehicles for controlled drug release, *Journal of Controlled Release,* 102(1), 113-122.

Hernandez, L.R. (2002). *Stochastische modellierung der nanopartikelbildung in mikroemulsionen*, Dissertation, Technische Universität Berlin.

Hingorani, S., Pillai, V., Kumar, P. Multani, M.S., Shah, D.O. (1993). Microemulsion mediated synthesis of zinc-oxide nanoparticles for varistor studies, *Materials Research Bulletin,* 28(12), 1303-1310.

Hintz, W., Jordanova, V., Nikolov, T., Tomas, J. (2003). Sol - gel - synthese zur herstellung nanoskaliger partikel aus titan(IV) - oxid - Reaktionskinetische Untersuchungen der Peptisationsreaktion, *Chemie Ingenieur Technik*, 75,1132.

Hirai, H., Sato, H., Komasawa, I. (1993). Mechanism of formation of titanium dioxide ultrafine particles in reverse micelles by hydrolysis of titanium tetrabutoxide, *Industrial and Engineering Chemical Research,* 32 (12), 3014-3019.

Hirai, T. Sato, H. Komasawa, I. (1994). Mechanism of formation of CdS and ZnS ultrafine particles in reverse micelles, *Industrial and Engineering and Chemical Research,* 33 (12), 3262-3266.

Hopwood, J.D., Mann, S. (1997). Synthesis of barium sulfate nanoparticles and nanofilaments in reverse micelles and microemulsions**,** *Chemical Material,* 9(8), 1819-1828.

Holmberg, K., Jonsson, B., Kronberg, B., Lindman, B. (2003). *Surfactants and Polymers in Aqueuous Solution*, Wiley and Sons, New York.

Hopwood, J.D., Mann, S. (1997). Synthesis of barium sulphate nanoparticles and nanofilaments in reverse micelles and microemulsions, *Chemistry Materials*, 9, 1819-1828.

Ingelsten, H.H., Bagwe, R.P., Palmqvist, A., Skoglundh, M., Svanberg, C., Holmberg, K., O-. Shah, D. (2001)**.** Kinetics of the formation of nano-sized platinum particles in water-in-oil microemulsions, *Journal of Colloid and Interface Science,* 241(1), 104-111.

Inouye, K., Endo, R., Otsuka, Y., Miyashiro, K., Kaneko, K., Ishikawa, T. (1982). Oxygenation of ferrous ions in reversed micelle and reversed microemulsion, *Journal of Physical Chemistry*, 86, 1465–1469.

Ivanova, N.I., Rudelev, D.S., Summ, B.D., Chalykh, A.A. (2001). Synthesis of barium sulphate nanoparticles in water-in-oil microemulsion system, *Colloid Journal,* 63, 714-717.

Jain, R., Mehra, A. (2004). Monte-Carlo models for nanoparticle formation in two microemulsion systems, *Langmuir*, 20 (15), 6507-6513.

Kahlweit, M., Strey, R., Busse, G. (1990). Microemulsions: a qualitative thermodynamic approach, *Journal of Physical Chemistry,* 94, 3881-3894.

Kandori, K., Konno, K., Kitahara, K. (1988). Preparation of $BaCO_3$ particles in ionic w/o microemulsion, *Journal Dispersion Science and Technology,* 9(1), 61-73.

Kandori, K., Shizuka, N., Konno, K., Kitahara, A. (1987). Preparation of $CaCO_3$ particles in water pool in non-aqueous non-ionic surfactant solutions, *Journal of Dispersion Science and Technology,* 8(5-6), 477-491.

Karanikolos, G.N., Alexandridis, P., Mountziaris, T.J. (2003). Synthesis and size control of luminescent II-VI semiconductor nanocrystals by a novel microemulsion-gas contacting

technique in: *AIChE Annual Meeting 2003*, Omnipress, and San Francisco, California, USA.

Kashchiev, D., Van Rosmalen, G.M. (2003). Nucleation in solutions revisited, *Crystal Research Technology,* 7-8, 555-574.

Kelsall, R., Hamley, I., Geoghegan, M. (2005). *Nanoscale Science and Technology*, Wiley and Sons, Weinheim.

Kemmer, F.N. (Ed.)(1988). NALCO Water Handbook, 2nd edition, McGraw-Hill, New-York.

Klabunde, K.J. (Ed.) (2001). *Nanoscale Materials in Chemistry*, Wiley and Sons, New York.

Köhler, M., Fritzsche, W. (2004). *Nanotechnology: an introduction to nanostructuring techniques*, Wiley-VCH, Weinheim.

Kurihara, K., Kizling, J., Stenius,P., Fendler, J.H. (1983). Laser and pulse radiolytically induced colloidal gold formation in water-in-oil microemulsions, *Journal of American Chemical Society*, 105, 2574-2579.

Kumar, A.R., Hota, G., Mehra, A., Khilar, K.C. (2004). Modeling of nanoparticles formation by mixing of two reactive microemulsions*, AIChE Journal*, 50(7), 1556-1567.

Kraume, M. (2003). *Mischen und Rühren : Grundlagen und moderne Verfahren*,Wiley-VCH, Weinheim.

Kruis, F. E., Goossens, A., Fissan, H. (1996). Synthesis of semiconducting nanoparticles, *Journal of Aerosol Science,* 27(1), 165-166.

Lade, M., Mays, H., Schmidt J., Willumeit, R., Schomäcker, R. (2000). On the nanoparticle synthesis in microemulsions: detailed characterization of an applied reaction mixture, *Colloids Surfaces A: Physicochemical and Engineering Aspect,* 163, 3-15.

Lamer, V., Dinegar, R.H. (1950). Theory, production, and mechanism of formation of monodispersed hydrosols, *Journal of the American Chemical Society*, 72 (11), 4847-4854.

Lee, D.W., Yu, J.H., Jang, T.S., Kim, B.K. (2005). Nanocrystalline iron particles synthesized by chemical vapor condensation without chilling, *Materials Letters,* 59(17), 2124-2127.

Lianos, P., Thomas, J.K. (1987). Small CdS particles in inverted micelles, *Journal of Colloid and Interface Science,* 117(2), 505-512.

Liz, L., Quintela, M.A., Mira, J., Rivas, J. (1994). Preparation of colloidal Fe_3O_4 ultrafine particles in microemulsions, *Journal of Materials Science*, 29, 3797-3801.

Li, G.L., Wang, G.H. (1999). Synthesis of nanometer-sized TiO_2 particles by a microemulsion method, *Nanostrucured Materials,* 11(5), 663-668.

Li, M., Mann, S. (2000). Emergence of morphological complexity in $BaSO_4$ fibers synthesized in AOT microemulsions**,** *Langmuir,* 16(17), 7088-7094.

Li, Y.C., Park, C.W. (1999). Particle size distribution in the synthesis of nanoparticles using microemulsions*, Langmuir*, 15(4), 952-956.

Lindberg, M., Rasmusson, A.C. (2000). Supersaturation generation at the feed point in reaction crystallization of a molecular compound, *Chemical Engineering Science,* 55, 1735-1746.

Malmstein, M. (1999). Microemulsions in pharmaceuticals in: Kumar, P. (Ed.), *Handbook of Microemulsion Science and Technology,* Marcel Dekker Inc, New York.

Moulik, S.P., Paul, B.K. (1998). Structure, dynamics, and transport properties of microemulsions, *Advances in Colloid and Interface Science*, 78(2), 99-195.

Monnoyer, P., Fonseca, A., Nagy, J. B. (1995). Preparation of colloidal AgBr particles from microemulsions, *Colloids and Surfaces A: Physicochemical Engineering Aspects,* 100, 233-243.

Motte, L., Billoudet, F., Pileni, M.P. (1996). Synthesis in situ of nanosize silver sulphide semiconductor particles in reverse micelles, *Journal of Material Science*, 31(1), 38-42.

Mullin, J. W. (2004). Crystallization and Precipitation, in: *Ullmann's Processes and Engineering*, Vol.2.1, Wiley-VCH, Weinheim.

Myerson, A.S. (1993). *Handbook of Industrial Crytallization*, Butterworth-Heinemann, Boston.

Nagy, J.B. (1999). Preparation of ultrafine particles of metals and metal borides in microemulsions, in: Kumar, P. (Ed.), *Handbook of Microemulsion Science and Technology,* Marcel Dekker Inc, New York.

Nagy, J.B. (1989). Multinuclear NMR characterization of microemulsions-preparation of monodisperse colloidal metal boride particles, *Colloid and Surfaces*, 35(2-4), 201-220.

Nanni, A., Dei, L. (2003). $Ca(OH)_2$ nanoparticles from w/o microemulsions, *Langmuir*, 19, 933-938.

Natarajan, U., Handique, K., Mehra, A., Bellare, J.R., Khilar, K.C. (1996). Ultrafine metal particle formation in reverse micellar systems: effects of intermicellar exchange on the formation of particles, *Langmuir,* 12 (11), 2670-2678.

Nyvlt, J., Söhnel O., Matuchová, M., Broul, M. (1985). *The Kinetics of Industrial Crystallization*, Elsevier, New York.

Niemann, B., Rauscher, F., Adityawarman, D., Voigt, A., Sundmacher, K. (2006). Microemulsion assisted precipitation of particles: experimental and model based process analysis, *Chemical Engineering Processing*, 45(10), 917-935.

Olrich, B., Schomäcker, R. (2001). *Candida Rugosa* Lipase reactions in non-ionic w/o-microemulsion with a technical surfactant, *Enzyme and Microbial Technology,* 28, 42–48.

Osseo-Asare, K. (1999). Microemulsion-mediated synthesis of nanosize oxide materials, in: Kumar, P. (Ed.), *Handbook of Microemulsion Science and Technology,* Marcel Dekker Inc, New York.

Osseo-Asare, K., Arriagada, F.J. (1990). Synthesis of nanosize particles in reverse microemulsions in: *Proceeding of the Third International Conference on Powder Processing Science in San Diego*. ISBN 0-944904-28-9.

O'Sullivan, E.C., Ward, A.J.I., Budd, T. (1994). Obvious and non-obvious influences of surfactants on the formation of nanosized particles*, Langmuir*, 10, 2985-2992.

Peng, X., Luan, Z., Ding, J., Di, Z., Li,Y., Tian, B. (2005). Ceria nanoparticles supported on carbon nanotubes for the removal of arsenate from water, *Materials Letter,* 59(4), 399-403.

Petit, C., Lixon, P., Pileni, M. P. (1993). In-situ synthesis of silver nanocluster in AOT reverse micelles, *Journal of Physical Chemistry,* 97 (49), 12974-12983.

Pileni, M.P., Motte, L., Billoudet, F., Petit, C. (1996). Synthesized "in situ" in reverse micelles of silver-sulfide semiconductors, *Surface Review and Letters*, 3(1), 1215-1218.

Pillai, V., Kanicky, J.R., Shah, D.O. (1999). Applications of microemulsion in enhanced oil recovery in: Kumar, P. (Ed.), *Handbook of Microemulsion Science and Technology,* Marcel Dekker Inc, New York.

Qi, L., Ma, J., Cheng, H., Zhao, Z. (1996). Preparation of $BaSO_4$ nanoparticles in non-ionic w/o microemulsions, *Colloids and Surfaces A: Physicochemical and Engineering Aspects,* 108, 117-126.

Rao, C.N.R, Müller, A., Cheetham, A.K. (2004). Nanomaterials – An Introduction, in: Rao, C.N.R (Ed.), *The Chemistry of Nanomaterials: Synthesis, Properties and Applications,* Wiley-VCH, Weinheim.

Randolph, A. D., Larson M. A. (1988). *Theory of Particulate Processes,* 2nd edition, Academic Press, San Diego.

Rauscher, F., Veit, P., Sundmacher, K. (2005). Detailed analysis of a technical grade w/o-microemulsion and its application for the precipitation of calcium carbonate particles. *Colloid Colloids and Surfaces A: Physicochemical Engineering Aspects,* 254, 183–191.

Ravet, I., Nagy, J.B., Derouane, E.G. (1987). On the mechanism of formation of colloidal monodisperse metal boride particles from reversed micelles composed of CTAB- 1-hexanol – water, in: Delmon, B (Hrsg.); Grange,P (Hrsg) : *Preparation of catalyst IV, scientific bases for the preparation of heterogenuous catalyst*, Elsevier.

Sato, H., Ohtsu, T. Komasawa, I. (2002). Preparation of ultrafine palladium particles in reverse micelles and application for hydrogenation catalysts, *Journal Chemical Engineering Japan*, 35(3), 255-262.

Sato, H., Hirai, T., Komasawa, I. (1996). Mechanism of formation of silver halide ultrafine particles in reverse micellar systems*, Journal Chemical Engineering Japan*, 29(3), 501-507.

Sato, H., Komasawa, I. (1995). Mechanism of formation of composite CdS-ZnS ultrafine particles in reverse micelles, *Industrial and Engineering Chemical Research,* 34(7), 2493-2498.

Schmidt, J. (2000). *Kinetische Modellierung von Fällungsreaktionen in Mikroemulsionen und Mehrphasensystemen*, Dissertation, TU Berlin.

Schulman, J.H., Stoekenius, W., Prince, L.M. (1959). Mechanism of formation and structure of microemulsions by electron microscopy, *Journal of Physical Chemistry*, 63, 1677-1680.

Schubert, K.V., Kaler, E.W. (1996). Non-ionic microemulsions, *Berichte der Bunsen-Gesellschaft - Physical Chemistry,* 100 (3),190-205.

Schwuger, M.J., Stickdorn, K., Schomäcker, R. (1995) Microemulsions in technical processes, *Chemical Review,* 95, 849-864.

Sottmann, T., Strey, R. (1997). Ultralow interfacial tensions in water-n-alkane-surfactant systems, *Journal Chemical Physiscs*, 106 (20), 8606-8615.

Sottmann, T., Lade, M., Stolz, M. Schomäcker, R. (2002). Phase behaviour of non-ionic microemulsions prepared from technical grade surfactants, *Tenside Surfactants Detergents*, 39(1), 239-249.

Son, J.T. (2004). Novel electrode material for Li Ion battery based on polycrystalline $LiNbO_3$, *Electrochemistry Communications,* 6 (10), 990-994.

Stöger, M. (2000) Prinzipielles über das TEM, http/tem.atp.tuwien.ac.at/EELS/TEMbild.html.

Skandan, G., Chen, Y.J., Glumac, N., Kear, B.H. (1999). Synthesis of oxide nanoparticles in low-pressure flames, *Nanostructured Materials,* 11(2), 149-158.

Summers, M., Eastoe, J., Davis, S. (2002). Formation of $BaSO_4$ nanoparticles in microemulsions with polymerized surfactant shells, *Langmuir*, 18(12), 5023-5026.

Tavare, N.S. (1995). *Industrial Crystallization: Process Simulation and Design*, Plennum Press, New York.

Tadros, T.T. (2005). Applied Surfactants: Principles and Application*,* Wiley-VCH, Weinheim.

Tojo, C., Blanco, M.C., Lopez-Quintela, M.A. (1998). The influence of reactant excess and film flexibility on the mechanism of nanoparticle formation in microemulsions: a Monte-Carlo simulation, *Langmuir,* 14, 6835-6839.

Thomas, G., Goreinge, M.J. (1979). *Transmission Electron Microscopy of Materials*, Wiley and Sons, New York.

Thorpe, J. (2005). *Principles of Transmission Electron Microscopy*, http://www.lifesci.sussex.ac.uk/home/Julian_Thorpe/genem.htm.

Van-Leuween, M.L.J. (1998). *Precipitation and Mixing*, Dissertation, Delft Technical University.

Voigt, A., Adityawarman, D., Sundmacher, K. (2005). Size and distribution prediction for nanoparticles produced by microemulsion precipitation: a Monte-Carlo simulation study, *Nanotechnology*, 16, 429-434.

Wagner, K., Pratsinis, S. (2005). Gas-phase synthesis of nanoparticles: scale-up and design of flame reactors, *Powder Technology,* 150, 117-122.

Watzke, H.J., Dieschbourgh, C. (1994). Novel silica in colloid and interface science, *Advances in Colloid and Interface Science*, 50, 1-4.

Wong D.C.Y., Jaworski, Z., Nienow A.W. (2001). Effect of ion excess on particle size and morphology during barium sulphate precipitation: an experimental study, Chemical *Engineering Science,* 56, 727-734.

Wu, M. L., Chen, D. H., Huang, T. C. (2001). Preparation of Pd/Pt bimetallic nanoparticles in water/AOT/isooctane microemulsions. *Journal of Colloid and Interface Science,* 243 (1), 102-108.

Yang, H., Rongrong Shi, Z., Li, X., Dong, X., Yu, Y. (2005). Sol–gel synthesis of TiO_2 nanoparticles and photocatalytic degradation of methyl orange in aqueous TiO_2 suspensions**,** *Journal of Alloys and Compounds*, 413 (1-2), 302-306.

Yu, F., Wang, J.N., Sheng, Z.M., Su, L.F. (2005). Synthesis of carbon-encapsulated magnetic nanoparticles by spray pyrolysis of iron carbonyl and ethanol, *Carbon,* 43(14), 3018-3021.

Zhao, L., Steinhart, M., Yosef, M., Lee, S.K., Schlecht, S. (2005) Large-scale template-assisted growth of LiNbO3 one-dimensional nanostructures for nano-sensors, *Sensors and Actuators B*, 109(86), 86-90.

Zhou, J. Leuschner, C., Kumar, C., Hormes, J. Soboyejo, W.O. (2005). A TEM study of functionalized magnetic nanoparticles targeting breast cancer cells, *Materials Science and Engineering: C,* 8(14), 1451-1455.

Zheng, H., Huang, J., Wang, W., Ma, C. (2005). Preparation of nano-crystalline tungsten carbide thin film electrode and its electrocatalytic activity for Hydrogen evolution, *Electrochemistry Communications,* 7, 1045-1049.

Zlokarnik, M. (1972).Rührtechnik in *Ullmans Encyklopädie der Technischen Chemie*, 4, Aufl., Band 2,Verlag Chemie,Weinheim.